ALMA MATER STUDIORUM
UNIVERSITÀ DI BOLOGNA

DOTTORATO DI RICERCA IN
ASTROFISICA

Ciclo XXXIV

AN EFFICIENT JEANS MODELLING OF AXISYMMETRIC GALAXIES WITH MULTIPLE STELLAR COMPONENTS

Presentata da: **Caterina Caravita**

Supervisore:
Chiar.mo Prof. **Luca Ciotti**

Co-supervisore:
Chiar.ma Prof.ssa **Silvia Pellegrini**

Coordinatore:
Chiar.mo Prof. **A. Miglio**

Esame finale anno 2022

Settore Concorsuale: 02/C1 – Astronomia, Astrofisica, Fisica della Terra e dei Pianeti
Settore Scientifico Disciplinare: FIS/05 – Astronomia e Astrofisica

Abstract

Dynamical models of stellar systems represent a powerful tool to study their internal structure and dynamics, to interpret the observed morphological and kinematical fields, and also to support numerical simulations of their evolution.

We present a method especially designed to build axisymmetric Jeans models of galaxies, assumed as stationary and collisionless stellar systems. The aim is the development of a rigorous and flexible modelling procedure of multicomponent galaxies, composed of different stellar and dark matter distributions, and a central supermassive black hole. The stellar components, in particular, are intended to represent different galaxy structures, such as discs, bulges, halos, and can then have different structural (density profile, flattening, mass, scale-length), dynamical (rotation, velocity dispersion anisotropy), and population (age, metallicity, initial mass function, mass-to-light ratio) properties.

The theoretical framework supporting the modelling procedure is presented, with the introduction of a suitable nomenclature, and its numerical implementation is discussed, with particular reference to the numerical code JASMINE2, developed for this purpose. We propose an approach for efficiently scaling the contributions in mass, luminosity, and rotational support, of the different matter components, allowing for fast and flexible explorations of the model parameter space. We also offer different methods of the computation of the gravitational potentials associated of the density components, especially convenient for their easier numerical tractability.

A few galaxy models are studied, showing internal, and projected, structural and dynamical properties of multicomponent galaxies, with a focus on axisymmetric early-type galaxies with complex kinematical morphologies. The application of galaxy models to the study of initial conditions for hydro-dynamical and N-body simulations of galaxy evolution is also addressed, allowing in particular to investigate the large number of interesting combinations of the parameters which determine the structure and dynamics of complex multicomponent stellar systems.

Contents

Chapter 1

Introduction

Galaxies are complex systems, populating the Universe. In some cases they are quite solitary, in other cases they are embedded in more or less crowded environments, such as groups and clusters of galaxies. In any case, they are composed of an ensemble of different matter components, gravitationally bounded: they are made of stars, interstellar medium (ISM, mainly composed of gas and dust), typically they contain a supermassive black hole (BH) in the galactic centre, and, last but not least, a huge halo of dark matter (DM) seems to host the galactic baryonic components. Moreover, like the ISM that occurs in different phases and distributions, also the stars do not belong to one single population; galaxies may contain, as principal components, a main younger stellar disc, or even a thin and a thick disc, embedded in an older stellar halo, a central bulge, a nuclear stellar disc and a nuclear star cluster, a bar, and spiral arms. The stellar dynamics plays a crucial role in connecting many aspects of galaxies, and stellar systems in general, such as also open and globular clusters. On one side, the stellar orbits are of course determined by the structure of the system, including the amount and distribution of the other matter components (and we will see how), which in turn depends on the history of formation and evolution of the system itself. On the other side, the stellar dynamics influences the evolution of the whole system. In galaxies, for instance, the stellar rotation affects the cooling flows, enhancing the formation of a cold gaseous disc in the galactic plane; the development of local instabilities in the disc then can lead to star formation bursts and to gas accretion events onto the central BH. Moreover, the rotation of galactic stellar discs enhances the development of global disc instabilities, which can lead to the formation of bars in the central galactic regions. The shape and rotation of galaxies are also recognised to significantly influence the X-ray properties of the hot gaseous corona. These are only some examples of evolutionary mechanisms which are strongly correlated to stellar dynamical properties. Therefore, the development of rigorous modelling techniques for the internal structure and dynamics is fundamental to understand the physical processes in real galaxies, and in particular to interpret observed morphological and kinematical fields, and to infer possible formation and evolution paths. Beyond a pure theoretical interest in understanding the internal processes feeding stellar systems, in the era of integral field spectroscopy (IFS) and large surveys, and of high-performance computing,

Figure 1.1: Elliptical galaxies IC2006 (left) and NGC1132 (right) from Hubble Space Telescope.

more and more sophisticated dynamical models are indeed required for the interpretation of observed galaxies and for simulations of their evolution.

1.1 Early-type galaxies

The focus of this Thesis is on early-type galaxies (ETGs) in the Local Universe (i.e. at redshift $z \simeq 0$). ETGs usually include elliptical (Es), lenticular (S0s), and dwarf galaxies, and so they can present an almost spherical shape up to a very flattened disc-like shape, without spiral arms (see two examples in Fig. 1.1). They represent in practice the left-hand side of the Hubble tuning-fork (Hubble 1936, see also Sandage 1961), and they have elliptical shape when observed in the plane of the sky. They are distinguished by late-type galaxies, which include spirals (with or without bar) and irregular galaxies. These two main categories present a strong bimodality, not only in their morphology, but also in several galaxy properties: ETGs in the Local Universe are typically passive (absent or almost absent star formation events), populated by older stars and then redder, rich of hot gas but poor of cold gas, and more metal-rich, with respect to late-type galaxies; moreover, they are mainly found in denser environments. In the Local Universe, ETGs are more rare than late-type, with about $20-30\%$ of the observed nearby galaxies versus $70-80\%$.

ETGs are observed to follow some empirical relations, showing correlations between their structural, and dynamical properties, so-called *Scaling Laws*. Just to briefly review the most important ones, we recall the Faber-Jackson relation (Faber and Jackson, 1976) and the Kormendy relation (Kormendy, 1977). The former one states a correlation between the luminosity (L, total or in a given band) and the stellar velocity dispersion (measured within a certain aperture radius, typically the effective radius R_{e}, so σ_{e}) of ETGs; the latter one, between the surface brightness (measured within e.g. R_{e}, so I_{e}) and the size of the galaxy, usually measured by R_{e}. From the Kormendy relation, it is also derived the so-called *size-luminosity* relation, involving L instead of I_{e}. Overall, it is widely recognised that ETGs with larger velocity dispersion of the stars (and so larger

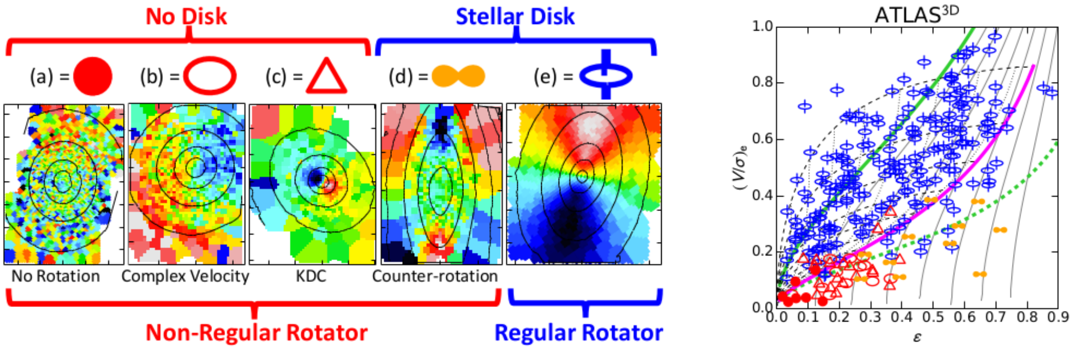

Figure 1.2: On the left, the five classes of ETGs distinguished by Krajnović et al. (2011) on the basis of the morphology of the velocity maps. On the right, the $(v/\sigma, \varepsilon)$ diagram for a sample of ETGs of the ATLAS^{3D}survey, where the symbols for the same classes are reported according to the legend on the left. The plots are taken from Cappellari (2016), to which we refer for details.

mass, from the *Virial Theorem*) are in general more extended and more luminous. These Scaling Laws are also a representation of the *Fundamental Plane* (Dressler et al., 1987; Djorgovski and Davis, 1987): ETGs remarkably lie on a plane $(\log I_\mathrm{e}, \log \sigma_\mathrm{e}, \log R_\mathrm{e})$, with a small scatter, and the Faber-Jackson and the size-luminosity relations can be obtained as projections of this plane. Another fundamental empirical scaling law highlights a strong correlation between the evolution of ETGs and their central BH: the mass of the BH is typically three orders of magnitude smaller than the total stellar mass of the host galaxy (Magorrian et al., 1998).

Thanks to the advent of Integral Field Spectroscopy, providing detailed kinematical maps, ETGs have shown kinematical features which have suggested a further classification, distinguishing them primarily in two main classes: the slow rotators and the fast rotators (Krajnović et al. 2011 from ATLAS^{3D}data, see also e.g. Cappellari 2016 for a review). Fast rotators show a wide range of observed ellipticity $\varepsilon = 1 - b/a$ (where b/a is the ratio between minor and major axis), and a regular pattern of rotation projected along the line-of-sight; they are also called *regular rotators*. Slow rotators, on the other side, have ellipticity typically $\varepsilon \lesssim 0.4$, and they are also called *non-regular rotators*; in particular four sub-classes have been recognised based on the morphology of the kinematical maps: not-rotating galaxies, galaxies with complex and irregular rotation pattern, galaxies with kinematically decoupled core, galaxies with two counter-rotating discs, as summarised in Fig. 1.2 (e.g. Morelli et al., 2004; Krajnović et al., 2015; Mitzkus et al., 2017). In the classical $(v/\sigma, \varepsilon)$ diagram (Binney, 1978), the distinction between regular and non-regular rotators is apparent: regular rotators are flatter and the flattening is more supported by the rotation, while non-regular rotators are rounder and mainly supported by the anisotropy of the velocity dispersion tensor (see the right panel of Fig. 1.2).

It is of course well-known that galaxies are made of different stellar components, as already mentioned, but the easier treatment of galaxy modelling in the assumption of a single stellar population, with global average properties, such as a total surface brightness distribution, a constant mass-to-light ratio, mean age and chemical abundance, and so on, made this approximation the most used for many years. Moreover, the possibility of theoretical studies on multiple stellar components was not supported by advanced enough observations or numerical simulations. Nowadays, the complexity revealed by observations of the kinematical fields of ETGs, and the huge amount of data available, have highlighted the need of sophisticate and flexible procedures for the galaxy models, in order to reproduce and interpret such kinematical features, clearly due to the presence of multiple stellar components, with different structural, dynamical and chemical properties. Moreover, other observational evidences request to properly model different stellar populations, such as gradients of color, chemical abundances, mass-to-light ratio, suggesting the importance of taking into account age, metallicity, stellar initial mass function (IMF) variations inside galaxies (e.g. Martín-Navarro et al. 2015; van Dokkum et al. 2017; Parikh et al. 2018; Bernardi et al. 2018; García-Benito et al. 2019; besides the non-universality of the IMF between different galaxies, see e.g. van Dokkum and Conroy 2010; Cappellari et al. 2012, 2013). More and more realistic galaxy models are also required by numerical simulations of galaxy evolution, both hydrodynamical or N-body simulations. We have already mentioned the importance of rigorous and flexible galaxy models in simulations, and we will dedicate a specific Introduction in Chapter 6 (see also Section 7.2), so we will not go in more details now.

1.2 Dynamical models

Dynamical models of galaxies are usually based on the assumption that galaxies are stellar systems in equilibrium, i.e. in a stationary state. The phase-space distribution function of the stars (DF), i.e. the 6-dimensional function describing the 3D position and the 3D velocity of each star, usually cannot be recovered, and so basic assumptions on its form are in order. For axisymmetric systems, due to the easier tractability, it is often assumed that the DF depends on the two classic integrals of motion, namely the energy and the axial component of the angular momentum.

Axisymmetric (oblate or prolate) galaxy models often represent an acceptable description of real galaxies, beyond the zeroth-order approximation of spherical symmetry. Analytical models of single and multicomponent axisymmetric galaxies are available only in few simpler cases; moreover, while of fundamental importance in elucidating physical concepts behind the stellar dynamics, and so in guiding the construction of more realistic galaxy models to be carried out numerically, analytical models necessarily suffer from the restrictions imposed by the request of analytical tractability, and they miss the flexibility of a numerical treatment. Analytical and numerical modelling should be seen then as complementary approaches.

Dynamical models of galaxies have been developed during the years, following different approaches. The most widely used are the Jeans modelling (Jeans 1922; see e.g. Binney and Tremaine 2008; Ciotti 2021), based on the application of equations very similar to those describing the hydrodynamics to the stellar dynamics, the orbit superposition technique (Schwarzschild, 1979), the made-to-measure particle based method (Syer and Tremaine, 1996), the torus mapper technique (Binney and McMillan, 2016).

The Jeans approach is based on the assumption of a two-integral DF, so that the Jeans equations solved for the stellar distribution embedded in a total gravitational potential give the total stellar velocity fields. In this framework, the stellar system is *quasi-isotropic*, in the sense that the axisymmetry naturally imposes that the velocity dispersion tensor is isotropic in the vertical and radial directions, and the system rotates only around the symmetry axis. Moreover, except in the isotropic case, the Jeans equations are not a closed system, and they lead to a degeneracy between the streaming velocity and velocity dispersion in the azimuthal direction (in cylindrical coordinates); this degeneracy is solved a posteriori by the adoption of an arbitrary kinematical decomposition. DFs which do not depend on two integrals can be considered within the Jeans method forcing the basic assumptions, and introducing also a radial anisotropy (Cappellari, 2008). The other methods mentioned are more general and suitable in modelling stellar systems described by three-integral DFs, however they are also more computationally demanding, and less straightforward in their use.

This Thesis and the numerical code developed, JASMINE2, are based on the Jeans approach, in particular with the aim of producing a tool suitable for the modelling of stellar systems with multiple stellar components. In general, we can consider two approaches when dealing with dynamical modelling of galaxies: one focused on the reproduction of specific observed galaxy properties, and the construction of best-fit models, that we can call *from observations to models*; the other one focused on the theoretical models of the galactic structure and dynamics, that we can call *from models to observations*. As example of the first approach, based on the solution of the Jeans equations and addressed to multiple stellar components, as well, we would like to mention the multi-gaussian expansion method (MGE, Emsellem et al., 2011; Cappellari, 2002). It consists in a series expansion of galaxy images with 2D gaussian functions; then the deprojected internal density is easily reconstructed, and other dynamical and photometric quantities can be easily and accurately evaluated, thanks to the analytical tractability of the gaussian function. In this way, an arbitrary large number of gaussian distributions is considered to best-match the surface brightness of the galaxy; to each gaussian is associated a deprojected internal density distribution, implicitly described by a phase-space DF, so that for each density component the Jeans equations are solved in the total gravitational potential; finally, the total kinematical fields are reconstructed. This method has been applied, for example, to a large number of galaxies of the ATLAS$^{3\mathrm{D}}$survey for the interpretation of the kinematical components observed, as illustrated in Fig. 1.2. Our method, instead, follows the second approach: we choose an arbitrary number of stellar components, each one implicitly described by its own DF, and modelled by a chosen density profile (e.g. a Hernquist ellipsoidal bulge, and exponential disc, a Jaffe ellipsoidal halo, and so on), then the Jeans equations are solved for each stellar distribution in the total gravitational potential, and the projected morphological and kinematical fields are obtained (for each stellar component), and can be compared with those of observed galaxies. This method allows for a higher level of theoretical understanding of the physical properties of multicomponent galaxies, in particular in case of multiple stellar components. We stress, indeed, that our modelling approach involves a *physical* decomposition of the total stellar distribution, where each underlying DF is intended to represent a physically meaningful stellar component; the MGE method, on the other side, consists in a *mathematical* decomposition. The two methods have their strengths and limitations, and can be seen as complementary in the study of structural and dynamical properties of galaxies.

1.3 Overview of the Thesis

In this Thesis we present the theoretical framework, and the scheme for a numerical implementation, of a multicomponent dynamical modelling of galaxies, in the assumption of axisymmetry in cylindrical coordinates, especially focused on the presence of multiple stellar components. The galaxy models may include an arbitrary number of stellar and DM components, and a central BH; the stellar components can have different structural (density profile, flattening, mass, scale-length), dynamical (rotation, velocity dispersion anisotropy), and population (age, metallicity, initial mass function, mass-to-light ratio) properties. The dynamical models are based on the solution of the Jeans equations for each stellar distribution, which is implicitly described by a two-integral DF (or even more general). In order to split the azimuthal velocity in the streaming and velocity dispersion motions, several kinematical decompositions are discussed. The sum rules for the combination of the internal structural and dynamical fields, and the projected fields, of the stellar components are presented, giving the resulting total galaxy properties. In a numerical implementation of this modelling procedure, two main obstacles are faced: an extensive exploration of the model parameter space would be impossible, due to the large number of parameters increasing with the number of matter components, and to the computational time required by the numerical evaluation of the gravitational potential associated to each density component, increasing also for increasing numerical resolution. To allow for a fast and flexible multicomponent modelling, the scaling operations allowed by the Poisson and Jeans equations, and by the projection formulae, are fully exploited: we present a *scaling approach*, developed in order to fix the minimum possible number of structural parameters before the computation of the potentials and the solution of the Jeans equations, and then to have the flexibility to vary the maximum possible number of model parameters in post-processing. Moreover, we present several methods for the evaluation of the potential components, allowing to drastically reduce the computational time; in particular, we give a new general formula for a fast numerical computation of the potential produced by factorised discs.

The framework presented is implemented in (and tested with) the numerical code JASMINE2. It is a substantially improved version of the original code JASMINE, which is now able to model multiple stellar components, improved by the addition of the scaling approach, and by different efficient methods for the computation of the gravitational potentials.

In Chapter 2, the theoretical framework for the multicomponent modelling is presented, and in Chapter 3 the scaling approach, with some references to the specific implementation in JASMINE2. In Chapter 4, the library of density models implemented in JASMINE2 is listed, with the related analytical potential when known, and several methods for its numerical evaluation are illustrated; finally, some tests are shown, to prove the accuracy of the numerical procedures, and in particular JASMINE2 is also used to verify the reliability of analytical formulae in homoeoidal approximation. In Chapter 5, some illustrative galaxy models including two distinct stellar components are shown, and their internal structural and dynamical properties discussed, together with the resulting projected fields; it is shown, for example, the effect of slightly prolate stellar components, of faster stellar discs embedded in stellar halos, of counter-rotating stellar components. Moreover, the possibility to reproduce properties of double-exponential discs through the sum of Miyamoto-Nagai discs is explored. In Chapter 6, we report a study of the effects of the shape and the rotation of the stellar component on gas flows in ETGs, which supports a more extended study of the evolution of gas flows carried out by means of hydrodynamical simulations. In each chapter, brief introductions and conclusions will help to take stock and follow the main flow of the dissertation. In Chapter 7, the whole work is summarised and the main results reported. Furthermore, an ongoing study on the stability of stellar discs is presented, in its preliminary stage; in particular, it is focused on criteria able to foresee the development of global instabilities leading to bar formation, with the employment of N-body simulations. At the end of this Thesis, a few Appendices report relevant analytical and technical arguments.

The Thesis is mainly based on a published and a submitted paper, and some brief and preliminary aspects were published also in Conference proceedings, with additional original material which will be partially included in other papers in preparation. The published and in preparation papers are listed below; then, at the beginning of each Chapter, we report the publications on which the material is mainly inserted.

- Dynamical models of spheroidal multi-component stellar systems
  Caravita C., Ciotti L., Pellegrini S., 2020, IAUS, 351, 273
- Jeans modelling of axisymmetric galaxies with multiple stellar populations
  Caravita C., Ciotti L., Pellegrini S., 2021, MNRAS, 506, 1480
- A parameter space exploration of high resolution numerically evolved ETGs including AGN feedback and accurate dynamical treatment of stellar orbits
  Ciotti L., Ostriker J. P., Gan Z., Jiang B. X., Pellegrini S., Caravita C., Mancino A., 2022, Accepted for publication, ApJ
- An efficient method to compute the gravitational potential of disc galaxies
  Caravita C., Ciotti L., In preparation
- Stability of disc galaxies through dynamical models and N-body simulations
  Caravita C., D'Onghia E., Ciotti L., Pellegrini S., In preparation

Chapter 2

Multicomponent modelling

We illustrate the main theoretical foundations on which our modelling procedure is based, and we introduce the general notation used. We discuss how the internal structure and dynamics are reconstructed for multicomponent axisymmetric systems in equilibrium, which can be composed of an arbitrary number of stellar and dark matter components, and in presence of a central supermassive black hole. We focus on the solution of the Jeans equations for the multiple stellar components embedded in the total gravitational potential, and satisfying the Virial Theorem. Then, we present different possible decompositions for the azimuthal motions, and the projection formulae on the plane of the sky of the morphological and kinematical fields produced, together with relevant observable galaxy properties. The formulae discussed have been implemented in (and tested with) our numerical code JASMINE2.

Caravita C., Ciotti L. and Pellegrini S., 2020, IAUS

Caravita C., Ciotti L. and Pellegrini S., 2021, MNRAS

2.1 Structure of the galaxy models

We adopt cylindrical coordinates (R, φ, z), with the symmetry axis of the models aligned with the z-axis. In full generality, we consider models composed of N different stellar density distributions $\rho_{*i}(R,z)$, of total mass M_{*i}, so that the total stellar density ρ_* and the total stellar mass M_* of the system are given respectively by

$$\rho_*(R,z) = \sum_i \rho_{*i}, \qquad M_* = \sum_i M_{*i}, \quad i = 1, \ldots, N. \tag{2.1}$$

From now on, sums over i indicate sums over the N stellar components. We assume that each ρ_{*i} is made of a simple stellar population (see e.g. Renzini and Buzzoni, 1986; Maraston, 2005), i.e. by stars of the same age, chemical composition, initial mass function, and in particular the same mass-to-light ratio Υ_{*i}. Therefore, the total stellar distribution ρ_* can be considered a composite stellar population; the luminosity density and the total luminosity of each stellar component can be written respectively as

$$\nu_{*i}(R,z) = \frac{\rho_{*i}}{\Upsilon_{*i}}, \qquad L_i = \frac{M_{*i}}{\Upsilon_{*i}}, \tag{2.2}$$

so that

$$\nu_*(R,z) = \sum_i \nu_{*i}, \qquad L = \sum_i L_i. \tag{2.3}$$

The local and average stellar mass-to-light ratios of the galaxy are given by

$$\Upsilon_*(R,z) \equiv \frac{\rho_*}{\nu_*} = \frac{\sum_i \rho_{*i}}{\sum_i \rho_{*i}/\Upsilon_{*i}}, \qquad < \Upsilon_* > \equiv \frac{M_*}{L} = \frac{\sum_i M_{*i}}{\sum_i M_{*i}/\Upsilon_{*i}}, \tag{2.4}$$

where it is apparent how in general the local stellar mass-to-light ratio in a multicomponent model depends on position.

As well-known, a mass density distribution is related to the gravitational potential produced through the Poisson equation, which we write for the total stellar density as

$$\nabla^2 \phi_* = 4\pi G \rho_*; \tag{2.5}$$

then, from eq. (2.1), we can write the total stellar potential as

$$\phi_*(R,z) = \sum_i \phi_{*i}, \tag{2.6}$$

where $\phi_{*i}(R,z)$ is the potential originated by the density component ρ_{*i}. The presence of a central BH, of mass $M_{\rm BH}$, produces the potential

$$\phi_{\rm BH}(r) = -\frac{GM_{\rm BH}}{r}, \qquad r = \sqrt{R^2 + z^2}, \tag{2.7}$$

and an axisymmetric DM halo, of density $\rho_{\rm h}(R,z)$ and total mass $M_{\rm h}$ (when finite), produces the potential $\phi_{\rm h}(R,z)$. Therefore, in general, the total gravitational potential of the model is

$$\Phi(R,z) = \phi_* + \phi_{\rm h} + \phi_{\rm BH} = \sum_j \phi_j, \qquad j = 1,\dots,N+2. \tag{2.8}$$

From now on, sums over j indicate sums over *all* the $N+2$ galaxy components, i.e. the N stellar components, the central BH, and the DM halo. In principle, also the DM distribution can be made of different components, with a trivial generalisation of the current discussion, which is not necessary to detail here; in Chapter 6, for example, some galaxy models are shown, including the effect of a group/cluster DM halo, in addition to the galactic DM halo. Our approach to multicomponent systems fully exploits the linearity of the Jeans equations with respect to the stellar density and to the gravitational potential, as shown in the following Sections and in the next Chapter.

2.2 N systems of Jeans equations

The procedure, in its basic version, assumes that each stellar component is implicitly described by a two-integral phase-space DF $f_i(E,J_z)$, in general different for each component, where E and J_z are respectively the energy and the axial component of the angular momentum of each star (per unit mass) in the *total* potential Φ. Therefore, the DF of the total stellar distribution is the two-integral function

$$f = \sum_i f_i. \tag{2.9}$$

In Appendix A, the assumption of non-collisionality is summarised, and the method of moments presented; then the Jeans equations are derived, and the Virial theorem verified, showing stationary and axisymmetric systems as particular case. Here we apply the same procedure, with the generalisation to multiple stellar components. First of all, f and f_i of eq. (2.9) satisfy eq. (A.3), giving respectively ρ_* and ρ_{*i}. As usual, we indicate with $({\rm v}_R, {\rm v}_\varphi, {\rm v}_z)$ the velocity components in the phase-space, and with a bar over a quantity the operation of average over the velocity-space, weighted for the DF of the stellar component of interest. We recall here that, in the assumption of two-integral DF, for each stellar component $\overline{{\rm v}_{R}}_i = \overline{{\rm v}_{z}}_i = 0$, the only non-zero ordered velocity can occur in the azimuthal direction $v_{\varphi i} \equiv \overline{{\rm v}_\varphi}_i$, and finally for the velocity dispersion tensor $\sigma_{Ri} = \sigma_{zi} \equiv \sigma_i$. Of course, from eq. (2.9), similar relations hold as well for the dynamical fields of the total ρ_*.

The Jeans equations for each stellar component are obtained as velocity moments of the Collisionless Boltzmann Equation for the corresponding f_i over the velocity space.

Overall, we have N systems of Jeans equations for the N stellar components,

$$\begin{cases} \dfrac{\partial \rho_{*i}\sigma_i^2}{\partial z} = -\rho_{*i}\dfrac{\partial \Phi}{\partial z}, \\ \\ \dfrac{\partial \rho_{*i}\sigma_i^2}{\partial R} = \rho_{*i}\dfrac{\Delta_i}{R} - \rho_{*i}\dfrac{\partial \Phi}{\partial R}, \end{cases} \tag{2.10}$$

where Φ is the total potential in eq. (2.8), and

$$\Delta_i \equiv \overline{\mathrm{v}_{\varphi}^2}_i - \sigma_i^2, \qquad \sigma_{\varphi i}^2 = \overline{\mathrm{v}_{\varphi}^2}_i - v_{\varphi i}^2 = \Delta_i + \sigma_i^2 - v_{\varphi i}^2. \tag{2.11}$$

In the isotropic case, it is immediate to prove that also $\sigma_{\varphi i} = \sigma_i$ and $\Delta_i = v_{\varphi i}^2$. Imposing the natural boundary condition $\rho_{*i}\sigma_i^2 \to 0$ for $z \to \infty$, the solution of eqs. (2.10) is

$$\rho_{*i}\sigma_i^2 = \int_z^\infty \rho_{*i}\frac{\partial \Phi}{\partial z'}\,\mathrm{d}z', \qquad \rho_{*i}\Delta_i = R\left(\frac{\partial \rho_{*i}\sigma_i^2}{\partial R} + \rho_{*i}\frac{\partial \Phi}{\partial R}\right). \tag{2.12}$$

We notice that Δ_i can be also recast as a commutator-like integral as

$$\rho_{*i}\Delta_i = R\int_z^\infty \left(\frac{\partial \rho_{*i}}{\partial R}\frac{\partial \Phi}{\partial z'} - \frac{\partial \rho_{*i}}{\partial z'}\frac{\partial \Phi}{\partial R}\right)\mathrm{d}z', \tag{2.13}$$

with some advantage for analytical and numerical investigations (see e.g. eq. 35 in Ciotti et al. 2021, from now on shortened to CMPZ21); however we found by several numerical tests that Δ_i can also be accurately computed by (centred) numerical differentiation as in eq. (2.12), and so in our code JASMINE2 we maintain this more direct way of evaluation.

Furthermore, although our modelling procedure is based on the assumption of two-integral DFs, it is straightforward the generalisation proposed by Cappellari (2008), with the inclusion of the orbital anisotropy in the Jeans equations (2.10). In this case (also implemented in JASMINE2), we have $\sigma_{Ri} = b_i\,\sigma_{zi}$, with b_i a constant parameter that can be different for each stellar component, and the underlying f_i does not depend on the two classic integrals of motion.

A central point of the procedure is the sum rule in the phase-space imposed by the identity (2.9). We are assuming that the N stellar components ρ_{*i} are physically distinct, each of them described by its own f_i, and so necessarily the N pairs of equations (2.10) are the moment equations of each f_i in the total potential Φ. Therefore, for a generic physical property $F(\mathbf{x},\mathbf{v})$, defined over the phase-space, the following equivalences hold:

$$\overline{F}_i = \frac{\int F f_i d^3\mathbf{v}}{\rho_{*i}}, \qquad \overline{F} = \frac{\sum_i \rho_{*i}\overline{F}_i}{\rho_*}, \qquad \overline{F}_{\mathscr{L}} = \frac{\sum_i \nu_{*i}\overline{F}_i}{\nu_*}. \tag{2.14}$$

The first one is the average of F over the velocity-space, weighted for a given f_i; it is the counterpart of the more generic eq. (A.5), when applied specifically to multicomponent systems. Consequently, $\overline{F}$ and $\overline{F}_{\mathscr{L}}$ are properties related to the whole multicomponent system, and they can be interpreted, respectively, as the *mass-weighted* and the *luminosity-weighted* averages of the $\overline{F}_i$. Notice that we are not reconstructing here the phase-space DFs of the models; we just determine the general rules of combination of the velocity moments in multicomponent systems. The previous considerations show how to combine the solution for the single ρ_{*i} to obtain the dynamical fields associated with the total ρ_*. Clearly, the Jeans equations for ρ_*, as given in eq. (2.1), are obtained as the sum of eqs. (2.10) over the N components, and their solution can be written as the mass-weighted quantities

$$\begin{aligned} \sigma^2 &= \frac{\sum_i \rho_{*i}\sigma_i^2}{\rho_*}, \qquad & \Delta &= \frac{\sum_i \rho_{*i}\Delta_i}{\rho_*}, \\ \overline{\mathrm{v}_\varphi^2} &= \frac{\sum_i \rho_{*i}\overline{\mathrm{v}_{\varphi}^2}_i}{\rho_*}, \qquad & v_\varphi &= \frac{\sum_i \rho_{*i}v_{\varphi i}}{\rho_*}, \end{aligned} \tag{2.15}$$

where these identities are of straightforward proof from eqs. (2.14) and (2.11). Note, however, that the velocities $v_{\varphi i}$ sum linearly, since they derive from first-order velocity moments (see eq. A.6), at variance with σ_i, Δ_i, and $\overline{\mathrm{v}_{\varphi}^2}_i$, which are second-order moments (see eqs. A.7 and A.8). By consequence, and at variance with the previous quantities, σ_φ^2 is *not* given by the simple sum of the $\sigma_{\varphi i}^2$ of the single components: in fact, from eq. (2.11), $\sigma_\varphi^2 = \overline{\mathrm{v}_\varphi^2} - v_\varphi^2 = \Delta + \sigma^2 - v_\varphi^2$, and so

$$\sigma_\varphi^2 = \frac{\sum_i \rho_{*i}(\sigma_{\varphi i}^2 + v_{\varphi i}^2)}{\rho_*} - v_\varphi^2. \tag{2.16}$$

In the limiting case of single component, the two last terms cancel out, and the equality is trivially verified. Similarly, we can derive all the corresponding luminosity-weighted quantities, obtained by using as weights the luminosity densities ν_{*i} of the components instead of the mass densities ρ_{*i}, in eqs. (2.15) and (2.16), so that

$$\begin{aligned} \sigma_{\mathscr{L}}^2 &= \frac{\sum_i \nu_{*i}\sigma_i^2}{\nu_*}, \qquad & \Delta_{\mathscr{L}} &= \frac{\sum_i \nu_{*i}\Delta_i}{\nu_*}, \\ \overline{\mathrm{v}_\varphi^2}_{\mathscr{L}} &= \frac{\sum_i \nu_{*i}\overline{\mathrm{v}_{\varphi}^2}_i}{\nu_*}, \qquad & v_{\varphi\mathscr{L}} &= \frac{\sum_i \nu_{*i}v_{\varphi i}}{\nu_*}, \end{aligned} \tag{2.17}$$

and then

$$\sigma_{\varphi\mathscr{L}}^2 = \overline{\mathrm{v}_\varphi^2}_{\mathscr{L}} - v_{\varphi\mathscr{L}}^2 = \Delta_{\mathscr{L}} + \sigma_{\mathscr{L}}^2 - v_{\varphi\mathscr{L}}^2 = \frac{\sum_i \nu_{*i}(\sigma_{\varphi i}^2 + v_{\varphi i}^2)}{\nu_*} - v_{\varphi\mathscr{L}}^2. \tag{2.18}$$

If all the mass-to-light ratios Υ_{*i} are equal, there is no reason to define luminosity-weighted quantities, which are indeed equal to the corresponding mass-weighted ones.

Finally, since each stellar component corresponds to a stationary and axisymmetric stellar system, described by its own DF, and satisfying the Jeans equations, it is also assured the Virial Theorem in the form of eq. (A.33). We refer to Appendix A, and in particular Section A.3, for details, where a generic density ρ in a generic potential Φ are treated; here we recast the main formulae entering the scalar Virial Theorem (that derives from the tensor Virial Theorem) when dealing with multiple stellar components. For each stellar distribution,

$$2K_i + W_i = 0, \tag{2.19}$$

where the trace of the total kinetic energy tensor is given by $K_i = T_{\varphi i} + \Pi_i + \Pi_{\varphi i}/2$, with

$$T_{\varphi i} = 2\pi \int_0^\infty \int_0^\infty \rho_{*i} v_{\varphi i}^2 \, R \, \mathrm{d}R \, \mathrm{d}z, \tag{2.20}$$

$$\Pi_i = 4\pi \int_0^\infty \int_0^\infty \rho_{*i} \sigma_i^2 \, R \, \mathrm{d}R \, \mathrm{d}z, \qquad \Pi_{\varphi i} = 4\pi \int_0^\infty \int_0^\infty \rho_{*i} \sigma_{\varphi i}^2 \, R \, \mathrm{d}R \, \mathrm{d}z, \tag{2.21}$$

and the trace of the gravitational energy tensor reads

$$W_i = -4\pi \int_0^\infty \int_0^\infty \rho_{*i} \left(R \frac{\partial \Phi}{\partial R} + z \frac{\partial \Phi}{\partial z} \right) R \, \mathrm{d}R \, \mathrm{d}z. \tag{2.22}$$

The same argument holds for the total stellar distribution ρ_*: in particular, from the sum rules of eqs. (2.1) and (2.15), it is immediate to prove that

$$K = \sum_i K_i, \qquad W = \sum_i W_i, \qquad 2K + W = 0. \tag{2.23}$$

We spend few additional words on the gravitational energy, because of the importance of different definitions. While W_i is obtained as the trace of the gravitational interaction energy tensor, for the i-th stellar component in the total potential, the gravitational energy of the stellar component in the total potential is given by

$$U_i = 2\pi \int_0^\infty \int_0^\infty \rho_{*i} \Phi \, R \, \mathrm{d}R \, \mathrm{d}z, \tag{2.24}$$

from eq. (A.17). Both the quantities represent the gravitational interaction between matter components, and they are always negative, but W_i involves the *forces* (space-derivatives of the potential), while U_i involves directly the potential (as we discuss in particular in Section 7.2).

2.3 Azimuthal velocity decomposition

As well known, eqs. (2.10) are degenerate in the azimuthal direction, i.e. they only provide the total (squared) azimuthal velocity $\overline{\mathrm{v}_{\varphi_i}^2} = \sigma_{\varphi i}^2 + v_{\varphi i}^2$ for each stellar component. The most common phenomenological approach to break this degeneracy is the Satoh (1980) k-decomposition, valid for systems with $\Delta_i \geq 0$. In addition, we propose an alternative kinematical decomposition which can be applied when $\Delta_i < 0$, a not uncommon case in multicomponent stellar systems. Finally, we give a further equation allowing to close the system of Jeans equations, in the approximation of almost circular orbits.

2.3.1 Satoh k-decomposition

If $\Delta_i \geq 0$ over the whole space, Satoh (1980) assumes

$$v_{\varphi i} = k_i\sqrt{\Delta_i}, \qquad \sigma^2_{\varphi i} = \sigma^2_i + \left(1 - k^2_i\right)\Delta_i, \tag{2.25}$$

with negative values of k_i describing clockwise rotation. The special case $k^2_i = 1$ describes an isotropic rotator ($\sigma_{\varphi i} = \sigma_i$), so the flattening of an ellipsoidal system is totally supported by rotation; on the other side, $k_i = 0$ implies no net rotation ($v_{\varphi i} = 0$), and the flattening is totally supported by tangential velocity anisotropy. In case of spherical symmetry, it is immediate to prove directly from the Jeans equations (eqs. 2.10) that $\Delta_i = 0$, meaning that with the Satoh decomposition a spherical system cannot rotate and is isotropic independently of the value of k_i. Furthermore, in a simpler kinematical decomposition, k_i is assumed constant over the whole space (as can be found in many applications in the literature), while more general decompositions can be obtained by adopting a position-dependent parameter $k_i(R, z)$ (see e.g. eq. 5.8 used in Section 5.2.2 and in Chapter 6), also allowing for values greater than unity: a position-dependent maximum is then determined by the request $\sigma_{\varphi i} = 0$ (e.g. Satoh, 1980; Ciotti and Pellegrini, 1996; Negri, Ciotti and Pellegrini, 2014). In principle each stellar component of a multicomponent model is characterised by a different k_i, so that, from eqs. (2.25) and (2.15), we can define an *effective* Satoh parameter k_e for the total ρ_*, given by

$$k_\mathrm{e} \equiv \frac{v_\varphi}{\sqrt{\Delta}} = \frac{\sum_i k_i \rho_{*i}\sqrt{\Delta_i}}{\rho_*\sqrt{\Delta}}, \qquad \sigma^2_\varphi = \sigma^2 + \left(1 - k^2_\mathrm{e}\right)\Delta, \tag{2.26}$$

where k_e in general depends on position, even if the k_i do not.

2.3.2 Generalised k-decomposition

Clearly, in case of $\Delta_i < 0$ for some stellar component, the Satoh decomposition in eq. (2.25) cannot be applied. The case of a negative Δ_i over some regions of space (or everywhere) is not frequently encountered in applications, but it is not impossible; for example, it necessarily occurs for at least one density component in a multicomponent system with spherically symmetric total density, or in a density distribution elongated along the symmetry axis (see two applications in Sections 5.1 and 5.2; see also e.g. Ciotti 2021). Indeed, $\Delta = 0$ everywhere for a spherical system supported by a two-integral DF, and thus, from eq. (2.15), at least one Δ_i must be negative (excluding the trivial case of all the subcomponents spherically symmetric, so that all $\Delta_i = 0$). Notice that $\Delta_i < 0$ is not necessarily a manifestation of an inconsistent DF ($f_i < 0$), while if $\overline{\mathrm{v}^2_{\varphi i}} = \Delta_i + \sigma^2_i < 0$ *certainly* the whole model must be discarded as unphysical, even if the solution for the *total* stellar distribution is well-behaved. Therefore, in case of some $\Delta_i < 0$, but positivity of the sum $\Delta_i + \sigma^2_i \geq 0$, the Satoh decomposition is generalised to

$$v_{\varphi i} = k_i\sqrt{\Delta_i + \sigma^2_i}, \qquad \sigma^2_{\varphi i} = \left(1 - k^2_i\right)\left(\Delta_i + \sigma^2_i\right), \qquad k^2_i \leq 1, \tag{2.27}$$

where again k_i can depend on position. We refer to this alternative decomposition as to the *generalised* k-decomposition. The case $k_i = 0$ implies no net rotation ($v_{\varphi i} = 0$), while now $k_i^2 = 1$ corresponds to $\sigma_{\varphi i} = 0$; notice that no isotropic rotators can be realised from eq. (2.27) when $\Delta_i < 0$, because isotropy ($\sigma_{\varphi i} = \sigma_i$) would imply $k_i^2 < 0$. At variance with the Satoh decomposition, it is now possible to model rotating and anisotropic spherical systems (an application of this last case can be found, for example, in exploratory numerical simulations of rotating gas flows in galaxies of Yoon et al. 2019). Notice that the generalised decomposition applied to systems with $\Delta_i \gg \sigma_i^2$ (as for instance the case of highly flattened discs) reduces to the standard Satoh formula. A more interesting (and delicate) case, requiring particular care in the choice of the parameter k_i, is represented by systems with $|\Delta_i| \ll \sigma_i^2$, when we have $v_{\varphi i} \sim k_i \sigma_i$, and $\sigma_{\varphi i}^2 \sim (1 - k_i^2)\sigma_i^2$. This means that, in order to avoid substantial rotation, for example in almost spherical systems (oblate or prolate), k_i must be kept small.

We finally remark that, for a given multicomponent system, it is also possible to assume a Satoh decomposition for some components, and the generalised decomposition for the others. In analogy with eq. (2.26) it is possible to define a total *effective* decomposition parameter k_e as

$$k_\mathrm{e} \equiv \frac{v_\varphi}{\sqrt{\Delta + \sigma^2}}, \qquad \sigma_\varphi^2 = \left(1 - k_\mathrm{e}^2\right)\left(\Delta + \sigma^2\right). \tag{2.28}$$

2.3.3 Epicyclic approximation

We consider a further possibility for the determination of the azimuthal motions. For quite flattened axisymmetric systems, the stellar orbits can be described by almost circular orbits, in the so-called *epicyclic approximation*. In this case, it can be shown that the azimuthal velocity dispersion is directly related to the radial (and vertical) velocity dispersion by

$$\sigma_{\varphi i}^2 = \frac{\sigma_i^2}{\eta^2}, \qquad v_{\varphi i}^2 = \Delta_i + \left(1 + \frac{1}{\eta^2}\right)\sigma_i^2, \tag{2.29}$$

where

$$\eta^2 = \frac{4}{R}\frac{\partial \Phi}{\partial R}\left(\frac{3}{R}\frac{\partial \Phi}{\partial R} + \frac{\partial^2 \Phi}{\partial R^2}\right)^{-1} \tag{2.30}$$

(see e.g. B&T08). Notice that that $v_\mathrm{c}^2 = R\,\partial\Phi/\partial R$ is the squared circular velocity on the equatorial plane, and Φ is the total potential (eq. 2.8). Under this approximation, the ordered rotational velocity of the stellar component is everywhere near to the circular velocity at the same radius, and the first- and second-order velocity moments are all determined only by the structure of the system, without assuming any arbitrary decomposition parameter. This means that the system of two Jeans equations (eq. 2.10) turns out to be closed. Moreover, the ratio between azimuthal and vertical velocity dispersion, i.e. η in eq. (2.30), is the same for all the stellar components in the model. Obviously, this approximation is quite realistic only for very flattened systems made of circular orbits. In Section 7.2, we mention some models of disc galaxies where the epicyclic approximation is employed, following Springel et al. 2005.

2.4 Projections

We recast here the projection formulae presented in Posacki et al. (2013) for the case of a multicomponent system, focusing in particular on how the solutions for the components must be summed to obtain the projected fields of the total stellar distribution. We indicate with $<,>$ the scalar product, with $\mathbf{n}$ the line-of-sight direction (hereafter los) directed from the observer to the galaxy[1], and with l the integration path along the los. For the ease of notation in this Section we drop the subscript i, so that all the following formulae must be intended to hold separately for each stellar component ρ_{*i} (and of course also for the total ρ_*). We will resume the use of the subscript i at the end of the Section, when we give the expressions for the projected fields of ρ_* as functions of the projected fields of the components. The projection of a stellar density, and of the ordered velocity $\boldsymbol{v} = v_\varphi \, \mathbf{e}_\varphi$, are

$$\Sigma_* = \int_{-\infty}^{\infty} \rho_* \, \mathrm{d}l, \quad \Sigma_* v_{\mathrm{los}} = \int_{-\infty}^{\infty} \rho_* v_\varphi < \mathbf{e}_\varphi, \mathbf{n} > \, \mathrm{d}l, \tag{2.31}$$

where $\mathbf{e}_\varphi = (-\sin\varphi, \cos\varphi, 0)$ is the unitary vector in the tangential direction. From the adopted orientation of $\mathbf{n}$, a positive/negative v_{los} indicates a motion receding from/approaching to the observer, respectively. The los velocity dispersion can be written as

$$\sigma_{\mathrm{los}}^2 = \sigma_{\mathrm{P}}^2 + V_{\mathrm{P}}^2 - v_{\mathrm{los}}^2 = V_{\mathrm{rms}}^2 - v_{\mathrm{los}}^2, \tag{2.32}$$

where

$$\Sigma_* \sigma_{\mathrm{P}}^2 = \int_{-\infty}^{\infty} \rho_* < \boldsymbol{\sigma}^2 \mathbf{n}, \mathbf{n} > \, \mathrm{d}l, \qquad \Sigma_* V_{\mathrm{P}}^2 = \int_{-\infty}^{\infty} \rho_* v_\varphi^2 < \mathbf{e}_\varphi, \mathbf{n} >^2 \, \mathrm{d}l, \tag{2.33}$$

and we refer to Ciotti and Pellegrini (1996), in particular, for a thorough distinction between the meanings of 'P' and 'los'; in the first eq. (2.33), $\boldsymbol{\sigma}$ is the 3×3 velocity dispersion tensor. We also define $V_{\mathrm{rms}}^2 \equiv \sigma_{\mathrm{P}}^2 + V_{\mathrm{P}}^2 = \sigma_{\mathrm{los}}^2 + v_{\mathrm{los}}^2$, in agreement with the definition of Cappellari (2008). The fields V_{rms} and v_{los} in general depend on the specific direction $\mathbf{n}$; moreover, v_{los}, σ_{P} and V_{P} depend on the specific velocity decomposition adopted, while V_{rms} is independent of the velocity decomposition. For this reason, this latter can be a convenient observable quantity to fit (see e.g. Cappellari, 2008). The previous identities are fully general and hold for a generic inclination of the los with respect to the galaxy. For our axisymmetric models, it is assumed without loss of generality that the los is parallel to the $x - z$ plane, and the projection plane rotates around the y axis.

In particular, in the face-on projection (hereafter FO), the los is parallel to the z axis with $\mathbf{n} = -\mathbf{e}_z$, the projection plane is the $x - y$ plane, and

$$\Sigma_* = 2\int_0^{\infty} \rho_* \, \mathrm{d}z, \quad \Sigma_* \sigma_{\mathrm{los}}^2 = 2\int_0^{\infty} \rho_* \sigma^2 \, \mathrm{d}z, \tag{2.34}$$

---

[1] Since in the following we refer often to CMPZ21, we report here the different convention adopted: in that paper, indeed, $\mathbf{n}$ points from the galaxy to the observer.

because $v_{\rm los} = V_{\rm P} = 0$, and so $\sigma_{\rm los} = \sigma_{\rm P}$. In the edge-on projection (hereafter EO), the los is aligned with the x axis with $\mathbf{n} = -\mathbf{e}_x$, the projection plane coincides with the $y - z$ plane, and $(\cos\varphi, \sin\varphi) = (x/R, y/R)$, where $R = \sqrt{x^2 + y^2}$. Therefore

$$\Sigma_* = 2\int_y^\infty \frac{\rho_* R}{\sqrt{R^2 - y^2}}\,{\rm d}R, \quad \Sigma_* v_{\rm los} = 2y\int_y^\infty \frac{\rho_* v_\varphi}{\sqrt{R^2 - y^2}}\,{\rm d}R, \tag{2.35}$$

and, with some algebra from eqs. (2.33),

$$\Sigma_* \sigma_{\rm P}^2 = 2\int_y^\infty \frac{(R^2 - y^2)\sigma^2 + y^2\sigma_\varphi^2}{R\sqrt{R^2 - y^2}}\rho_*\,{\rm d}R, \tag{2.36}$$

$$\Sigma_* V_{\rm P}^2 = 2y^2\int_y^\infty \frac{\rho_* v_\varphi^2}{R\sqrt{R^2 - y^2}}\,{\rm d}R. \tag{2.37}$$

Finally, exploiting eq. (2.11), eq. (2.32) can be recast in compact form as

$$\Sigma_* \sigma_{\rm los}^2 = 2\int_y^\infty \frac{R^2\sigma^2 + y^2\Delta}{R\sqrt{R^2 - y^2}}\rho_*\,{\rm d}R - \Sigma_* v_{\rm los}^2, \tag{2.38}$$

where the independence of $V_{\rm rms}$ (first term) from the specific azimuthal velocity decomposition is here apparent. We stress that at this stage JASMINE2 performs only FO and EO projections, but the extension to general los is one of our prospects.

2.4.1 Mass-weighted projections

The projected properties of a multicomponent stellar system can now be obtained, regardless of the los direction, by considering the sum rules of the internal quantities shown so far. From eqs. (2.1) and (2.15), and from eqs. (2.31)–(2.33), it is immediate to see that

$$\Sigma_* = \sum_i \Sigma_{*i}, \quad v_{\rm los} = \frac{\sum_i \Sigma_{*i}\, v_{{\rm los}i}}{\Sigma_*}, \quad V_{\rm rms}^2 = \frac{\sum_i \Sigma_{*i} V_{{\rm rms}i}^2}{\Sigma_*}, \tag{2.39}$$

and $\sigma_{\rm los}^2$ is given again by eq. (2.32).

2.4.2 Luminosity-weighted projections

No difficulty is encountered in the construction of the luminosity-weighted fields analogous to eqs. (2.39), by using the surface brightness distributions, $I_{*i} = \Sigma_{*i}/\Upsilon_{*i}$ and $I_* = \sum_i I_{*i}$, in lieu of the surface densities, Σ_{*i} and Σ_*. In particular, the los luminosity-weighted rotational velocity $v_{{\rm los}\mathscr{L}}$ and velocity dispersion $\sigma_{{\rm los}\mathscr{L}}$ are obtained. At variance with the (internal, i.e. non projected) quantities of Section 2.2, the luminosity-weighted projected properties are equal to the mass-weighted ones only if all the mass-to-light ratios Υ_{*i} of the different stellar components are equal and constant. The projected stellar mass-to-light ratio is defined as $\Upsilon_{*{\rm los}} \equiv \Sigma_*/I_*$, in analogy with the local Υ_* in eq. (2.4).

Thus it is given by the ratio between the projected mass and luminosity, and not by the projection of their ratio, i.e. it is not the projection of Υ_*.

For their usefulness in the observational field, we introduce some further quantities: in particular, ETGs satisfy empirical Scaling Laws (e.g. Faber and Jackson, 1976; Kormendy, 1977) relating their size, luminosity, and kinematics. We can define for each stellar distribution an *effective radius*[2], $R_{\mathrm{e}i}$, as the radius of the circumference of half-light, $L_i/2$, on the plane of the sky; analogously, we have the total effective radius R_e enclosing $L/2$. They are respectively defined by

$$L_i(R_{\mathrm{e}i}) = 2\pi \int_0^{R_{\mathrm{e}i}} I_{*i}\, t\, \mathrm{d}t = \frac{L_i}{2}, \qquad L(R_\mathrm{e}) = 2\pi \int_0^{R_\mathrm{e}} I_*\, t\, \mathrm{d}t = \frac{L}{2}, \tag{2.41}$$

where t is the integration radius on the projection plane, for any given los. Note that for a stellar component with a constant mass-to-light ratio, the half-light radius coincides with the half-mass radius, indeed

$$M_{*i}(R_{\mathrm{e}i}) = 2\pi \int_0^{R_{\mathrm{e}i}} \Sigma_{*i}\, t\, \mathrm{d}t = \frac{M_{*i}}{2}. \tag{2.42}$$

This is not true when the mass-to-light ratio depends on the position, as occurs in general for the total stellar distribution, so that the total R_e encloses $L/2$, but not $M_*/2$ in general. We stress now an important point: the relation between R_e and all the $R_{\mathrm{e}i}$ of the stellar components is not trivial, and in fact R_e can not be directly determined once all the $R_{\mathrm{e}i}$ are known, (as we show in Section 3.2.3, in particular see the Footnote 2 therein). Moreover, from eq. (2.41), and recalling that $L = \sum_i L_i$ (eq. 2.3), we prove that

$$L(R_\mathrm{e}) = \frac{\sum_i L_i}{2} = \sum_i \frac{L_i}{2} = \sum_i L_i(R_{\mathrm{e}i}), \tag{2.43}$$

but also, since $I_* = \sum_i I_{*i}$,

$$L(R_\mathrm{e}) = 2\pi \int_0^{R_{\mathrm{e}i}} \sum_i I_{*i}\, t\, \mathrm{d}t = \sum_i \left(2\pi \int_0^{R_{\mathrm{e}i}} I_{*i}\, t\, \mathrm{d}t \right) = \sum_i L_i(R_\mathrm{e}). \tag{2.44}$$

Nevertheless, although $\sum_i L_i(R_{\mathrm{e}i}) = \sum_i L_i(R_\mathrm{e})$, we stress that $R_\mathrm{e} \neq R_{\mathrm{e}i}$, which can be different for each stellar component. Finally, we define an *aperture* velocity dispersion, as the luminosity-weighted velocity dispersion $\sigma_{\mathrm{los}\mathscr{L}}$ integrated over an aperture radius xR_e (given by a fraction x of the effective radius R_e), and luminosity-averaged, so that

$$\sigma_0^2 = \frac{\int_0^{xR_\mathrm{e}} I_* \sigma_{\mathrm{los}\mathscr{L}}^2\, t\, \mathrm{d}t}{\int_0^{xR_\mathrm{e}} I_*\, t\, \mathrm{d}t}. \tag{2.45}$$

---

[2] For an ellipsoidal system, we can define also a *circularised* effective radius $\langle R_\mathrm{e} \rangle$ when the system is observed EO, which is useful in the next Chapters. It is related to R_e of the same model in the spherical limit (or when observed FO) by the identity

$$\langle R_\mathrm{e} \rangle = \sqrt{q} R_\mathrm{e}. \tag{2.40}$$

Besides, in the EO projection of an ellipsoidal system, the isophotal flattening coincide with the intrinsic flattening.

2.5 Summary

We have shown the sum rules to combine structural and dynamical properties of multicomponent systems, based on the assumption that each stellar component is implicitly described by a specific distribution function (usually depending on two integrals of motion). We now have the framework necessary to determine the solution of the Jeans equations, and the projected properties, for the whole multicomponent stellar system, once the solutions for the single stellar components in the total gravitational potential are known. Investigations of galaxy properties can be based on such galaxy models, as mentioned in Chapter 1. Nevertheless, an extensive exploration of the model parameter space would be impossible, due to the large number of parameters, increasing with the number of matter components; indeed, for each (stellar and DM) density distribution, unless the gravitational potential produced is known analytically, a numerical evaluation of the potential is necessary, and can require a lot of computational time. To overcome these bottlenecks of a numerical implementation, we proceeded in two directions. In the next Chapter, we present in depth the *scaling approach*, developed in order to fix the minimum possible number of structural parameters before the computation of the potentials and the solution of the Jeans equations, and then to have the flexibility to vary the maximum possible number of model parameters in post-processing. Then, in Chapter 4, we present several methods for the evaluation of the potential components which allow to drastically reduce the computational time.

Chapter 3

The scaling approach

We show how, thanks to the full use of the scaling operations allowed by the Poisson and the Jeans equations, and by the projection formulae, it is possible to calculate a set of scaled (dimensionless) solutions, and then to build an arbitrarily large family of models, just by combining the solutions in this set with suitable weights. For this purpose the numerical procedure is organised in two main parts: in the Potential & Jeans Solver, the potential associated to each density component is calculated, and the Jeans equations are solved for each stellar component in each potential component; in the Post-processing, the mass and luminosity weights are assigned, the kinematical decompositions imposed, and the projections performed. The numerical procedure is described in depth in its basic (an reproducible) idea, with some references to the implementation in JASMINE2, when necessary for more clearness.

Caravita C., Ciotti L. and Pellegrini S., 2020, IAUS

Caravita C., Ciotti L. and Pellegrini S., 2021, MNRAS

3.1 $N \times (N+2)$ systems of Jeans equations

We recognise that the Jeans equations (2.10), at fixed total potential Φ, are invariant to a mass scaling of the density ρ_{*i}, i.e. at fixed Φ the derived velocity fields would be independent of the value of M_{*i}. However, as Φ contains also ϕ_{*i}, eqs. (2.10) obviously are *not* invariant to such scaling. Nevertheless, recalling that $\Phi = \sum_j \phi_j$, we are allowed to split the Jeans equations (2.10) with respect to the contribution of each potential ϕ_j. We write the $N \times (N+2)$ systems of equations for the stellar densities ρ_{*i} in the potentials ϕ_j,

$$\begin{cases} \dfrac{\partial \rho_{*i}\sigma_{ij}^2}{\partial z} = -\rho_{*i}\dfrac{\partial \phi_j}{\partial z}, \\[2ex] \dfrac{\partial \rho_{*i}\sigma_{ij}^2}{\partial R} = \rho_{*i}\dfrac{\Delta_{ij}}{R} - \rho_{*i}\dfrac{\partial \phi_j}{\partial R}, \end{cases} \tag{3.1}$$

and their solutions

$$\rho_{*i}\sigma_{ij}^2 = \int_z^\infty \rho_{*i}\frac{\partial \phi_j}{\partial z'}\,\mathrm{d}z', \qquad \rho_{*i}\Delta_{ij} = R\left(\frac{\partial \rho_{*i}\sigma_{ij}^2}{\partial R} + \rho_{*i}\frac{\partial \phi_j}{\partial R}\right), \tag{3.2}$$

with $\rho_{*i}\sigma_{ij}^2 \to 0$ for $z \to \infty$. The Jeans equations in this form do have important scaling properties that will be exploited in Section 3.2. We note that, here and in the following, the double subscript ij does not refer to a tensorial nature, but just identifies the solution of the i-th stellar component in the j-th potential component.

Leaving aside for the moment the scaling properties of eqs. (3.1) and (3.2), it is clear that the sums

$$\sigma_i^2 = \sum_j \sigma_{ij}^2, \qquad \Delta_i = \sum_j \Delta_{ij}, \tag{3.3}$$

are the solution of eqs. (2.10). This can be demonstrated, first by summing over j the $N+2$ eqs. (3.1) and their solutions (3.2) for a given ρ_{*i}, and comparing the resulting expressions with eqs. (2.10) and (2.12), and then by proving that the solution of equation (2.10) is unique from the imposed boundaries.

An important point is in order here. Despite the apparent similarity of the decomposition of σ_i^2 and Δ_i performed in eqs. (3.1) over the $N+2$ potential components ϕ_j, with the decomposition of σ^2 and Δ performed in eqs. (2.10) over the N stellar components ρ_{*i}, there is a fundamental conceptual difference between the two decompositions. In fact, eqs. (2.10) are *true* moments of the Collisionless Boltzmann Equation obeyed by the DFs f_i in the total potential Φ, and so they have a sort of autonomous physical meaning; eqs. (3.1), instead, are just a mathematical decomposition over the different ϕ_j of the Jeans equations for ρ_{*i}. As a consequence, phase-space consistency arguments apply to the solution of eqs. (2.10), but not to σ_{ij}^2 and Δ_{ij} separately: as far as the fields σ_i^2 and Δ_i are physically acceptable, the model is also acceptable, independently of the specific properties[1] of its components σ_{ij}^2 and Δ_{ij}.

---

[1] The situation is somewhat similar to that faced when decomposing a positive density distribution

A further dynamical quantity interested by a decomposition of the total potential surely deserves to be mentioned: the rotation curve in the equatorial plane is given in terms of the circular velocities v_{cj} of the mass components as

$$v_{\rm c}^2 = \sum_j v_{{\rm c}j}^2, \qquad v_{{\rm c}j}^2 = R\,\frac{\partial\phi_j(R, z=0)}{\partial R}, \tag{3.4}$$

as a direct consequence of eq. (2.8).

Finally, we apply this decomposition also to the Virial Theorem (in its scalar form, but the formulae can be easily extended to the tensorial form) of eq. (2.19). For each i-th stellar component in each the j-th potential component, it holds

$$2K_{ij} + W_{ij} = 0, \tag{3.5}$$

whose sums over j,

$$K_i = \sum_j K_{ij}, \qquad W_i = \sum_j W_{ij}, \tag{3.6}$$

satisfy eq. (2.19). K_{ij} and W_{ij} are defined from Appendix A, and in analogy with eqs. (2.20)–(2.22). In particular, here $K_{ij} = K_{\varphi ij} + \Pi_{ij}$, where $K_{\varphi ij}$ is the total azimuthal kinetic energy: since the kinematical decomposition of the azimuthal motions (see Section 2.3) is applied to the i-th velocity fields, and not to their ij-th decompositions, it has no sense here to split the $K_{\varphi ij}$ in its streaming and velocity dispersion contributions. In analogy with eqs. (2.22) and (2.24), we stress that W_{ij}, for the i-th stellar component in the j-th potential component, reads

$$W_{ij} = -4\pi \int_0^\infty \int_0^\infty \rho_{*i} \left(R\frac{\partial\phi_j}{\partial R} + z\frac{\partial\phi_j}{\partial z} \right) R\,{\rm d}R\,{\rm d}z, \tag{3.7}$$

while the gravitational energy is

$$U_{ij} = 4\pi \int_0^\infty \int_0^\infty \rho_{*i}\phi_j\, R\,{\rm d}R\,{\rm d}z, \tag{3.8}$$

from eq. (A.18). In particular, U_{ij} is symmetric from the *Reciprocity Theorem*, so that $U_{ij} = U_{ji}$, while W_{ij} is not, and, in general, $U_{ij} = W_{ij} + W_{ji}$. In case of self-gravity, i.e. $i = j$ in the current notation, it immediately turns out that $U_{ii}/2 = W_{ii}$: indeed the self-energy is usually defined as half of eq. (3.8). In the same manner, also the gravitational energy due to the interaction of a density ρ_{*i} and the total potential Φ is given by half of the corresponding integral of eq. (3.8), as shown in eq. (2.24). A deeper discussion on these properties of the gravitational energies is subject of the study introduced in Section 7.2, for the special case of a two-component galaxy model.

---

over some prescribed set of functions (e.g spherical harmonics), when the basis functions can present regions of negative densities.

3.2 Scaling procedure

We describe the scaling approach, with a particular focus on its numerical implementation. We distinguish three groups of model parameters, on the basis of their roles in the construction of a multicomponent model, and coherently we organise the numerical procedure in two logically distinct parts - the Potential & Jeans Solver and the Post-Processing (PP) -, as illustrated in the following Sections, and summarised in Fig. 3.1 and Table 3.1. The procedure is implemented in the numerical code JASMINE2 (see Appendix B for a technical description of the code), to which we refer sometimes specifically, but it can be implemented as well in similar numerical codes.

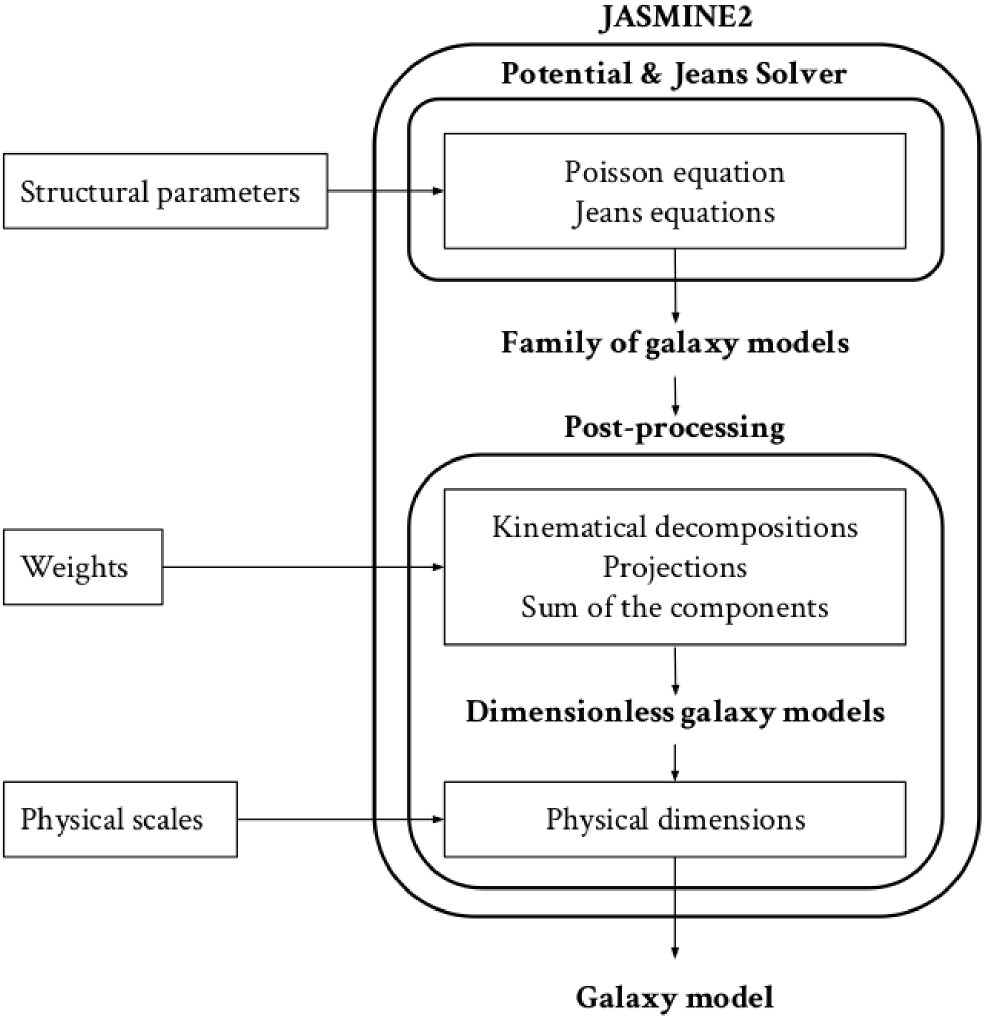

Figure 3.1: Scheme of the modelling procedure. The diagram summarises the procedure of construction of multicomponent galaxy models, based on the scaling approach described in Section 3.2, and implemented in the code JASMINE2. For details about the input parameters - structural parameters, weights, and physical scales -, see Table 3.1.

Potential & Jeans Solver Structural parameters	
Scaled stellar and DM densities	$\tilde{\rho}_{*i},\ \tilde{\rho}_{\rm h}$
Scale-length ratios	$\xi_i = \dfrac{r_{*i}}{r_*},\ \xi_{\rm h} = \dfrac{r_{\rm h}}{r_*}, \ldots$
Shape parameters	$q_i,\ q_{\rm h}, \ldots$
Post-Processing Weights	
Mass ratios	$\mathcal{R}_i = \dfrac{M_{*i}}{M_*},\ \mathcal{R}_{\rm h} = \dfrac{M_{\rm h}}{M_*},\ \mathcal{R}_{\rm BH} = \dfrac{M_{\rm BH}}{M_*}$
Mass-to-light ratios	$\Upsilon_{*i} = \dfrac{M_{*i}}{L_i}$
Kinematical decompositions	$k_i(\lambda_i, \delta_i)$
Post-Processing Physical Scales	
Total stellar mass	M_*
Total stellar scale-length	r_*

Table 3.1: Model parameters. The three main steps involved in the construction of a multicomponent galaxy model, listed from top to bottom in the order in which they are considered in a numerical implementation of the scaling approach, as shown in the diagram of Fig. 3.1. The meaning and the role of the parameters, separated in three groups, and the two main parts of the numerical procedure - the Potential & Jeans Solver and the Post-Processing (PP) - are described in detail in Section 3.2.

3.2.1 Model parameters

The three groups model parameters are presented in the following in the opposite order with respect to the list of Table 3.1. Here they are discussed following logical arguments, to introduce them as clearly as possible, while in Table they are listed in the order in which they are considered in a numerical implementation.

Physical scales

In the first group of model parameters, there are the physical scales M_* and r_*, meaning the total stellar mass and its scale-length. All the masses and lengths are normalised to M_* and r_*, respectively. In particular, all the density and potential components are made dimensionless by scaling them, respectively, with the normalisation coefficients

$$\rho_{\rm n} \equiv \frac{M_*}{4\pi r_*^3}, \qquad \phi_{\rm n} \equiv \frac{GM_*}{r_*}; \tag{3.9}$$

and the 2D numerical grid is normalised to r_*, so that we have $(\tilde{R}, \tilde{z})$, with $\tilde{R} \equiv R/r_*$ and $\tilde{z} \equiv z/r_*$. Such a scaled grid guarantees the same resolution, independently of the actual physical size of the model, measured by r_* (see Appendix B for details about the spatial grid implemented in JASMINE2). *Even though the physical scales are logically introduced first, the values of M_* and r_* (and so of ρ_n and ϕ_n) are fixed as the last step of the model construction, at the end of the PP.* In this way, different physical realisations (in total mass and size) can be obtained for the same multicomponent galaxy model.

Weights

In the second group of parameters there are the relative mass weights $\mathcal{R}_i \equiv M_{*i}/M_*$, $\mathcal{R}_\mathrm{h} \equiv M_\mathrm{h}/M_*$, $\mathcal{R}_\mathrm{BH} \equiv M_\mathrm{BH}/M_*$ of the different components, the mass-to-light ratios Υ_{*i}, and the parameters k_i appearing in eqs. (2.25) and (2.27) for the kinematical decomposition of the azimuthal motions. By definition

$$\sum_i \mathcal{R}_i = 1, \tag{3.10}$$

and in full generality we write

$$\rho_{*i} = \rho_\mathrm{n}\mathcal{R}_i\tilde{\rho}_{*i}, \qquad \rho_\mathrm{h} = \rho_\mathrm{n}\mathcal{R}_\mathrm{h}\tilde{\rho}_\mathrm{h}, \qquad \rho_* = \rho_\mathrm{n}\tilde{\rho}_* = \rho_\mathrm{n}\sum_i \mathcal{R}_i\tilde{\rho}_{*i}, \tag{3.11}$$

where $\tilde{\rho}_{*i}$ and $\tilde{\rho}_\mathrm{h}$ are the *scaled* (and dimensionless) density distributions, and $\tilde{\rho}_*$ is the dimensionless total stellar density, weighted for the mass ratios of the stellar components. Notice that, from the definition of ρ_n (eq. 3.9), the volume integrals of the dimensionless densities over the whole dimensionless numerical grid evaluate to 4π by construction. We mention here a subtlety which however can be very useful in applications: in principle all the stellar mass weights $\mathcal{R}_i$ are naturally positive numbers, describing everywhere positive density distributions; nevertheless, when interested in reproducing a physically meaningful ρ_* with the superposition of different components ρ_{*i}, regardless of their physical acceptability (as a purely mathematical decomposition), also negative ρ_{*i} can be considered, obtained with negative $\mathcal{R}_i$ (in Section 5.3, for example, we model such a case). The situation is conceptually similar to that explained in Section 3.1 for σ_i^2 and Δ_i (see also Footnote 1 therein). Similarly to eq. (3.11), for the gravitational potentials we have

$$\phi_{*i} = \phi_\mathrm{n}\mathcal{R}_i\tilde{\phi}_{*i}, \qquad \phi_\mathrm{h} = \phi_\mathrm{n}\mathcal{R}_\mathrm{h}\tilde{\phi}_\mathrm{h}, \qquad \phi_\mathrm{BH} = \phi_\mathrm{n}\mathcal{R}_\mathrm{BH}\tilde{\phi}_\mathrm{BH}, \tag{3.12}$$

and so

$$\phi_j = \phi_\mathrm{n}\mathcal{R}_j\tilde{\phi}_j, \qquad \Phi = \phi_\mathrm{n}\sum_j \mathcal{R}_j\tilde{\phi}_j. \tag{3.13}$$

Exploiting the normalisation of the potentials, the ij-th solution (3.2) of the Jeans equations can be written as

$$\sigma_{ij}^2 = \phi_\mathrm{n}\mathcal{R}_j\tilde{\sigma}_{ij}^2, \qquad \Delta_{ij} = \phi_\mathrm{n}\mathcal{R}_j\tilde{\Delta}_{ij}; \tag{3.14}$$

then the i-th solution σ_i^2 and Δ_i are given by sums over j from eq. (3.3), so that we define dimensionless $\tilde{\sigma}_{ij}^2$ and $\tilde{\Delta}_i$ as

$$\sigma_i^2 = \phi_\mathrm{n}\tilde{\sigma}_i^2 = \phi_\mathrm{n}\sum_j \mathcal{R}_j\tilde{\sigma}_{ij}^2, \qquad \Delta_i = \phi_\mathrm{n}\tilde{\Delta}_i = \phi_\mathrm{n}\sum_j \mathcal{R}_j\tilde{\Delta}_{ij}, \tag{3.15}$$

and in turn the total solution σ^2 and Δ are given by sums over i as in eq. (2.15), involving also the normalisation of the stellar densities in eq. (3.11).

Since $v_{\varphi i}$ and $\sigma^2_{\varphi i}$ derive from σ^2_i and Δ_i (see Section 2.3), their scaling derive directly from the previous equation, with the addition of the decomposition parameters k_i, which enter the sums over i. Moreover, for the energies entering the Virial Theorem in eq. (3.5) we have

$$K_{ij} = M_* \phi_{\rm n} \mathcal{R}_i \mathcal{R}_j \tilde{K}_{ij}, \qquad W_{ij} = M_* \phi_{\rm n} \mathcal{R}_i \mathcal{R}_j \tilde{W}_{ij}, \tag{3.16}$$

with K_i, W_i, and K, W, obtained from the sum rules of eqs. (3.6) and (2.23), respectively, in analogy with the velocities above. Finally, from the assumption of a constant mass-to-light ratio Υ_{*i} for each stellar component,

$$\nu_{*i} = \rho_{\rm n} \frac{\mathcal{R}_i}{\Upsilon_{*i}} \tilde{\rho}_{*i}, \qquad L_i = \frac{\mathcal{R}_i}{\Upsilon_{*i}} M_*, \tag{3.17}$$

where obviously the luminosity density follows the shape of the scaled mass density $\tilde{\rho}_{*i}$: in case of constant Υ_{*i}, indeed, the dimensionless luminosity density corresponds to $\tilde{\rho}_{*i}$. *The values of the weights are chosen in PP, because a change in their values, and in the kinematical decompositions, does not require to recompute the potentials and solve again the Jeans equations.* This possibility allows for a fast construction of different models belonging to the same family, defined below.

Structural parameters

A family of models is characterised by the choice of the third group of parameters, to be performed at the beginning of the model construction: the structural parameters of the scaled density components $\tilde{\rho}_{*i}$ and $\tilde{\rho}_{\rm h}$, that in full generality we indicate with the symbols $\xi_i \equiv r_{*i}/r_*$ and $\xi_{\rm h} \equiv r_{\rm h}/r_*$ for the different scale-lengths, and with q_i and $q_{\rm h}$ for other parameters that determine the shape of the scaled densities (e.g. the flattenings in case of ellipsoidal density distributions). *The values of the structural parameters must be assigned in order to run the Potential and Jeans Solver, and in general a change in some of their values requires a new computation of the potentials and of the Jeans solutions.*

3.2.2 The Potential & Jeans Solver

For a chosen set of values for the structural parameters, the scaled Jeans equations are solved from eqs. (3.2) and (3.14), for each scaled density $\tilde{\rho}_{*i}$ in each scaled potential $\tilde{\phi}_j$. In practice, for N assigned scaled stellar components $\tilde{\rho}_{*i}$ and a scaled DM halo $\tilde{\rho}_{\rm h}$, the Potential & Jeans Solver first computes the $N+2$ scaled potentials $\tilde{\phi}_{*i}$, $\tilde{\phi}_{\rm h}$, and $\tilde{\phi}_{\rm BH}$, and the relative *forces* (space-derivatives); then solves the $N \times (N+2)$ pairs of scaled Jeans equations (3.1), one for each $\tilde{\rho}_{*i}$ in the potential $\tilde{\phi}_j$, over the dimensionless grid $(\tilde{R}, \tilde{z})$. Thus the scaled fields $\tilde{\sigma}^2_{ij}$ and $\tilde{\Delta}_{ij}$ are obtained. The possibility to solve eq. (3.1) without choosing $\mathcal{R}_i$ and $\mathcal{R}_j$ is due to the fact that, on one hand, the weights $\mathcal{R}_i$ appear linearly in both sides of eqs. (3.1); on the other hand, $\tilde{\sigma}^2_{ij}$ and $\tilde{\Delta}_{ij}$ scale linearly with $\mathcal{R}_j$, once the boundary condition is fixed to zero at infinity.

When the analytical expression of the gravitational potential produced by a specific density distribution is not known, a numerical evaluation is required, and many different techniques have been developed. The details of the numerical methods implemented in our code JASMINE2 are given in Sections 4.2 and 4.4 (see also Appendix B); here we mention them for completeness. First of all, when available, the analytical potential is used; in this regard, JASMINE2 is supplied with a continuously updated *library* of analytical density-potential pairs available in the literature. For any choice of the density distribution, it is always possible to perform a fully numerical computation of the potential through the 2D integration over the cylindrical grid in terms of complete elliptic integrals of the first kind $\mathbf{K}$. Unfortunately, exact analytical potentials are known only in few cases, and the latter very accurate fully numerical computation is quite time-expensive. For these reasons, we have also implemented the Chandrasekhar formula for ellipsoidal distributions, and a formula based on zeroth-order Bessel function of the first kind J_0 for discs; both imply a 1D integration, allowing for a quite fast computation. Moreover, for ellipsoidal distributions, we can exploit analytical homoeoidally expanded density-potential pairs, in particular for almost spherical ellipsoids.

3.2.3 The Post-Processing

As described in the previous Section, for a given multicomponent model of assigned $\tilde{\rho}_{*i}$, $\tilde{\rho}_{\rm h}$, and with a central BH, the Potential & Jeans Solver gives the solution $\tilde{\sigma}_{ij}^2$ and $\tilde{\Delta}_{ij}$ of the scaled form of eq. (3.1). The $N+2$ solutions for each the stellar component in all the potential components are then combined in PP, with the assignment of the mass ratios $\mathcal{R}_j$, so that the solution σ_i^2 and Δ_i of eq. (2.10) for ρ_{*i} is obtained, according to eq. (3.15). At this stage, as discussed in Section 2.3, the PP performs a positivity check of $\tilde{\Delta}_i$ and $\tilde{\Delta}_i + \tilde{\sigma}_i^2$. In case of negativity of the latter quantity, a new choice of the weights $\mathcal{R}_j$ is made, until positivity is reached: if positivity cannot be obtained for acceptable choices of $\mathcal{R}_j$, then the multicomponent model is discarded as unphysical; if instead $\tilde{\Delta}_i + \tilde{\sigma}_i^2$ is nowhere negative for some choice of $\mathcal{R}_j$, the sign of $\tilde{\Delta}_i$ influences the choice of a suitable kinematical decomposition (in Sections 5.1 and 5.2, some illustrative cases are shown).

Once the mass weights are assigned and the kinematical decomposition formula is chosen, the PP requires the decomposition parameter k_i, that gives the scaled azimuthal velocity fields $\tilde{v}_{\varphi i}$ and $\tilde{\sigma}_{\varphi i}$. In full generality, we define each decomposition parameter as

$$k_i(R, z) = \lambda_i \delta_i(R, z), \tag{3.18}$$

where λ_i is a constant weight, and $\delta_i(R, z)$ is a position-dependent function; the constant Satoh parameter is obtained with $\delta_i = 1$ and $\lambda_i = k_i$. The benefit of this factorisation is due to the fact that the projection formula of $\tilde{v}_{\varphi i}$, as in equation (2.31), for a given $\delta_i(R, z)$ scales with λ_i, so that we can set the value of λ_i *after* having computed the projection integral. As projections represent the second most time-consuming step, the possibility to choose (and change) λ_i after projections is a significant advantage. Note that, at variance with what happens for the fields $\tilde{\sigma}_i^2$, $\tilde{\Delta}_i$, $\tilde{v}_{\varphi i}^2$ and $\tilde{\sigma}_{\varphi i}^2$, the mass weights

$\mathcal{R}_j$ enter the expression of $\tilde{v}_{\varphi i}$ under a square root (see eqs. 2.25 and 2.27). This implies that the weights $\mathcal{R}_j$ must be chosen before calculating the projections that use $v_{\varphi i}$. The effective radius $R_{\rm e}$ of the total stellar distribution is obviously another important quantity that can not be obtained as a linear combination of the effective radii of the stellar components, as mentioned in Section 2.4.2, and it can only be computed after the choice of the weights $\mathcal{R}_i$ and Υ_{*i}[2]. Summarising, the possibility to modify the values of $\mathcal{R}_j$ in PP, allowed by the ij-decomposition, concern all the internal (i.e. non projected) quantities, and the projected quantities with the exception of $v_{\rm los}$, $\sigma_{\rm los}$ and $R_{\rm e}$. Once we have obtained the internal and projected fields of each ρ_{*i}, they are combined to calculate the *total* (mass- and luminosity-weighted) internal and projected fields of ρ_* (respectively from eqs. 2.15, 2.16, and eq. 2.39).

Finally, it is possible to arbitrarily set the physical scales M_* and r_* (determining also $\rho_{\rm n}$ and $\phi_{\rm n}$), giving physical dimensions to the model.

3.3 Summary

A *family* of multicomponent galaxy models is defined by the choice of N scaled stellar density components $\tilde{\rho}_{*i}$, a scaled DM halo $\tilde{\rho}_{\rm h}$, and a central BH. The Potential & Jeans Solver computes the associated scaled potentials $\tilde{\phi}_j$, and then solves the $N \times (N+2)$ systems of Jeans equations in their scaled form. In the subsequent PP, specific values of the mass ratios $\mathcal{R}_i$, $\mathcal{R}_{\rm h}$, $\mathcal{R}_{\rm BH}$, and of the mass-to-light ratios Υ_{*i}, and the kinematical decompositions with the parameters k_i, are fixed, thus defining a specific model in the same family. The solution of the Jeans equations for the total density distribution is recovered as (mass- or luminosity-) weighted sums of the scaled solutions, and the projections along a given line-of-sight are performed. The values of the total stellar mass M_* and of the scale-length r_* complete the construction of the model. In practice, we set the *total* mass and size, scaling the whole galaxy model, without changing its internal structure and dynamics, neither the relative contributions in mass and luminosity of the

---

[2] Given that the projection of a dimensionless density distribution $\tilde{\rho}_{*i}$ gives the dimensionless surface density $\tilde{\Sigma}_{*i}$, we can define the projected mass enclosed within a circular radius $xR_{\rm e}$ (defined as in eq. 2.45) as

$$\tilde{M}_{*i}(x\tilde{R}_{\rm e}) = \int_0^{x\tilde{R}_{\rm e}} \tilde{\Sigma}_{*i}\,\tilde{t}\,{\rm d}\tilde{t}\,, \tag{3.19}$$

where $\tilde{R}_{\rm e} = R_{\rm e}/r_*$ and $\tilde{t} \equiv t/r_*$. The integral of $\tilde{M}_{*i}(x\tilde{R}_{\rm e})$ over the projection plane results in $\tilde{M}_{*i} = 4\pi$, and $\tilde{M}_{*i}(\tilde{R}_{{\rm e}i}) = 2\pi$, which directly provides the value of $\tilde{R}_{{\rm e}i} = R_{{\rm e}i}/r_*$. In order to calculate $\tilde{R}_{\rm e}$, instead, we write $L(R_{\rm e}) = L/2$ as follows:

$$\rho_{\rm n} r_*^3 \sum_i \frac{\mathcal{R}_i}{\Upsilon_{*i}} \tilde{M}_{*i}(\tilde{R}_{\rm e}) = \frac{M_*}{2} \sum_i \frac{\mathcal{R}_i}{\Upsilon_{*i}}\,, \tag{3.20}$$

which immediately leads to

$$\sum_i \frac{\mathcal{R}_i}{\Upsilon_{*i}} \tilde{M}_{*i}(\tilde{R}_{\rm e}) = 2\pi \sum_i \frac{\mathcal{R}_i}{\Upsilon_{*i}}\,, \tag{3.21}$$

showing that the estimate of $\tilde{R}_{\rm e}$ requires to set the weights $\mathcal{R}_i$ and Υ_{*i} of each stellar component, and it can not be calculated directly from the values of $\tilde{R}_{{\rm e}i}$.

different matter components. This is also convenient, for example, to make a certain model lie on the Scaling Laws (e.g. Faber and Jackson, 1976; Kormendy, 1977) and the Fundamental Plane (Dressler et al., 1987; Djorgovski and Davis, 1987) for ETGs. The modelling procedure, as also implemented in JASMINE2, is summarised in the scheme of Fig. 3.1, and the model parameters involved are listed in Table 3.1.

There are at least two significant advantages in this procedure, when compared with a straightforward integration of the Jeans equations for a multicomponent galaxy model. First, the gravitational potentials of each stellar component and of the DM halo need not to be recalculated every time the weights are changed in PP; thus the run of the most time-expensive part of the numerical procedure is required just once for all the models in the same family. Second, the possibility to choose the weights in PP allows for a fast exploration of the parameter space (that can be very large for multicomponent models). Qualitatively, the $N \times (N+2)$ ij-th scaled solutions of the Jeans equations, for all the i-th density components in all the j-th potential components, can be interpreted as *basis vectors* that are successively linearly combined with different weights, to obtain a specific solution belonging to a family of multicomponent models.

Chapter 4

Density models, evaluation of the potentials and tests

A large number of density models have been studied (and published in the literature) to describe the matter distributions in astrophysical systems, both for the luminous and the dark matter. We summarise all the density models that have been included in the code JASMINE2, with the relative analytical potential when known. Then, we present the different methods for the numerical computation of the potentials that have been implemented in JASMINE2, with particular reference to the evaluation of the potentials produced by the density models of our library. The standard method for axisymmetric density distributions is the integration formula in terms of elliptic integrals; for ellipsoidal systems, we also recall the Chandrasekhar integral formula, and the analytical solutions in homoeoidal approximation (for small flattening of the ellipsoidal density distribution); finally, for factorised discs, we present a new general formula in terms of Bessel functions. All these methods have been widely tested, and applied to the construction of the galaxy models presented as applications in this Thesis work. Moreover, JASMINE2 has been used to test the reliability of the solution of the Jeans equations in homoeoidal expansion, for increasing flattening.

Caravita C., Ciotti L. and Pellegrini S., 2021, MNRAS

Caravita C. and Ciotti L., In preparation

4.1 Density models

The following list of density profiles, and density-potential pairs when analytical potentials are known, represents the current *library* from which we can choose for the construction of our models with JASMINE2, meaning for the definition of the stellar and DM distributions. The library is continuously updated with other density profiles according to the needs. In full generality, we adopt the normalisations introduced in the previous Chapter, so that all the masses and the lengths are normalised, respectively, to M_* and r_*, and consequently all the densities and the potentials to $\rho_{\rm n}$ and $\phi_{\rm n}$, respectively: the formulae for the density and the potentials are then recast, and given for general $\tilde{\rho}(\tilde{R},\tilde{z})$ and $\tilde{\phi}(\tilde{R},\tilde{z})$. The models are ordered according to their shapes: in Section 4.1.1, spheroidal density models, characterised by a flattening parameter q; in Section 4.1.2, other special flattened systems; in Section 4.1.3, exponential discs, infinitely thin and with two possible vertical stratifications. The complete list is summarised in Table 4.1, where it is also specified whether the analytical potential is known, and the numerical methods to calculate the potential available for each specific density model. With regard to discs, in Section 4.4, other radial profiles are mentioned (which are not included in JASMINE2 at this stage) that can describe the surface density of infinitely thin discs, or can be combined with one of the two vertical profiles.

The description of the density profiles (density-potential pairs in some cases) does not intend to be exhaustive, and some references are suggested for more details; moreover, general and quite comprehensive references on the topic can be, for instance, B&T08, Ciotti (2021).

4.1.1 Spheroidal systems

γ-models The family of γ-models (Dehnen, 1993; Tremaine et al., 1994) is characterised by a parameter $0 \leq \gamma < 3$, and its generalisation to the ellipsoidal case gives

$$\tilde{\rho}(\tilde{R},\tilde{z}) = \frac{(3-\gamma)\xi}{q\, m^{\gamma}(\xi+m)^{4-\gamma}}, \qquad m^2 = \tilde{R}^2 + \frac{\tilde{z}^2}{q^2}, \tag{4.1}$$

describing the Hernquist (1990) model and the Jaffe (1983) model, respectively, for $\gamma = 1$ and $\gamma = 2$. We recall that (here and below) ξ is the semi-major axis of the ellipsoid, normalised to r_*, and q is the flattening, i.e. the ratio between the semi-minor and semi-major axes of the ellipsoid. In the spherical limit, the analytical potential is

$$\tilde{\phi}(s) = \begin{cases} -\dfrac{1}{(2-\gamma)\xi}\left[1-\left(\dfrac{s}{\xi+s}\right)^{2-\gamma}\right], & \gamma \neq 2 \\[2ex] -\dfrac{1}{\xi}\ln\left(\dfrac{\xi+s}{s}\right), & \gamma = 2, \end{cases} \tag{4.2}$$

with $s = \sqrt{\tilde{R}^2+\tilde{z}^2}$ the normalised spherical radius. We mention, as a useful link with observations, that for a spherical Jaffe model, and in the assumption of constant mass-

Density model	Analytical	Chandrasekhar	Homoeoidal	Bessel
		Spheroidal systems		
γ-models	✓ $q = 1$	✓	✓	
NFW	✓ $q = 1$	✓	✓	
Quasi-iso. sphere ($q = 1$)	✓			
Perfect ellipsoid		✓	✓	
Plummer	✓ $q = 1$	✓	✓	
Einasto	✓ $q = 1$	✓		
de Vaucouleurs		✓		
		Other flattened systems		
MN	✓			
Satoh	✓			
Binney log potential	✓			
		Exponential discs		
Razor-thin exp				✓
Double-exponential				✓
Pseudo-isothermal exp				✓

Table 4.1: Density models and suitable methods for the evaluation of the potentials. All the density models presented in Section 4.1 are listed. On the right, it is specified whether the analytical potential is known, and other methods for its evaluation: the 1D numerical integration of the Chandrasekhar formula (Section 4.2.1) and the homoeoidal expansion (Section 4.2.2) for ellipsoidal systems; the 1D numerical integration based on Bessel functions for factorised discs (Section 4.4). Moreover, for all the density distributions, it is possible to calculate the associated potential with the standard 2D numerical integration based on elliptic integrals (eq. 4.23).

to-light ratio, the scale radius r_* is related to the effective radius by $R_\mathrm{e} \simeq 0.75\, r_*$ (see e.g. Jaffe, 1983; Ciotti and Ziaee Lorzad, 2018).

NFW model The Navarro-Frenk-White model (NFW, Navarro et al., 1996), in its ellipsoidal generalisation, is given by

$$\tilde{\rho}(\tilde{R}, \tilde{z}) = \frac{1}{q\, m(\xi + m)^2 f(c)}, \qquad f(c) = \ln(1 + c) - \frac{c}{1 + c}, \tag{4.3}$$

where the concentration $c = \xi_\mathrm{t}/\xi$ is the ratio between the truncation radius (enclosing the finite total mass) and the scale-length, both in units of r_*. In the spherical case, we have

$$\tilde{\phi}(s) = -\frac{1}{s\, f(c)} \ln\left(\frac{\xi + s}{s}\right). \tag{4.4}$$

Quasi-isothermal sphere The quasi-isothermal sphere is a spherical model of infinite mass,

$$\tilde{\rho}(s) = \frac{\xi^2}{\xi^2 + s^2}, \qquad \tilde{M}(s) = \xi^3 \left[\frac{s}{\xi} - \arctan\left(\frac{s}{\xi}\right) \right], \tag{4.5}$$

with $M(s) = M_* \mathcal{R} \tilde{M}(s)$, and circular velocity asymptotically constant at large radii, $v_{\mathrm{c}}^2 \sim \phi_{\mathrm{n}} \mathcal{R} \xi^2$. Due to the infinite mass, for this model we adopt $\mathcal{R} = \rho(0)/\rho_*(0)$, i.e. the density ratio at the centre, instead of the mass ratio. The gravitational potential is given by

$$\tilde{\phi}(s) = \xi^2 \left[\ln\left(\frac{\sqrt{\xi^2 + s^2}}{\xi} \right) + \frac{\arctan(s/\xi)}{s/\xi} - 1 \right], \tag{4.6}$$

where it is immediate to see that the big bracket represents ϕ/v_{c}^2, which can be an alternative convenient normalisation of the potential for this special model.

Perfect ellipsoid We write the density of the perfect ellipsoid, well-known for producing a potential of Stäckel form (de Zeeuw, 1985; de Zeeuw and Lynden-Bell, 1985), in the axisymmetric case, so that

$$\tilde{\rho}(\tilde{R}, \tilde{z}) = \frac{4\,\xi}{q\,\pi\,\left(\xi^2 + m^2\right)^2}. \tag{4.7}$$

Plummer The ellipsoidal generalisation of the Plummer (1911) sphere gives

$$\tilde{\rho}(\tilde{R}, \tilde{z}) = \frac{3\,\xi^2}{q\,\left(\xi^2 + m^2\right)^{5/2}}, \tag{4.8}$$

with associated potential, in the spherical limit, given by

$$\tilde{\phi}(s) = -\frac{1}{\sqrt{\xi^2 + s^2}}. \tag{4.9}$$

In the spherical limit, the previous models have been unified in a three-parameter family (see e.g. Hernquist, 1990; Zhao, 1996; Mo et al., 2010; Roncadelli and Galanti, 2021), with a **double power-law** density generically defined as

$$\rho(s) = \rho_0 s^{-\gamma} \left(1 + s^{\alpha}\right)^{\frac{\gamma - \beta}{\alpha}}, \tag{4.10}$$

describing each model with an appropriate constant ρ_0. In particular, for $\alpha = 1$, we obtain the γ-models when $\beta = 4$ (including the Hernquist model for $\gamma = 1$ and the Jaffe model for $\gamma = 2$), and the NFW model when $\beta = 3$ and $\gamma = 1$. Instead, for $\alpha = 2$ and $\gamma = 0$, we derive the family of so-called **β-models**, including the quasi-isothermal sphere, the modified Hubble sphere (not presented in this work), the Plummer sphere, and the spherical limit of the perfect ellipsoid, for $\beta = 2, 3, 4, 5$ respectively.

Einasto The Einasto (1965; see also Graham et al., 2006) profile is the three-dimensional counterpart of the Sérsic (1963) law applied to the internal density distribution, and it well reproduces the DM halos obtained from numerical simulations. Its ellipsoidal generalisation gives

$$\tilde{\rho}(\tilde{R}, \tilde{z}) = \frac{b_n^{3n}}{q\,n\,\xi^3 \Gamma(3n)}\,\mathrm{e}^{-b_n (m/\xi)^{1/n}}, \qquad b_n \simeq 3n - \frac{1}{3} + \frac{8}{1215n}, \tag{4.11}$$

with associated potential, in the spherical case, given by

$$\tilde{\phi}(s) = -\frac{1}{s}\left[1 - \frac{\Gamma(3n,x)}{\Gamma(3n)} + \frac{x^n\Gamma(2n,x)}{\Gamma(3n)}\right], \tag{4.12}$$

where $\Gamma(a) = \int_0^\infty t^{a-1}\mathrm{e}^{-t}\,\mathrm{d}t$ and $\Gamma(a,x) = \int_x^\infty t^{a-1}\mathrm{e}^{-t}\,\mathrm{d}t$ are the complete and the upper incomplete Gamma functions, respectively.

de Vaucouleurs The de Vaucouleurs (1948) profile, also known as '$R^{1/4}$' law, and special case of the Sérsic (1963) profile for $n = 4$, is widely used to describe the surface brightness of elliptical galaxies. From the deprojection formula of Mellier and Mathez (1987), an approximation of the Abel inversion formula, an axisymmetric density is derived:

$$\tilde{\rho}(\tilde{R},\tilde{z}) = \frac{B_n}{q\,\xi^3}\,\mathrm{e}^{-b_n(m/\xi)^{1/4}}\left(\frac{m}{\xi}\right)^{-0.855}, \tag{4.13}$$

where

$$B_n = \frac{b_n^{12-4\cdot0.855}}{4\,\Gamma(12-4\cdot0.855)}, \qquad b_n \simeq 2n - 0.324, \tag{4.14}$$

so that, for $n = 4$, $b_n \simeq 7.67$ and $B_n \simeq 588.637$. Note the similarity with the Einasto profile (eq. 4.11), except for the power-law term.

4.1.2 Other flattened systems

Miyamoto-Nagai The Miyamoto-Nagai model (MN, Miyamoto and Nagai, 1975) reads

$$\tilde{\rho}(\tilde{R},\tilde{z}) = \tilde{b}^2\frac{\tilde{a}\tilde{R}^2 + \left(\zeta + 2\sqrt{\tilde{z}^2+\tilde{b}^2}\right)\zeta^2}{\left(\tilde{R}^2+\zeta^2\right)^{5/2}\left(\tilde{z}^2+\tilde{b}^2\right)^{3/2}}, \tag{4.15}$$

$$\tilde{\phi}(\tilde{R},\tilde{z}) = -\frac{1}{\sqrt{\tilde{R}^2+\zeta^2}}, \qquad \zeta = \tilde{a} + \sqrt{\tilde{z}^2+\tilde{b}^2}, \tag{4.16}$$

depending on two scale-lengths, $\tilde{a}$ and $\tilde{b}$, both in units of r_*. For $\tilde{a} = 0$ it reduces to the Plummer sphere (eq. 4.8), and for $\tilde{b} = 0$ to the razor-thin Kuzmin-Toomre disc (Kuzmin 1956; Toomre 1963; see also Section 4.4).

Satoh Satoh (1980) derived a new model from the Plummer sphere, by differentiating the density-potential pair several times with respect to its scale parameter (i.e. ξ in eqs. 4.8 and 4.9) and then flattening it:

$$\tilde{\rho}(\tilde{R},\tilde{z}) = \frac{\tilde{a}\tilde{b}^2}{\zeta^3\left(\tilde{z}^2+\tilde{b}^2\right)}\left[\frac{1}{\sqrt{\tilde{z}^2+\tilde{b}^2}} + \frac{3}{\tilde{a}}\left(1 - \frac{\tilde{R}^2+\tilde{z}^2}{\zeta^2}\right)\right], \tag{4.17}$$

$$\tilde{\phi}(\tilde{R},\tilde{z}) = -\frac{1}{\zeta}, \quad \zeta = \sqrt{\tilde{R}^2+\tilde{z}^2+\tilde{a}\left(\tilde{a}+2\sqrt{\tilde{z}^2+\tilde{b}^2}\right)}. \tag{4.18}$$

Binney logarithmic potential B&T08 introduce an axisymmetric potential producing a circular velocity asymptotically constant at large radii, $v_\mathrm{c}^2 \sim \phi_\mathrm{n}\mathcal{R}$, for which they also derive the corresponding density:

$$\tilde{\rho}\big(\tilde{R},\tilde{z}\big) = \frac{\big(1+2q^2\big)\xi^2 + \tilde{R}^2 + \big(2-q^{-2}\big)\tilde{z}^2}{q^2\left(\xi^2+m^2\right)}, \qquad \tilde{\phi}\big(\tilde{R},\tilde{z}\big) = \frac{1}{2}\ln\left(\xi^2+m^2\right), \tag{4.19}$$

where for this special model q is the flattening of the potential distribution, and not of the density distribution. Moreover, in order to assure a nowhere negative density, $q > 1/\sqrt{2} \simeq 0.7$: approaching this limit, the density distribution presents a torus-like shape, becoming negative on the z-axis when the limit is reached.

4.1.3 Exponential discs

A radial exponential profile is commonly used to describe the surface density distribution of stellar and gaseous galactic discs. Here we present three cases of exponential discs: the infinitely thin disc, and two cases of vertical stratifications.

Razor-thin exponential disc Infinitely thin discs, defined only in the equatorial plane, represent the first approximation of thin stellar and gaseous galactic discs. The distribution

$$\tilde{\rho}\big(\tilde{R},\tilde{z}\big) = \frac{2\,\mathrm{e}^{-\tilde{R}/\tilde{a}}}{\tilde{a}^2}\delta(\tilde{z}) = \begin{cases} \dfrac{2\,\mathrm{e}^{-\tilde{R}/\tilde{a}}}{\tilde{a}^2}, & \tilde{z}=0 \\ 0, & \tilde{z}\neq 0. \end{cases} \tag{4.20}$$

is in fact a surface density, with scale-radius $\tilde{a}$, in units of r_*.

Double-exponential disc A simple model for a more realistic disc includes an exponential vertical profile, so that

$$\tilde{\rho}\big(\tilde{R},\tilde{z}\big) = \frac{\mathrm{e}^{-\tilde{R}/\tilde{a}-|\tilde{z}|/\tilde{b}}}{\tilde{a}^2\tilde{b}}, \tag{4.21}$$

with scale-length $\tilde{b}$, in units of r_*, typically much smaller than $\tilde{a}$.

Pseudo-isothermal exponential disc Another vertical stratification often employed gives

$$\tilde{\rho}\big(\tilde{R},\tilde{z}\big) = \frac{2^{2-n}}{\tilde{a}^2\tilde{b}\,\mathrm{B}\big(\frac{n}{2},\frac{n}{2}\big)}\mathrm{e}^{-\tilde{R}/\tilde{a}}\,\mathrm{sech}^n\big(\tilde{z}/\tilde{b}\big), \tag{4.22}$$

where we recall that $\mathrm{sech}^n(t) = \cosh^{-n}(t) = 2^n\mathrm{e}^{nt}/(1+\mathrm{e}^{2t})^n$, producing again an exponential vertical decline of the density distribution. We also recall (see Appendix C for more details) that the complete Beta function can be written in terms of the complete Gamma function, so that $\mathrm{B}\big(\frac{n}{2},\frac{n}{2}\big) = \Gamma\big(\frac{n}{2}\big)^2 = \Gamma(n)$, and, for example, it evaluates to π for $n=1$, and to 1 for $n=2$. This last is the most commonly used value for n when modeling exponential stellar and gaseous discs, describing the so-called *isothermal* sheet (Spitzer, 1942).

4.2 Methods to calculate the gravitational potential

In the previous Section, we have reported some analytical potentials associated to the respective mass densities. Unfortunately, only in few cases it is possible to recover the analytical expression for the potential, making it necessary to develop numerical procedures, complementing the analytical results. In this and the next Section, we present some techniques, whether well-known in the literature, or discussed specifically in this Thesis work, and all implemented in (and tested with) JASMINE2. They are summarised in Table 4.1, where it is also specified which methods can be used for each density model of the previous Section.

First of all, for axisymmetric distributions, in cylindrical coordinates, it is always possible to perform a fully numerical computation of the potential in terms of elliptic integrals. In the current notation, we recast the formula as follows:

$$\tilde{\phi}(\tilde{R},\tilde{z}) = -\frac{1}{\pi}\int_0^\infty\int_{-\infty}^\infty \mathbf{K}\left[\sqrt{\frac{4\tilde{R}\tilde{R}'}{\left(\tilde{R}+\tilde{R}'\right)^2+\left(\tilde{z}-\tilde{z}'\right)^2}}\right]\frac{\tilde{\rho}\left(\tilde{R},\tilde{z}\right)\,\tilde{R}'\,\mathrm{d}\tilde{R}'\,\mathrm{d}\tilde{z}'}{\sqrt{\left(\tilde{R}+\tilde{R}'\right)^2+\left(\tilde{z}-\tilde{z}'\right)^2}}, \tag{4.23}$$

where $\mathbf{K}$ is the complete elliptic integral of the first kind, related to the incomplete one by $\mathbf{K}(k) = F(\pi/2, k)$ (see e.g. B&T08; Ciotti 2021). The potential is evaluated as a 2D integration for each point $\left(\tilde{R},\tilde{z}\right)$, giving a very accurate solution, but at the price of a quite time-expensive computation (see Appendix B for more technical details).

To reduce the computational time required by the evaluation of the potentials, recalling that it is the most time-consuming part of the numerical procedure (as highlighted in Section 3), we have also implemented in JASMINE2 two faster 1D integration formulae: the Chandrasekhar formula for ellipsoidal distributions, and a formula based on Bessel functions for discs. Moreover, we can use analytical homoeoidally expanded density-potential pairs for some ellipsoidal distributions. In the following Sections we describe these three methods: we stress that, while the integration based on elliptic integrals (eq. 4.23) was already implemented in the first version of the code, JASMINE, and it was in fact the only numerical method available for the evaluation of the potentials, besides the use of analytical potentials for some density models, the further three methods represent a trait of the new version of the code, JASMINE2. In particular, for the Chandrasekhar formula (Section 4.2.1) and the homoeoidal expansion technique (Section 4.2.2), we briefly report formulae from other works, while a deeper discussion will be dedicated to factorised discs (Section 4.4), with a new method and original results presented.

4.2.1 Chandrasekhar formula for ellipsoidal models

We recall the Chandrasekhar integration formula for the evaluation of the gravitational potential produced by a generic density distribution stratified on ellipsoidal surfaces, in cartesian coordinates (x, y, z), with semi-axes $a \geq b \geq c \geq 0$ aligned with the coordinate system (see e.g. Chandrasekhar 1969; B&T08; Ciotti 2021):

$$\phi(\mathbf{x}) = -\pi G abc \int_0^\infty \frac{\Delta\psi \, \mathrm{d}\tau}{\sqrt{(a^2+\tau)(b^2+\tau)(c^2+\tau)}}, \tag{4.24}$$

where

$$\Delta\psi = \psi(\infty) - \psi(m_\tau) = 2\int_{m_\tau}^\infty \rho(t)\, t \, \mathrm{d}t, \tag{4.25}$$

and

$$t = \sqrt{\frac{x^2}{a^2} + \frac{y^2}{b^2} + \frac{z^2}{c^2}}, \qquad m_\tau = \sqrt{\frac{x^2}{a^2+\tau} + \frac{y^2}{b^2+\tau} + \frac{z^2}{c^2+\tau}} \tag{4.26}$$

are dimensionless parameters. In case of axisymmetric ellipsoid, so that $a = b$, $c = qa$, in cylindrical coordinates, and with the adoption of our usual normalisations (in analogy with the previous Section), we obtain

$$\tilde{\phi}(\tilde{R}, \tilde{z}) = -\frac{q}{4}\int_0^\infty \frac{\widetilde{\Delta\psi}\, \mathrm{d}\lambda}{(1+\lambda)\sqrt{(q^2+\lambda)}}, \qquad \lambda = \frac{\tau}{r_*}, \tag{4.27}$$

where now

$$\widetilde{\Delta\psi} = 2\int_{m_\tau}^\infty \tilde{\rho}(t)\, t\, \mathrm{d}t, \tag{4.28}$$

with t and m_τ unchanged with respect to eq. (4.26), but they can be recast as

$$t = \sqrt{\tilde{R}^2 + \frac{\tilde{z}^2}{q^2}}, \qquad m_\tau = \sqrt{\tilde{R}^2 + \frac{\tilde{z}^2}{q^2+\lambda}}. \tag{4.29}$$

We see, in the following, the expression of $\widetilde{\Delta\psi}$ for some ellipsoidal distributions in our library, obtained through the analytical solution of eq. (4.28) with the respective density $\tilde{\rho}$ from Section 4.1. For details, we refer especially to Ciotti (2021).

For the γ-models, from eq. (4.1), we have

$$\widetilde{\Delta\psi} = \begin{cases} \dfrac{2}{q(2-\gamma)\xi}\left\{1 - \dfrac{m_\tau^{2-\gamma}}{(\xi+m_\tau)^{3-\gamma}}\left[m_\tau + (3-\gamma)\xi\right]\right\}, & \gamma \neq 2 \\ \\ \dfrac{2}{q\xi}\left[\ln\left(\dfrac{\xi+m_\tau}{m_\tau}\right) - \dfrac{\xi}{\xi+m_\tau}\right], & \gamma = 2; \end{cases} \tag{4.30}$$

for the NFW model, from eq. (4.3),

$$\widetilde{\Delta\psi} = \frac{2}{q(\xi+m_\tau)f(c)}; \tag{4.31}$$

for the perfect ellipsoid, from eq. (4.7),

$$\widetilde{\Delta\psi} = \frac{4\,\xi}{q\,\pi\,(\xi^2+m_\tau^2)}; \tag{4.32}$$

for the Plummer model, from eq. (4.8),

$$\widetilde{\Delta\psi} = \frac{2\,\xi^2}{q\,\left(\xi^2 + m_\tau^2\right)^{3/2}}; \tag{4.33}$$

for the Einasto model From eq. (4.11),

$$\widetilde{\Delta\psi} = \frac{2\,b_n^n}{q\,\xi\,\Gamma(3n)}\,\Gamma\left[2n,\, b_n\left(\frac{m_\tau}{\xi}\right)^{1/n}\right]; \tag{4.34}$$

finally, for the de Vaucouleurs deprojected profile, from eq. (4.13), we obtain

$$\widetilde{\Delta\psi} = \frac{0.4174}{q\,\xi}\,\Gamma\left[4.58,\, 7.67\left(\frac{m_\tau}{\xi}\right)^{1/4}\right], \tag{4.35}$$

where the numerical values derive from the values given for $\tilde{\rho}$.

4.2.2 Homoeoidally expanded formulae for ellipsoidal models

For density distributions stratified on homoeoidal surfaces, such as ellipsoidal distributions, both the density and the associated gravitational potential can be approximated by an expansion in the limit of small flattening, through the so-called *homoeoidal expansion technique* (Ciotti and Bertin, 2005). We see the *homoeoidally expanded* density distributions, and the related analytical expressions for the expanded potentials, for some density models of Section 4.1; we report also the expression for the density distribution for reasons that will be clear in the following. In case of axisymmetric density distributions, the expansion up to the linear order in the flattening q can be written as

$$\tilde{\rho}\big(\tilde{R}, \tilde{z}\big) = \tilde{\rho}_0(s) + (1-q)\tilde{\rho}_1(s) + (1-q)\tilde{R}^2\tilde{\rho}_2(s), \tag{4.36}$$

and, in analogy, the potential produced is

$$\tilde{\phi}\big(\tilde{R}, \tilde{z}\big) = -\big[\tilde{\phi}_0(s) + (1-q)\tilde{\phi}_1(s) + (1-q)\tilde{R}^2\tilde{\phi}_2(s)\big], \tag{4.37}$$

where the usual normalisations are adopted, and $s = \sqrt{\tilde{R}^2 + \tilde{z}^2}$ is the normalised spherical radius, accordingly to Section 4.1. For details about the homoeoidal expansion technique, we refer to Ciotti and Bertin (2005), and also CMPZ21 (where in particular axisymmetric Jaffe models are treated); here we recall the meaning of the functions in eqs. (4.36) and (4.37) for coherence with our use of the formulae:

$$\begin{aligned}
\tilde{\rho}_0(s) &= \tilde{\rho}(s), \\
\tilde{\rho}_1(s) &= \tilde{\rho}(s) + s\frac{\mathrm{d}\tilde{\rho}(s)}{\mathrm{d}s}, \\
\tilde{\rho}_2(s) &= -\frac{1}{s}\frac{\mathrm{d}\tilde{\rho}(s)}{\mathrm{d}s};
\end{aligned} \tag{4.38}$$

$$\begin{aligned}\tilde{\phi}_0(s) &= \frac{1}{s}\int_0^s \tilde{\rho}(t)t^2\,\mathrm{d}t + \int_s^\infty \tilde{\rho}(t)t\,\mathrm{d}t,\\ \tilde{\phi}_1(s) &= -\frac{2}{3s^2}\int_0^s \tilde{\rho}(t)t^4\,\mathrm{d}t + \frac{1}{3}\int_s^\infty \tilde{\rho}(t)t\,\mathrm{d}t,\\ \tilde{\rho}_2(s) &= \frac{1}{s^5}\int_0^s \tilde{\rho}(t)t^4\,\mathrm{d}t.\end{aligned} \tag{4.39}$$

These are functions of the radius s and the scale-length ξ, while the dependence on the flattening q is contained in eqs. (4.36) and (4.37). The homoeoidally expanded density-potential pair recovers the exact spherical case for $q = 1$, and indeed $-\tilde{\phi}_0(s)$ is the potential associated to $\tilde{\rho}_0(s)$, while it diverges from the ellipsoidal density-potential pair for increasing flattening (decreasing q). We highlight here two possible interpretations (and applications) of the homoeoidal expansion: on one side, homoeoidally expanded density-potential pairs can be intended as approximations of true ellipsoidal systems, and this can be useful to deal with analytical potentials (even if approximated), when otherwise numerical computations would be required; on the other side, homoeoidally expanded models can be intended as *proper* models, regardless of the approximation of ellipsoidal systems. In Section 4.3, we see some tests involving the homoeoidal expansion technique, and in Chapters 5 and 6 we use it in applications.

In the following, we give the analytical solutions of eqs. (4.38) and (4.39) for some models of interest, for which also the homoeoidal expansions have been included in JASMINE2 (see Table 4.1). From Ciotti and Bertin (2005), we recast the formulae for γ-models in eqs. (4.1)–(4.2). For $\gamma \neq 2$ (including the Hernquist model for $\gamma = 1$), we have

$$\begin{gathered}\tilde{\rho}_0(s) = \frac{(3-\gamma)\xi}{s^\gamma(\xi+s)^{4-\gamma}}, \qquad \tilde{\rho}_1(s) = -\frac{\xi(3-\gamma)\big[\xi(\gamma-1)+3s\big]}{s^\gamma(\xi+s)^{5-\gamma}},\\ \tilde{\rho}_2(s) = \frac{\xi(3-\gamma)(\xi\gamma+4s)}{s^{2+\gamma}(\xi+s)^{5-\gamma}};\end{gathered} \tag{4.40}$$

$$\begin{aligned}\tilde{\phi}_0(s) &= \frac{1}{\xi(2-\gamma)}\left[1-\left(\frac{s}{\xi+s}\right)^{2-\gamma}\right],\\ \tilde{\phi}_1(s) &= -\frac{1}{3\xi(2-\gamma)}\left\{1+\Big[\xi(\gamma-3)-s\Big]s^{2-\gamma}(\xi+s)^{\gamma-3}\right\}\\ &\quad -\frac{2\xi^2(3-\gamma)}{3s^3}\mathrm{B}\left(5-\gamma,-1;\frac{s}{\xi+s}\right),\\ \tilde{\phi}_2(s) &= \frac{\xi^2(3-\gamma)}{s^5}\mathrm{B}\left(5-\gamma,-1;\frac{s}{\xi+s}\right),\end{aligned} \tag{4.41}$$

exploiting the incomplete Beta function $\mathrm{B}(a,b;x)$. In Appendix C, some considerations about the Beta function and its numerical implementation are discussed. In particular, since the incomplete Beta function is often called in numerical languages in its regularised form, it must be $b > 0$, which fails in the expressions of $\tilde{\phi}_1$ and $\tilde{\phi}_2$ above, since $b = -1$: the incomplete Beta function is recast for this situation in terms of Hypergeometric function

${}_2\mathrm{F}_1$ (eq. C.3). The case $\gamma = 2$, i.e. Jaffe model, is solved separately and can be found with detailed discussions in CMPZ21:

$$\tilde{\rho}_0(s) = \frac{\xi}{s^2(\xi+s)^2}, \qquad \tilde{\rho}_1(s) = -\frac{\xi(\xi+3s)}{s^2(\xi+s)^3}, \qquad \tilde{\rho}_2(s) = \frac{2\xi(\xi+2s)}{s^4(\xi+s)^3}; \tag{4.42}$$

$$\begin{aligned} \tilde{\phi}_0(s) &= \frac{1}{\xi}\ln\left(\frac{\xi+s}{s}\right), \\ \tilde{\phi}_1(s) &= -\frac{s^2+2\xi s+4\xi^2}{3s^2(\xi+s)} + \frac{1}{3\xi}\ln\left(\frac{\xi+s}{s}\right) + \frac{4\xi^2}{3s^3}\ln\left(\frac{\xi+s}{\xi}\right), \\ \tilde{\phi}_2(s) &= \frac{\xi(2\xi+s)}{s^4(\xi+s)} - \frac{2\xi^2}{s^5}\ln\left(\frac{\xi+s}{\xi}\right). \end{aligned} \tag{4.43}$$

For the perfect ellipsoid in eq. (4.7), we obtain

$$\tilde{\rho}_0(s) = \frac{4\xi}{\pi(\xi^2+s^2)^2}, \qquad \tilde{\rho}_1(s) = \frac{4\xi\left(\xi^2-3s^2\right)}{\pi(\xi^2+s^2)^3}, \qquad \tilde{\rho}_2(s) = \frac{16\xi}{\pi(\xi^2+s^2)^3}; \tag{4.44}$$

$$\begin{aligned} \tilde{\phi}_0(s) &= \frac{2\arctan(s/\xi)}{\pi s}, \qquad \tilde{\phi}_1(s) = \frac{4\xi^2\arctan(s/\xi)}{\pi s^3} - \frac{2\xi\left(2\xi^2+s^2\right)}{\pi s^2(\xi^2+s^2)}, \\ \tilde{\phi}_2(s) &= \frac{2\xi\left(3\xi^2+s^2\right)}{\pi s^4(\xi^2+s^2)} - \frac{6\xi^2\arctan(s/\xi)}{\pi s^5}. \end{aligned} \tag{4.45}$$

Finally, for the Plummer model in eqs. (4.8)–(4.9),

$$\tilde{\rho}_0(s) = \frac{2\xi^2}{(\xi^2+s^2)^{5/2}}, \qquad \tilde{\rho}_1(s) = \frac{\xi^2\left(3\xi^2-12s^2\right)}{(\xi^2+s^2)^{7/2}}, \qquad \tilde{\rho}_2(s) = \frac{15\xi^2}{(\xi^2+s^2)^{7/2}}; \tag{4.46}$$

$$\begin{aligned} \tilde{\phi}_0(s) &= \frac{1}{\sqrt{\xi^2+s^2}}, \qquad \tilde{\phi}_1(s) = \frac{\xi^2\left(2\xi^2+3s^2\right)}{s^2(\xi^2+s^2)^{3/2}} - \frac{2\xi^2\,\mathrm{arcsinh}(s/\xi)}{s^3}, \\ \tilde{\phi}_2(s) &= \frac{3\xi^2\,\mathrm{arcsinh}(s/\xi)}{s^5} - \frac{\xi^2\left(3\xi^2+4s^2\right)}{s^4(\xi^2+s^2)^{3/2}}. \end{aligned} \tag{4.47}$$

For the formulae of the last two models, we thank especially the courtesy of Luca Ciotti and Antonio Mancino. Some similarities between the formulae above are not surprising, indeed these models, in their spherical limit, belong to a same three-parameter family with a double power-law density distribution, as shown in eq. (4.10). In particular, the expressions for $\tilde{\rho}_0$ and $\tilde{\phi}_0$ are the exact spherical density-potential pair, as mentioned above, and they are necessarily in agreement with the formulae for the ellipsoidal distributions of Section 4.1, when $q = 1$.

4.3 Tests for spheroidal systems

We show some proves of the accuracy of the numerical methods seen so far for the computation of the gravitational potentials, and of the numerical solution of the Jeans equations, with the code JASMINE2. First, in Section 4.3.1, we check the numerical integrations based on elliptic integrals and on the Chandrasekhar formula for the evaluation of the potential of spherical systems, against analytical potentials, and we check the numerical integration of the Jeans equations against analytical results. Second, once we have verified these numerical procedures, in Section 4.3.2, we use numerical potentials to study the reliability of the homoeoidal expansion, for ellipsoidal systems with increasing degree of flattening.

For this set of tests, for simplicity, we use a single-component Jaffe stellar model: the density distribution is given by eq. (4.1), for $\gamma = 2$, and $\xi = 1$ (i.e. the scale-length r_* is taken as the scale-length of the density model itself). We choose an ellipsoidal density distribution, and in particular a Jaffe profile, for the following reasons. First, we verify the accuracy of two numerical methods for the evaluation of the potential (see Table 4.1): via elliptic integrals from eq. (4.23), and via the Chandrasekhar formula of eq. (4.27) with $\widetilde{\Delta\psi}$ from eq. (4.30); both the numerical integrations are compared with the analytical expression of the potential in case of spherical symmetry (eq. 4.2 with $\gamma = 2$, $\xi = 1$). Second, for a spherical Jaffe model, also the solution of the Jeans equations is known analytically (see Jaffe 1983; see also e.g. Ciotti and Ziaee Lorzad 2018, and references therein), allowing for a check of the numerical solution.

Once we have verified the accuracy of the numerical potential and of the numerical integration of the Jeans equations with JASMINE2, the Jaffe model is also suitable for a further twofold experiment, addressed to verify the reliability of homoeoidal expansion techniques for increasing flattening of the ellipsoid. On one side, we solve numerically the Jeans equations for a *true* ellipsoidal model (eq. 4.1) with numerical potential, and for an *homoeoidally expanded* (up to the linear terms in the flattening) density-potential pair (as reported in eqs. 4.36, 4.37, and 4.42, 4.43, from CMPZ21): we show how well the internal structure and dynamics are reproduced in the second case, for increasing flattening. We recall that the most time-consuming part of the modelling procedure is the numerical evaluation of the potential (when using elliptic integrals), thus the possibility to exploit an approximated analytical expression for the potential can be a significant advantage. On the other side, in CMPZ21, the analytical solution of the Jeans equations in homoeoidal expansion is also given: in this case, only the linear order in the flattening is taken into account, while a numerical integration of the Jeans equations for an homoeoidally expanded density-potential pair (again up to the linear terms in the flattening) keep also the quadratic flattening terms in the solution. We compare the expanded solution with the numerical solution of JASMINE2, checking the importance of quadratic flattening terms. Summarising, we compare the solutions of the Jeans equations obtained in three different ways: a *true ellipsoidal* density model, with numerical potential and numerical integration of the Jeans equations (that we call in the following figures 'num'); an *hybrid* solution, obtained from an homoeoidally expanded density-potential pair, with numerical solution of the Jeans equations ('hom-num'); a *pure homoeoidal* solution, obtained from an homoeoidally expanded density-potential pair, with homoeoidally expanded solution of the Jeans equation ('hom'). We expect an increasing discrepancy of the 'hom-num', and more of the 'hom', results with respect to the pure 'num', for increasing flattening.

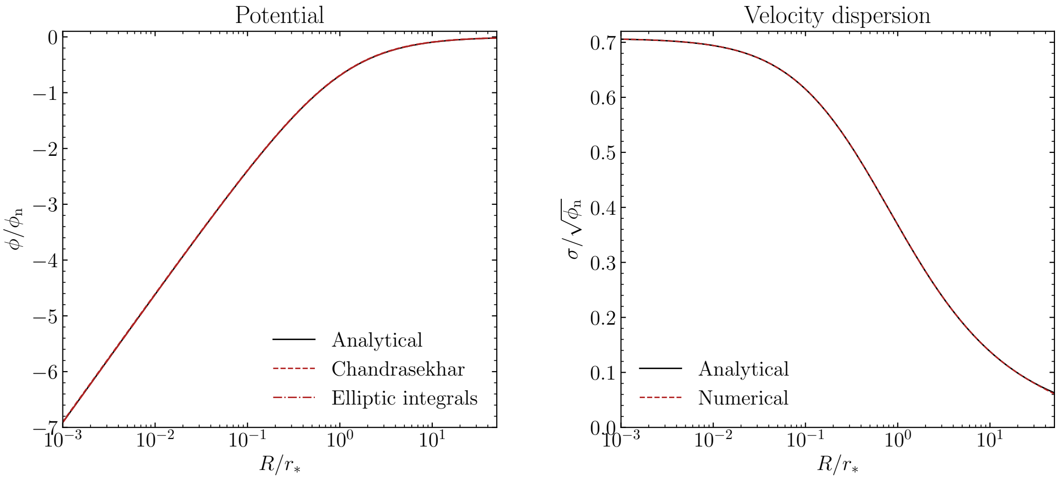

Figure 4.1: Radial profiles in the equatorial plane $\left(\tilde{R}, \tilde{z} = 0\right)$ of the (dimensionless) gravitational potential ϕ (left), and velocity dispersion σ (right), for a spherical Jaffe model. On the left, the numerical evaluations of ϕ with JASMINE2, in terms of elliptic integrals and with the Chandrasekhar formula, are compared with the analytical potential. Then, the numerical integration of the Jeans equations in JASMINE2 gives σ, compared with the analytical solution in the right plot, and an everywhere zero Δ, as expected.

In the following, we discuss some figures showing the comparisons discussed. We do not analyse here the structural and dynamical properties of the models, while we focus only on the tests in interest; details on the features typical of Jaffe models (and other models) can be found in the applications of Chapters 5 and 6. Similar tests have been performed also for other density models of our library, as we mention below. Finally, we only mention here that similar tests have been performed for two-component models, to check the multicomponent modelling procedure, for different degrees of flattening of the ellipsoidal distributions, and also in presence of the central BH. In particular, we refer to the so-called JJ model in Ciotti and Ziaee Lorzad (2018) for the spherical case, and to the JJe model in CMPZ21 for the ellipsoidal case (see also the models used in Section 5.1 and in Chapter 6). For the sake of conciseness, we do not show figures for these cases, limiting the treatment to the spherical and flattened single-component cases.

4.3.1 Spherical case: test of numerical procedures

We show in Fig. 4.1 the radial profile on the equatorial plane of the gravitational potential produced by a spherical Jaffe density model, comparing the numerical evaluation of JASMINE2, both in terms of elliptic integrals and with the Chandrasekhar formula, with the analytical potential. With a suitable resolution of the spatial grid $\left(\tilde{R}, \tilde{z}\right)$, and of the integration variable λ of eq. (4.27) (see Appendix B), both the numerical methods are able to perfectly reproduce the potential.

We then solve the Jeans equations numerically with JASMINE2, comparing the solution with the well-known analytical solution for spherical Jaffe model. We recall that for a spherical system $\Delta = 0$, and so only σ is given. In the right plot of Figure 4.1, we show how well the numerical integration of the vertical Jeans equation recovers the analytical σ; of course, we have also verified that the numerical integration of the radial Jeans equation gives an everywhere zero Δ.

Similar checks on the potential of spherical systems have been performed also for other density models, strengthening our confidence in the numerical implementation in JASMINE2 of the two methods. Finally, some checks on the integration via elliptic integrals, and on the solution of the Jeans equations, had been already performed with the first version of the code, JASMINE, by comparison with the analytical results of Smet et al. (2015). In this regard, we recall that the numerical integration in terms of elliptic integrals, and the integration of the Jeans equations, in cylindrical coordinates, in JASMINE2 are based on the same approach of the original JASMINE, but extended to the treatment of multiple stellar and DM components.

4.3.2 Increasing flattening: test of homoeoidal expansion

After the checks on the numerical techniques implemented in JASMINE2, we now consider the numerical results as *true*, and we use them to verify the reliability of homoeoidally expanded results. We recall that the homoeoidal expansion of an ellipsoidal distribution recovers the exact analytical results in the limit case of spherical symmetry ($q = 0$), and diverges from the true ellipsoidal model for increasing flattening. The homoeoidal expansion technique is then valid only for small flattening of the ellipsoid, and in particular it imposes a flattening $q \geq 2/3$, in order to assure an everywhere positive density distribution. For illustrative purposes, in Fig. 4.2, the difference of the ellipsoidal Jaffe density distribution (solid black line) and its expansion is shown, for $q = 0.9, 0.8, 0.7$. While on the equatorial plane the isodensity contours are substantially the same, along (and near) the z-axis the outer expanded contours differ from the elliptical shape for increasing q; for $q < 2/3$ this behaviour would lead to regions of negative density. More details, and similar figures, can be found in CMPZ21, in particular see Figure 2 therein.

We see now the difference between the numerical and the expanded potentials related to the Jaffe density models above. The numerical potentials are calculated by JASMINE2 through the Chandrasekhar formula, because of its enormous rapidity with respect to the integration based on elliptic integrals (see Appendix B). As well known, a generic oblate density distribution produces a gravitational potential with a rounder distribution: then the potentials produced by the almost spherical density distributions of Fig. 4.2 are essentially spherical. For this reason, in Fig. 4.3, we do not show the isopotential contours, but the radial profiles on the equatorial plane; moreover, since the main differences between the curves occur in the innermost regions, a logarithmic radial scale allows to better appreciate them (besides, an inset plot shows a zoom in at small radii). The curves for the three models with $q = 0.9, 0.8, 0.7$ are overlapped, and lower profiles refer to lower q, since more flattened systems produce more negative potentials:

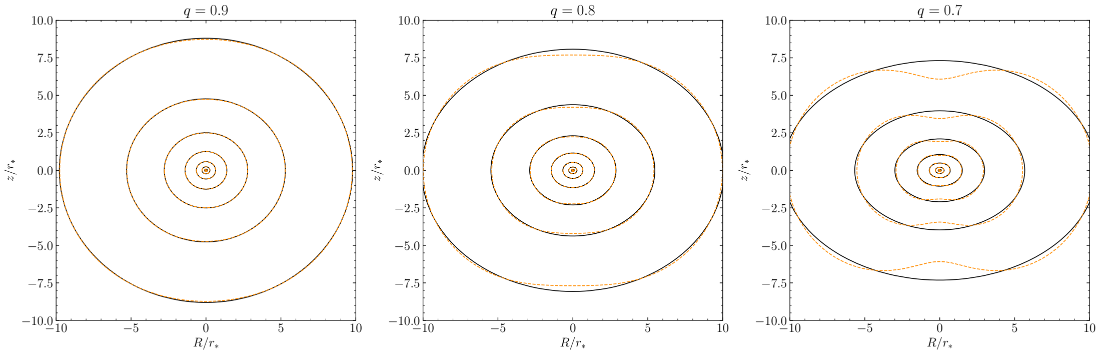

Figure 4.2: Isodensity contours on the meridional plane $(\tilde{R}, \tilde{z})$ for true ellipsoidal Jaffe density distributions (solid black lines) and the respective homoeoidal expansions (dashed orange lines), for increasing flattening $q = 0.9$, 0.8, 0.7, from left to right. The isodensity contours represent the dimensionless $\rho/\rho_{\rm n}$, with values spaced by 1 dex.

of course, at large radii the profiles are nearly the same, while at small radii we can see the effect of the increasing flattening. The expanded potentials (dashed orange lines) reproduce very well the true potentials (solid black lines), with small discrepancies in the innermost regions, and only slightly increasing the discrepancy for increasing flattening.

In Figure 4.4, the radial profiles on the equatorial plane of the solutions of the Jeans equations, σ and $\sqrt{\Delta}$, are shown for the three Jaffe models with $q = 0.9$, 0.8, 0.7, comparing the three cases 'num', 'hom-num' and 'hom', already introduced. Let us analyse first the difference between the numerical integration of the Jeans equations for a true ellipsoidal density model with numerical potential ('num', solid black lines), and for an homoeoidally expanded density-potential pair ('hom-num', dot-dashed green lines): the increasing discrepancies for increasing flattening are apparent. In particular, the velocity dispersion σ is perfectly reproduced for $q = 0.9$, and still with very good agreement for $q = 0.8$, up to an error of few per cent for $q = 0.7$; the differences in $\sqrt{\Delta}$, instead, are larger, from few per cent for $q = 0.9$, to about 10% for $q = 0.8$, up to about 20% for $q = 0.7$. Caution is then required when using homoeoidally expanded density-potential pairs to approximate true ellipsoidal distributions. We recall that, however, homoeoidally expanded models can also be intended as *proper* models, regardless of the approximation of ellipsoidal systems (as explained in Section 4.2.2): in this case, the solution of the Jeans equations called 'hom-num' is the true numerical solution for this density-potential pair. Especially for this case, it is interesting to see how well the analytical integration of the Jeans equations, truncated to the linear order in flattening ('hom', dashed orange lines), reproduce the numerical integration, which in contrast extends to second-order ('hom-num', dot-dashed green lines). The difference between the two profiles is not significant, neither for σ nor for $\sqrt{\Delta}$, for any degree of flattening shown. This means that, when interested in homoeoidally expanded density-potential pairs, quadratic flattening terms can be neglected also in the solution of the Jeans equations, without a significant loss in accuracy.

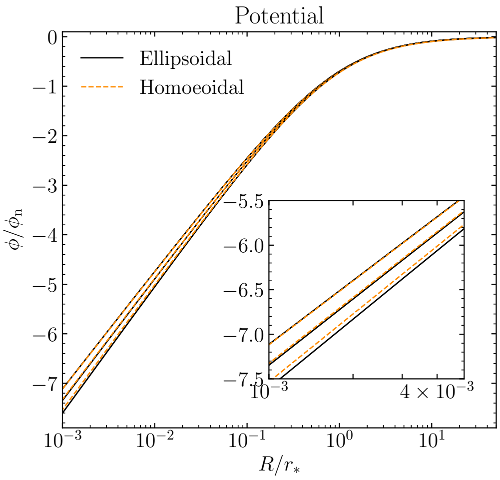

Figure 4.3: Radial profiles in the equatorial plane $\left(\tilde{R}, \tilde{z} = 0\right)$ of the gravitational potential ϕ, normalised to ϕ_n: the numerical potential (Chandrasekhar formula) for true ellipsoidal Jaffe density distributions (solid black lines) are compared with the respective homoeoidal expansions (dashed orange lines), for increasing flattening $q = 0.9$, 0.8, 0.7. The curves for the three degrees of flattening are overlapped, and lower profiles refer to lower q. The inset plot shows a zoom in at small radii, to better appreciate the differences between the curves.

We stress that the results about the homoeoidal expansion technique are obtained for Jaffe models and can be different for other ellipsoidal distributions, at least quantitatively.

4.4 Gravitational potential of factorised discs with Bessel functions

We consider a generic axisymmetric system, in cylindrical coordinates, with a mass density distribution $\rho(R, z)$, producing a gravitational potential $\phi(R, z)$, and satisfying the Poisson equation $\nabla^2\phi = 4\pi G\rho$. If we apply the Hankel transform (or Fourier-Bessel transform) to both sides of the Poisson equation, we can write the potential in terms of Bessel functions (see e.g. Toomre 1963; Casertano 1983; B&T08; Ciotti 2021; Bovy 2022; see also Jackson 1998), as follows:

$$\begin{cases} \phi(R, z) = -2\pi G \displaystyle\int_0^\infty \mathrm{J}_0(kR)\,\mathrm{d}k \int_{-\infty}^{\infty} \hat{\rho}(k, z')\,\mathrm{e}^{-k|z-z'|}\,\mathrm{d}z', \\ \hat{\rho}(k, z') = \displaystyle\int_0^\infty \rho(R', z')\,\mathrm{J}_0(kR')R'\,\mathrm{d}R', \end{cases} \tag{4.48}$$

where J_0 is the zeroth-order Bessel function of the first kind, and $\hat{\rho}$ is the zeroth-order Hankel transform of the function ρ.

From a computational point of view, eqs. (4.48) correspond to a 3D integral, to be evaluated in each position of a numerical grid in the coordinates (R, z). Therefore,

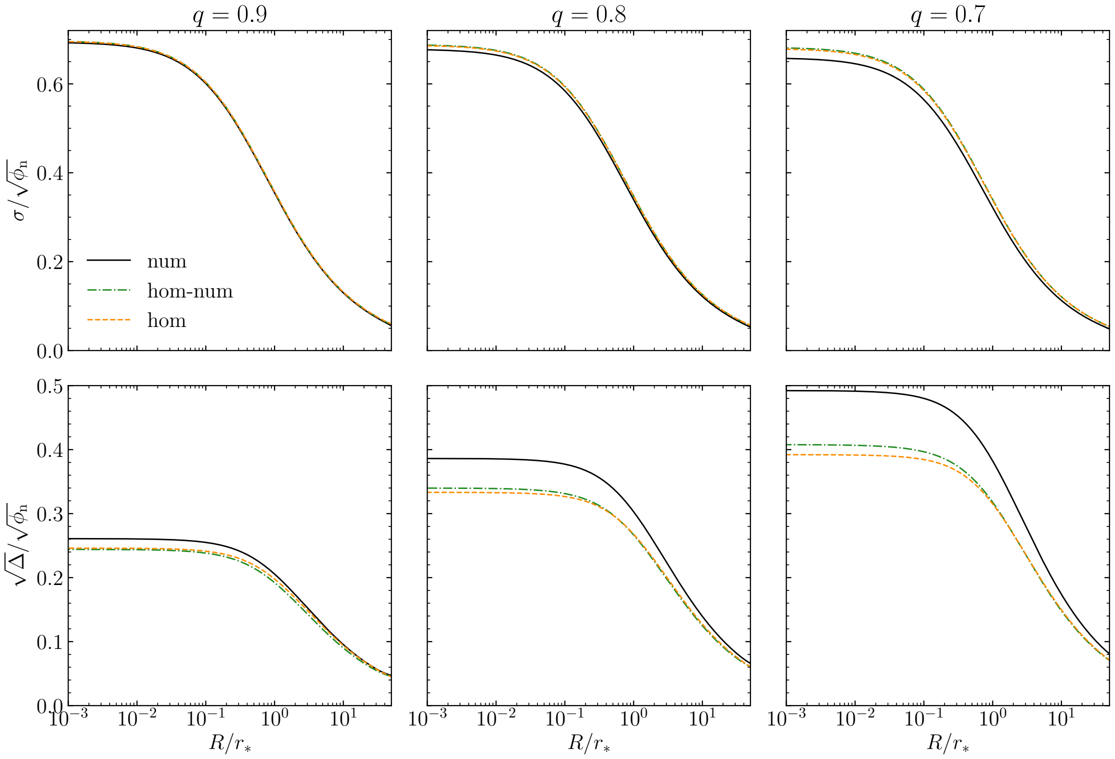

Figure 4.4: Radial profiles in the equatorial plane $\left(\tilde{R}, \tilde{z} = 0\right)$ of the solution of the Jeans equations for Jaffe models with flattening $q = 0.9$, 0.8, 0.7 from left to right. The first row shows the velocity dispersion σ, and the second row $\sqrt{\Delta}$, both normalised to $\sqrt{\phi_n}$, obtained in three different ways: a *true ellipsoidal* density model, with numerical potential and numerical integration of the Jeans equations ('num', solid black lines); an *hybrid* solution, obtained from an homoeoidally expanded density-potential pair, with numerical solution of the Jeans equations ('hom-num', dot-dashed green lines); a *pure homoeoidal* solution, obtained from an homoeoidally expanded density-potential pair, with homoeoidally expanded solution of the Jeans equation ('hom', dashed orange lines).

in the hypothesis of the same grid resolution for the integration and for sampling the potential, with N grid points in each variable, a number of operations of the order of $\mathcal{O}(N^5)$ is required. The situation slightly improves if $\hat{\rho}$ is known analytically, reducing the order of operations to $\mathcal{O}(N^4)$. Finally, if the density ρ can be written in factorised form, i.e. it is separable in cylindrical coordinates, and also the integral over z' can be solved analytically, eqs. (4.48) reduce to a 1D integral, and the order of operations drops to $\mathcal{O}(N^3)$. This may allow to save a remarkable amount of computational time. The case already mentioned may appear quite rare and of limited use, but fortunately it is not, since factorised density distributions are often employed in modelling stellar and gaseous galactic discs (e.g. Casertano, 1983; Kuijken and Gilmore, 1989; Jurić et al., 2008; Smith et al., 2015, among many others). In a very first approximation, stellar and gaseous discs are often considered as zero-thickness discs, i.e. in the simplest and idealised case of infinitely thin (a.k.a. razor-thin) discs, thanks to the very small vertical extension with respect to their radial size. More realistic models, however, assume a - albeit small - non-zero constant scale-height, characterising the vertical distribution of matter off-plane, and allowing for a full 3D treatment of the gravitational potential produced. The reality is even more complex, and in fact stellar and gaseous discs in disc galaxies are observed to have radial-dependent scale-height.

In this Section, we take into consideration some radial and vertical density distributions which can be multiplied to produce a variety of factorised discs, in the assumption of constant scale-height. For each radial distribution we report in Appendix D the analytical Hankel transform $\hat{\rho}$, and for each vertical stratification we give in the following the analytical solution of the integral over z' in eq. (4.48), so that the evaluation of the potential of these factorised discs requires only the 1D integration over k. Writing the potential in terms of Bessel function J_0, of course, is not the only way for a numerical computation, and sometimes it could not be the most convenient. In the previous Section 4.2, we have seen other numerical methods, from the most general and direct approach through the complete elliptic integral of the first kind $\mathbf{K}$, to methods especially suitable for spheroidal systems. In case of infinitely thin axisymmetric discs, an alternative formulation have been proposed by Cuddeford (1993), through the superposition of infinitely thin homoeoids. For example, in case of infinitely thin exponential disc, the potential is evaluated in terms of modified Bessel functions K_0 or K_1, with an important advantage with respect to eq. (4.48): the modified Bessel functions K_0 and K_1 decrease exponentially and are always positive towards infinity, while the Bessel function J_0 has a slow and oscillatory decline, requiring more care in the numerical evaluation. Another formulation for the potential of infinitely thin axisymmetric discs has been proposed by Evans and de Zeeuw (1992), exploiting Stieltjes transforms, and avoiding the use of Bessel functions. Nevertheless, eq. (4.48), while firstly developed for discs of zero-thickness, is easily extended to discs with a generic vertical stratification of matter, which allows to have density distributions factorised in cylindrical coordinates, and, for many commonly used radial and vertical distributions, the integrals in R' and z' have analytical solutions: this allows to reduce the problem to a 1D integration, with evident benefit in computational time, as mentioned above.

In Section 4.4.1, we introduce the integration formulae to evaluate the potential in case of factorised discs in cylindrical coordinates. In Section 4.4.2, we focus in particular on two important vertical stratifications, beyond the case of zero-thickness: the exponential profile and the 'pseudo-isothermal' profile, decreasing as a power-law of the sech. We also recall a variety of widely used radial distributions (Appendix D): the exponential and the Kuzmin discs, the disc of truncated constant density, the Maclaurin disc, and the finite, truncated, and truncated Mestel discs. Remarkable combinations of these radial and vertical distributions are, for example, the double-exponential disc and the pseudo-isothermal exponential disc, presented in Section 4.1.3 (and already implemented in JASMINE2). The analytical terms for the potential of the double-exponential disc are given also in Kuijken and Gilmore (1989) and Cuddeford (1993), so we verify their results. Instead, the potential of an exponential disc with a vertical pseudo-isothermal profile is mentioned in Casertano (1983) and Kuijken and Gilmore (1989), but the analytical solution of the integral in z' is not given there, neither in other references of our knowledge. In Cuddeford (1993), also the gaussian vertical density profile is analysed, and the analytical solution of the integral in z' is shown, which could be included in our scheme of building of factorised discs with no effort. As a proof of the new method in terms of Bessel functions, in Section 4.4.3, we show the comparison of the numerical evaluation of the potential with respect to the integration based on elliptic integrals (method already verified, as shown in Section 4.3), for the two factorised discs named as double-exponential and pseudo-isothermal exponential discs.

In the following, to avoid an excessively cumbersome notation, we still omit the usual normalisations of the masses and the lengths to the M_* and r_*, respectively, but their addition would be straightforward.

4.4.1 Factorised density distributions

We consider axisymmetric density distributions that can be written in factorised form in cylindrical coordinates, so that

$$\rho(R,z) = \rho_0\, A(R)\, B(z), \tag{4.49}$$

with a generic normalisation ρ_0. Therefore the 3D integral of eqs. (4.48) is separable, and it is naturally divided in a part depending only on R' and a part depending only on z', giving

$$\phi(R,z) = -2\pi G\rho_0 \int_0^\infty \hat{A}(k)\, \hat{B}(k,z)\, \mathrm{J}_0(kR)\, \mathrm{d}k, \tag{4.50}$$

where

$$\hat{A}(k) = \int_0^\infty A(R')\, \mathrm{J}_0(kR')R'\, \mathrm{d}R', \qquad \hat{B}(k,z) = \int_{-\infty}^\infty B(z')\, \mathrm{e}^{-k|z-z'|}\, \mathrm{d}z'. \tag{4.51}$$

This formulation for the potential becomes especially useful when the two functions $\hat{A}(k)$ and $\hat{B}(k,z)$ have analytical forms, i.e. when the radial distribution $A(R)$ has analytical Hankel transform $\hat{A}(k)$, and the vertical distribution $B(z)$ allows an analytical solution of the integral over z', giving $\hat{B}(k,z)$. In this case, eq. (4.50) reduces to a 1D integration over k. We see some radial and vertical distributions allowing for such simplification: in particular, we discuss some profiles widely used in the description of stellar galactic discs. In Appendix D, we report the Hankel transforms for some radial density distributions, while the description of the vertical structure deserves a deeper discussion, in the next Section. Then the analytical radial and vertical functions $\hat{A}(k)$ and $\hat{B}(k,z)$ can be combined to calculate the gravitational potential for different factorised discs from eq. (4.50).

Of course, a special case of factorised distribution is the razor-thin disc, the simplest and idealised representation of a (finite or infinite) disc, defined only in the equatorial plane ($z = 0$) and with no matter off-plane. In this case, we have

$$B(z) = \delta(z) = \frac{\delta(z/h_\mathrm{d})}{h_\mathrm{d}}, \tag{4.52}$$

where the second equivalence comes directly from a property of the δ function, and in general $h_{\rm d}$ represents the scale-height of the disc. In case of infinitely thin disc, naturally, the density distribution reduces to a surface density distribution, thus the definition of a scale-height has no physical meaning, and $h_{\rm d}$ only represents an arbitrary algebraic constant (at variance with the cases discussed in the next Section). It is immediate to prove that the solution of $\hat{B}(k,z)$ in eq. (4.51), for $B(z)$ from eq. (4.52), provides

$$\hat{B}(k,z) = {\rm e}^{-k|z|}, \tag{4.53}$$

recasting a well-known result (see e.g. B&T08; Ciotti 2021).

4.4.2 Two important vertical stratifications

Besides the razor-thin case, we also investigate two vertical density stratifications, which find wide applications in the description of realistic (thin and thick) galactic discs: the exponential vertical distribution and the 'pseudo-isothermal' sheet. We consider a generic vertical distribution, written as $B(z) = g(z/h_{\rm d})$, with g being an *even* function of z, i.e. $B(z) = B(-z)$. It is immediate to show that it holds also $\hat{B}(k,z) = \hat{B}(k,-z)$. We can write eq. (4.51) as

$$\hat{B}(k,z) = h_{\rm d} \int_{-\infty}^{\infty} g(t)\, {\rm e}^{-\gamma|\zeta - t|}\, {\rm d}t, \qquad \gamma = k h_{\rm d} \geq 0, \quad \zeta = \frac{|z|}{h_{\rm d}}, \quad t = \frac{z'}{h_{\rm d}}. \tag{4.54}$$

This formulation of $\hat{B}(k,z)$ is valid also for the previous case of zero-thickness (eq. 4.52), as a particular case with $g(t) = \delta(t)/h_{\rm d}$. We present the expressions of the functions $B(z)$, and so $g(t)$ in the integral above, for the exponential and the 'pseudo-isothermal' stratifications, and we derive the related analytical solutions for $\hat{B}(k,z)$. In particular, with this new approach, for the exponential case, we re-obtain the results known from the literature, while for the first time we offer the solution for the computation of the potential of the 'pseudo-isothermal' vertical distribution. Moreover, in the latter case, we derive the solution for a generic power-law n of the hyperbolic secant, where the most common used value of $n = 2$ (Spitzer 1942; see also Section 4.1.3) is obtained as a particular case with no effort.

The exponential stratification

An exponential vertical stratification (Freeman, 1970), perhaps the simplest modification of the razor-thin disc, is given by

$$B(z) = {\rm e}^{-|z|/h_{\rm d}}. \tag{4.55}$$

The solution of eq. (4.54), with $g(t) = {\rm e}^{-|t|}$, have already been studied, and published in the literature: we report here for completeness the solution in the current notation, reassuringly in agreement with e.g. Kuijken and Gilmore (1989); Cuddeford (1993). By inserting eq. (4.55) in eq. (4.54), the resulting integral can be split in three parts: between

$-\infty$ and 0, between 0 and ζ, and between ζ and ∞. The integration is elementary for the three parts, giving

$$\mathrm{e}^{-\gamma\zeta}\int_{-\infty}^{0}\mathrm{e}^{(\gamma+1)t}\,\mathrm{d}t=\frac{\mathrm{e}^{-\gamma\zeta}}{\gamma+1},\qquad \mathrm{e}^{\gamma\zeta}\int_{\zeta}^{\infty}\mathrm{e}^{-(\gamma+1)t}\,\mathrm{d}t=\frac{\mathrm{e}^{-\zeta}}{\gamma+1},\tag{4.56}$$

and

$$\mathrm{e}^{-\gamma\zeta}\int_{0}^{\zeta}\mathrm{e}^{(\gamma-1)t}\,\mathrm{d}t=\begin{cases}\dfrac{\mathrm{e}^{-\zeta}-\mathrm{e}^{-\gamma\zeta}}{\gamma-1}, & \gamma\neq 1,\\ \zeta\,\mathrm{e}^{-\zeta}, & \gamma=1.\end{cases}\tag{4.57}$$

Therefore, we obtain

$$\hat{B}(k,z)=h_{\mathrm{d}}\times\begin{cases}\dfrac{2\,(\gamma\mathrm{e}^{-\zeta}-\mathrm{e}^{-\gamma\zeta})}{\gamma^2-1}, & \gamma\neq 1,\\[2ex] \mathrm{e}^{-\zeta}(1+\zeta), & \gamma=1.\end{cases}\tag{4.58}$$

The 'pseudo-isothermal' sheet

The so-called 'pseudo-isothermal' sheet is defined by the *even* stratification

$$B(z)=\mathrm{sech}^n(z/h_{\mathrm{d}}),\qquad n>0,\tag{4.59}$$

where $\mathrm{sech}^n(t)=\cosh^{-n}(t)$, which naturally produces again an exponential density decline. Surprisingly, although studied in several theoretical works and widely used in applications, it is often stated in the literature the impossibility to solve analytically the integral of eq. (4.54) for this case (e.g. Casertano, 1983; Kuijken and Gilmore, 1989; Cuddeford, 1993). Thus a fast 1D numerical integration of the gravitational potential of a disc with a vertical stratification such as eq. (4.59) would not be allowed. We show in the following that the analytical solution of eq. (4.54) is in fact possible, even if not in terms of elementary functions, for generic positive values of n.

Therefore, in eq. (4.54), $g(t)=2^n\mathrm{e}^{nt}/(1+\mathrm{e}^{2t})^n$, and the integration can be performed as follows. We split the integral in two parts, between $-\infty$ and ζ, and between ζ and ∞; in each of the two integrals, we change the variable as $y=\mathrm{e}^{2t}$. The two integrals can now be recast in a very compact form, as functions of three parameters, so that they can be written as

$$\begin{aligned}\int_0^{\epsilon}\frac{y^{\beta}\,\mathrm{d}y}{(1+y)^{\alpha}}&=\mathrm{B}\left(\beta+1,\alpha-\beta-1;\frac{\epsilon}{1+\epsilon}\right),\qquad \alpha>0,\quad \beta>-1,\\ \int_{\epsilon}^{\infty}\frac{y^{\beta}\,\mathrm{d}y}{(1+y)^{\alpha}}&=\mathrm{B}\left(\alpha-\beta-1,\beta+1;\frac{1}{1+\epsilon}\right),\qquad \alpha>0,\quad \alpha-\beta>1,\end{aligned}\tag{4.60}$$

in terms of incomplete Beta functions, $\mathrm{B}(a, b; x)$, requiring $a > 0$ always, and $b > 0$ when $x = 1$ (see Appendix C). Then we obtain

$$\begin{aligned}\hat{B}(k, z) = h_{\mathrm{d}}\, 2^{n-1} \bigg[& \mathrm{e}^{-\gamma\zeta} \mathrm{B}\left(\frac{n+\gamma}{2}, \frac{n-\gamma}{2}; \frac{1}{1+\mathrm{e}^{-2\zeta}}\right) \\ & + \mathrm{e}^{\gamma\zeta} \mathrm{B}\left(\frac{n+\gamma}{2}, \frac{n-\gamma}{2}; \frac{\mathrm{e}^{-2\zeta}}{1+\mathrm{e}^{-2\zeta}}\right)\bigg].\end{aligned} \tag{4.61}$$

A few comments are in order about the last equation. First, we stress that we recast the argument x of the Beta functions in a suitable form, in order to avoid numerical evaluations of ratios between very large numbers. Second, the condition $a > 0$ is always verified, since n and γ are positive coefficients. On the contrary, the condition $b > 0$ for $x = 1$ apparently fails easily, in the sense that $(n - \gamma)/2$ becomes negative for $n < \gamma$, and we recall that $\gamma = k h_{\mathrm{d}}$ is integrated from 0 to ∞ in eq. (4.50). However, for both the arguments of the incomplete Beta functions of eq. (4.61), we can be sure that x is always smaller than 1, and in fact it is immediate to see that $0 < x < 1$, since $\zeta \geq 0$. After careful considerations, we then confirm that the conditions on the arguments a and b are always satisfied for the incomplete Beta functions used in eq. (4.61).

A further consideration is however in order, specifically for a numerical implementation. As happens for the homoeoidally expanded potential of eq. (4.41), the fact that the argument b of the incomplete Beta function can be negative (for some values of n and γ, as seen above), impedes in some cases the numerical implementation, as shown in Appendix C. Therefore, a relation between the incomplete Beta function and the Hypergeometric function is given (eq. C.3), allowing for an alternative formulation of eq. (4.61), such as

$$\begin{aligned}\hat{B}(k, z) = \frac{h_{\mathrm{d}}\, 2^{n}}{(n+\gamma)(1+\mathrm{e}^{-2\zeta})^{(n+\gamma)/2}} \bigg[& \mathrm{e}^{-\gamma\zeta} {}_2\mathrm{F}_1\left(\frac{\mathrm{n}+\gamma}{2}, \frac{2-\mathrm{n}+\gamma}{2}; \frac{2+\mathrm{n}+\gamma}{2}; \frac{1}{1+\mathrm{e}^{-2\zeta}}\right) \\ & + \mathrm{e}^{-n\zeta} {}_2\mathrm{F}_1\left(\frac{\mathrm{n}+\gamma}{2}, \frac{2-\mathrm{n}+\gamma}{2}; \frac{2+\mathrm{n}+\gamma}{2}; \frac{\mathrm{e}^{-2\zeta}}{1+\mathrm{e}^{-2\zeta}}\right)\bigg].\end{aligned} \tag{4.62}$$

4.4.3 Tests for factorised discs

We show now the application of the method presented to two density models commonly used for discs, already reported in Section 4.1.3: the double-exponential disc and the pseudo-isothermal exponential disc. Their density distribution, respectively eq. (4.21) and eq. (4.22), is of the factorised form of eq. (4.49), so that the potential can be evaluated from eqs. (4.50)–(4.51). The Hankel transform $\hat{A}(k)$ for the exponential radial part is given in eq. (D.2), while the solutions for $\hat{B}(k, z)$ for the vertical stratifications are given in eq. (4.58) for the exponential case, and in eq. (4.62) for the pseudo-isothermal sheet.

In Section 4.3, we verified the accuracy of the numerical integration based on elliptic integrals (eq. 4.23), which we recall is valid for any axisymmetric density distribution, so

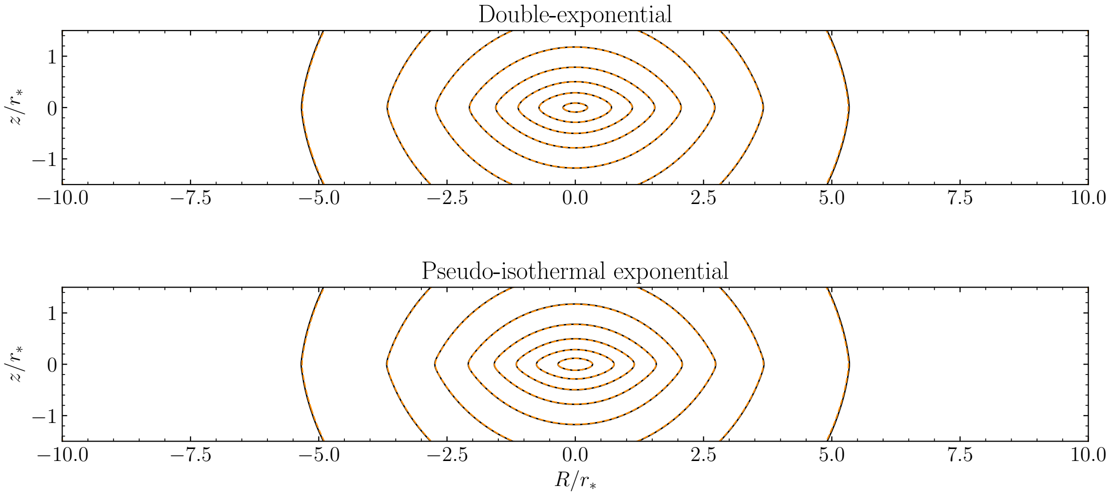

Figure 4.5: Isopotential contours on the meridional plane $\left(\tilde{R},\tilde{z}\right)$ for a double-exponential disc (top) and a pseudo-isothermal exponential disc (bottom). The numerical evaluation of the potentials in terms of complete elliptic integrals (solid black line) and of Bessel functions (dashed orange line) are compared, showing excellent agreement between the two methods. The two models have $\tilde{a} = 1$, $\tilde{b} = 0.1$, and for the second model we set the isothermal sheet, i.e. $n = 2$. The isopotential contours represent the dimensionless $\phi/\phi_{\rm n}$, with values spaced by 1 dex.

that we take it as reference here. Then, we test the accuracy of the numerical evaluation of the gravitational potential in terms of Bessel functions, for the two factorised discs above, by showing the comparison with the potential computed in terms of elliptic integrals. In Fig. 4.5, the isopotential contours on the meridional plane $\left(\tilde{R},\tilde{z}\right)$ are compared for two quite thin discs with arbitrary parameters ($\tilde{a} = 1$, $\tilde{b} = 0.1$, and $n = 2$ for the isothermal-sheet), where curves of $\tilde{\phi} = \phi/\phi_{\rm n}$ calculated via the elliptic integrals integration are solid black, and the curves obtained with the Bessel method are dashed orange: the agreement is excellent. We recall, as detailed in Appendix B, the outstanding gain in computational time allowed by the new method, making it the favourite choice when it is possible to apply it.

Looking at the shape of the isopotential curves, for this choice of the model parameters, the potentials produced by a double-exponential disc and by an isothermal exponential disc are very similar, slightly more flattened near the centre in the second case. Notice also that, for both the models, the potential is quite flattened in the inner regions, while it is almost spherical towards large radii.

4.5 Summary

We showed several density models which are suitable for the description of stellar and DM components in galaxies; in the next Chapters some of them are used to build specific galaxy models, and their properties are discussed in more details. A starting and crucial point of galaxy modelling is the evaluation of the gravitational potential associated to each density component involved in the system; we presented different methods to calculate the potential for axisymmetric systems in cylindrical coordinates, which we can summarise as follows, in agreement with Table 4.1:

- analytical potential (when available),
- elliptic integrals (always),
- Chandrasekhar formula (ellipsoids),
- homoeoidal expansion (ellipsoids),
- Bessel functions (factorised discs).

With respect to the 2D integration in terms of elliptic integrals, besides the immediate (exact or approximated) analytical expressions for the potentials, the 1D integrations based on the Chandrasekhar formula, or Bessel functions, allow to reduce the computational time required by the numerical computation of a potential component, from many hours to few minutes or even few seconds. We showed that these alternative methods are not only remarkably faster, but they are also equally accurate. After a safety check on the numerical solution of the Jeans equations, we investigated the reliability of homoeoidal approximations, for increasing flattening (in the limit allowed by the homoeoidal expansion technique). Since our tests have been performed on Jaffe models, and the results can depend on the density models, we only assert here that σ is reconstructed with high precision even for quite flat spheroids, while the discrepancy increases faster for $\sqrt{\Delta}$, when solving numerically the Jeans equations (with JASMINE2) for an homoeoidally-expanded density-potential pair or for the true ellipsoidal density with numerical potential. On the other side, we also confirm that, when exploiting analytical solutions of the Jeans equations obtained in homoeoidal expansion, neglecting second-order terms in the flattening does not produce a significant divergence. Finally, concerning the integral formula based on Bessel functions, we stress the benefit of our method: we propose a general formula which can be used for a variety of factorised discs, allowing to combine many possible radial profiles with at least two different vertical stratifications. Thanks to the efficiency of this method, it is not necessary to resort to the approximation of zero-thickness of the disc, neither to simple analytical but less realistic disc models (in the next Chapter, we will see, for example, the decomposition of thick exponential discs with a combination of MN discs). In particular, we offer a practical solution for the sech^n stratification, even if not in terms of elementary functions. We also showed that for $n = 2$, an isothermal exponential disc and a double-exponential disc, with same scale-length and scale-height, produce a very similar potential.

Chapter 5

Illustrative multicomponent models

In order to illustrate the features and potentialities of the modelling procedure, as presented so far and implemented in JASMINE2, we show in this Chapter four brief direct applications. Firstly, we describe in some detail the building of three multicomponent galaxy models; we focus on the resulting total structural and dynamical properties, and on the projected kinematical fields, discussing the contribution of each matter component. All the three models are made of two stellar distributions, to which a DM halo with a spherical NFW profile and a central supermassive BH are added. In the first model (called JJE, i.e. 'Jaffe-Jaffe Ellipsoidal') the *total* spherical stellar distribution and an ellipsoidal stellar component, both with a Jaffe density profile, are assigned; then the second stellar component is obtained *by difference*. This represents a special way to build multiple components, not by sum of assigned components, but by difference, as a particular application of the modelling procedure presented; the JJE model originates as a generalisation of JJe models in homoeoidal expansion of CMPZ21. The successive models are instead built by sum of assigned components. The second model (JHD, for 'Jaffe-Heavy Disc') consists of an ellipsoidal Jaffe stellar density distribution, that represents a light stellar halo, coupled with a massive MN stellar disc. In the third model (JLD, for 'Jaffe-Light Disc'), the ellipsoidal Jaffe component dominates, while a small MN inner disc counter-rotates in the central regions. These three models are intended to represent features observed in real galaxies, but they are not designed to reproduce specific objects. Finally, we illustrate the comparison between a double-exponential disc and its representation via the sum of three MN discs, as proposed by Smith et al. (2015), with the extension of their analysis to the projected kinematical fields.

Caravita C., Ciotti L. and Pellegrini S., 2021, MNRAS

5.1 The JJE models

JJE models are a natural generalisation of JJe (standing for 'Jaffe-Jaffe ellipsoidal') models presented in CMPZ21. As these latter describe quite well real elliptical galaxies, and several of their dynamical properties can be expressed in analytical form, through the homoeoidal expansion technique, they also represent an obvious test for JASMINE2 (see Section 4.3). JJE models consist in multicomponent models made of two stellar components defined *by difference*, a DM halo, and a central BH, allowing to test this way of modelling the stellar distributions, as a particular case of the sum rules illustrated in Chapter 2. We also extend the analysis of JJe models, by studying the dynamics and the stellar properties of the *difference* component. Moreover, as we will see, the difference component results slightly prolate, requiring special case in its treatment, and offering the chance to employ the generalised Satoh k-decomposition (Section 2.3.2). In the following, we see the main structural properties of this family of models, and then we analyse the features of a specific model, after the choice of specific parameters.

5.1.1 Building of JJE models by difference

To better appreciate the properties of JJE models, we first recall the main properties (and limitations) of JJe models. These are constructed by assigning a total density, that we call generically ρ, following the axisymmetric ellipsoidal generalisation of the Jaffe model (eq. 4.1), and another axisymmetric ellipsoidal Jaffe distribution, representing a stellar density component ρ_1, with different flattening, scale-length and total mass; in CMPZ21 the second density distribution is obtained by difference as $\rho_2 = \rho - \rho_1$, and interpreted as a DM halo; finally, a central BH is added to the system. The analytical conditions on ρ_1 to guarantee the positivity of ρ_2 are given, and then the Jeans equations for the stellar component ρ_1 are solved in analytical closed form, by using the homoeoidal expansion technique (reported in Section 4.2.2), truncated at the linear order in the flattenings q and q_1, of ρ and ρ_1, respectively (the expanded solution of the Jeans equations is that used for tests in Section 4.3). Albeit several properties of JJe models can be expressed in analytical form (making them useful in numerical simulations of gas flows in galaxies, see Chapter 6), few important shortcomings still affect them: i) the projected kinematical fields of ρ_1 can be obtained in analytical form only as asymptotic formulae at the center and at large radii; ii) the Jeans equations (and the projections) have not been studied for the difference component ρ_2. A numerical code like JASMINE2 is then the obvious tool to address the two points above.

Now we generalise the JJe models to JJE models: at variance with the former, in JJE models the total Jaffe density distribution is purely stellar, so that the two density components discussed above assume here the meaning of stellar distributions, and the galaxy turns out to include two stellar components. We model the total ρ_* with an ellipsoidal Jaffe profile, of total mass M_*, scale-length ξ, and flattening q, as given in eq. (4.1), and recast here with the inclusion of the weights and normalisation scales (see also

Table 3.1 for a summary of the model parameters):

$$\rho_*(R,z) = \frac{\rho_{\rm n}\xi}{q\, m^2(\xi+m)^2}, \qquad m^2 = \tilde{R}^2 + \frac{\tilde{z}^2}{q^2}. \tag{5.1}$$

We then consider another ellipsoidal Jaffe density profile, of total mass $M_{*1} = \mathcal{R}_1 M_*$, scale-length $r_{*1} = \xi_1 r_*$, and flattening q_1:

$$\rho_{*1}(R,z) = \frac{\rho_{\rm n}\mathcal{R}_1\xi_1}{q_1 m_1^2(\xi_1+m_1)^2}, \qquad m_1^2 = \tilde{R}^2 + \frac{\tilde{z}^2}{q_1^2}. \tag{5.2}$$

The second stellar component is then defined as

$$\rho_{*2}(R,z) = \rho_*(R,z) - \rho_{*1}(R,z), \tag{5.3}$$

with $M_{*2} = M_* - M_{*1} = (1-\mathcal{R}_1)\, M_* = \mathcal{R}_2\, M_*$, in agreement with eq. (3.10). Notice that ρ_{*2} is not an ellipsoid, unless $q_1 = q$, and even in this case ρ_{*2} is not a Jaffe ellipsoid, unless $\xi_1 = \xi$. As extensively discussed in CMPZ21, ρ_{*2} could be negative somewhere (and so unphysical) for some choices of $\mathcal{R}_1$, ξ_1 and q_1. Remarkably, the conditions required to assure $\rho_{*2} \geq 0$ can be expressed as analytical (and simple) inequalities: due to the different roles of the density components in our interpretation and in the original JJe models, we recast the positivity condition in Appendix E in agreement with our notation. In particular, in CMPZ21 the normalisation scales, r_* and M_*, represent the scale-length and the total mass, respectively, of the stellar density *component*, while here they represent the scale-length and the total mass of a *total* stellar distribution (making necessary to rewrite the proof in Appendix). In Chapter 6, we use again JJe models, with the original meaning of the density components of CMPZ21. We stress that for these illustrative models (JJE, JHD, JLD) we use actually the homoeoidally expanded density-potential pairs of the Jaffe models (eqs. 4.42–4.43), for which we solve the Jeans equations numerically with JASMINE2 (solutions that we call 'hom-num' in the tests of Section 4.3).

The total stellar distribution ρ_* is embedded in a NFW DM halo (spherically symmetric for simplicity), of mass $M_{\rm h}(r_{\rm t}) = \mathcal{R}_{\rm h} M_*$ enclosed within a truncation radius $r_{\rm t}$, scale-length $r_{\rm h} = \xi_{\rm h} r_*$, and concentration $c \equiv r_{\rm t}/r_{\rm h}$. Again, we recast eqs. (4.3) and (4.4) with the inclusion of the weights and normalisation scales, so that

$$\rho_{\rm h}(r) = \frac{\rho_{\rm n}\mathcal{R}_{\rm h}}{s(\xi_{\rm h}+s)^2 f(c)}, \qquad \phi_{\rm h}(r) = -\frac{\phi_{\rm n}\mathcal{R}_{\rm h}}{s f(c)} \ln\left(\frac{\xi_{\rm h}+s}{s}\right), \tag{5.4}$$

where $s = r/r_*$, and $f(c) = \ln(1+c) - c/(1+c)$. We complete the model with a central BH of mass $M_{\rm BH} = \mathcal{R}_{\rm BH} M_*$.

Summarising, JJE models are determined, besides the total stellar mass and scale-length, M_* and r_*, by the two parameters ξ and q for ρ_*, the five parameters q_1, ξ_1, $\mathcal{R}_1$, Υ_{*1}, k_1 for ρ_{*1}, the two parameters Υ_{*2}, k_2 for ρ_{*2}, the three DM parameters $\xi_{\rm h}$, c, $\mathcal{R}_{\rm h}$, and the BH mass weight $\mathcal{R}_{\rm BH}$ (see Table 5.1 for a specific JJE model). We anticipate that a further generalisation of JJE models can be found in 6, with the addition of a second DM component given by a shallow and very extended quasi-isothermal halo, as useful in simulations of gas flows in galaxies residing in groups or clusters.

Model	ρ_{*1}	ρ_{*2}
JJE	Jaffe	$\rho_*(\xi=1, q=1) - \rho_{*1}$
	$\xi_1 = 0.1$	—
	$q_1 = 0.8$	—
	$\mathcal{R}_1 = 0.04$	$\mathcal{R}_2 = 0.96$
	$\Upsilon_{*1} = 2$	$\Upsilon_{*2} = 6$
	$k_1 = 0.5$	$k_2 = 0.2$
JHD	Jaffe	MN
	$\xi_1 = 1$	$\tilde{b} = 0.1$
	$q_1 = 0.8$	$q_2 = 10$
	$\mathcal{R}_1 = 0.3$	$\mathcal{R}_2 = 0.7$
	$\Upsilon_{*1} = 6$	$\Upsilon_{*2} = 2$
	$k_1 = 0.5$	$k_2 = 0.8$
JLD	Jaffe	MN
	$\xi_1 = 1$	$\tilde{b} = 0.01$
	$q_1 = 0.8$	$q_2 = 10$
	$\mathcal{R}_1 = 0.96$	$\mathcal{R}_2 = 0.04$
	$\Upsilon_{*1} = 6$	$\Upsilon_{*2} = 2$
	$k_1 = 0.5$	$k_2(R, z)$

Table 5.1: The parameters for the stellar components of the illustrative JJE, JHD and JLD models (Sections 5.1 and 5.2). In the JJE model, the component ρ_{*2} is obtained as *difference* between a total spherical ($q = 1$) Jaffe profile ρ_*, with scale-length $\xi = 1$, and a small and light Jaffe ellipsoidal component ρ_{*1} (similarly to JJe models in CMPZ21). The standard Satoh k-decomposition in eq. (2.25) for ρ_{*1}, and the generalised k-decomposition in equation (2.27) for ρ_{*2}, are adopted. In the JHD model, an ellipsoidal Jaffe distribution is coupled to a massive and quite flat ($q_2 = \tilde{a}/\tilde{b} = 10$) MN disc; in both components a generalised k-decomposition is adopted. In the JLD model, the ellipsoidal Jaffe component has the same flattening and size as in the JHD model, but the disc is significantly smaller, and counter-rotates in the inner regions, with the position-dependent Satoh parameter in eq. (5.8), while a constant Satoh parameter is applied to the Jaffe component. In all models, the DM halo has a spherical NFW profile with $\xi_{\rm h} = 2.6$, $c = 10$, $\mathcal{R}_{\rm h} = 20$, and the BH is defined by $\mathcal{R}_{\rm BH} = 0.002$. Moreover, in all models the homoeoidally expanded density-potential pairs are used for the Jaffe distributions (after many checks on their reliability, as shown in Section 4.3). Finally, for details on the meaning and the role of the model parameters in Table, we refer to Section 3.2, and in particular Figure 3.1 and Table 3.1.

5.1.2 Results for a JJE model

We move now to illustrate the main properties of a specific JJE model (see Table 5.1). The total stellar distribution ρ_* has a spherical Jaffe profile obtained from eq. (5.1) with $\xi = 1$ and $q = 1$; this quite artificial case allows us to discuss some subtleties that can occur to the kinematical decomposition in multicomponent systems. The stellar component ρ_{*1} is obtained from eq. (5.2) with $\xi_1 = 0.1$, $q_1 = 0.8$, $\mathcal{R}_1$ is 0.04, and $\Upsilon_{*1} = 2$, i.e. it is a quite small ellipsoidal distribution at the center of the galaxy; note that, from eq. (E.15), the maximum possible value of $\mathcal{R}_1$ to assure a nowhere negative

ρ_{*2} is 0.08. The component ρ_{*2} accounts for the remaining 96% of the total stellar mass of the galaxy, and $\Upsilon_{*2} = 6$, so that ρ_* could represent an elliptical galaxy with a central and younger[1] stellar system. We add the spherical NFW DM halo, given by eq. (5.4), with $\xi_{\rm h} = 2.6$, $c = 10$, and $\mathcal{R}_{\rm h} = 20$, so that the DM mass inside r_* is ≈ 0.45 of the total mass[2]. Finally, in agreement with BH-galaxy scaling relations (see e.g. Kormendy and Ho, 2013), the mass of the central BH is fixed to $\mathcal{R}_{\rm BH} = 0.002$.

In the three top panels of Fig. 5.1, we show the scaled (dimensionless) density distribution of the components $\tilde{\rho}_{*1}$ and $\tilde{\rho}_{*2}$, and of the total stellar density $\tilde{\rho}_* = \rho_*/\rho_{\rm n}$ (from definitions of eq. 3.11). Being this last spherical, and $\tilde{\rho}_{*1}$ oblate, $\tilde{\rho}_{*2}$ in its central regions is slightly prolate, and this affects its kinematical fields, as we discuss below and anticipated in Section 2.3. Additional information on the model structure is provided in the first column of Fig. 5.2: the top panel shows the radial profiles in the equatorial plane of $\mathcal{R}_1\tilde{\rho}_{*1}$, $\mathcal{R}_2\tilde{\rho}_{*2}$, $\tilde{\rho}_*$, and $\mathcal{R}_{\rm h}\tilde{\rho}_{\rm h}$, i.e. the density components normalised to $\rho_{\rm n}$ (dimensionless density components, weighted for the respective mass ratios). The total ρ_* is almost coincident with ρ_{*2}, except for the central regions, where ρ_{*1} and ρ_{*2} are comparable. The DM density $\rho_{\rm h}$ overcomes ρ_* outside $\approx 0.5\, r_*$. The bottom panel shows the radial profiles in the equatorial plane of the contributions to the circular velocity due to the various mass components (from eq. 3.4): the BH contribution is dominant in the inner regions, the DM in the outer regions, while at intermediate distances from the centre the resulting circular velocity is quite flat. Notice that the radial scale is logarithmic, to appreciate the rotation curve produced by all the matter components, even if the flat region of the curve would have been more emphasised by a linear scale.

Similar trends can be seen in the radial profiles of the velocity fields in the equatorial plane of Fig. 5.3, where, in the first column from top to bottom, we show the rotational velocity, the vertical velocity dispersion, and the azimuthal velocity dispersion, of ρ_{*1} and ρ_{*2}, and the total mass-weighted and luminosity-weighted fields (see eqs. 2.14–2.18). Note that in the three panels the vertical scale is the same, and the resulting system appears to have a significantly low rotational velocity with respect to the velocity dispersion in all the directions, but producing a regular pattern of rotation (as we will see especially in Fig. 5.4). This JJE model offers the opportunity to apply the generalised k-decomposition of eq. (2.27): the field Δ_2, associated to the slightly prolate ρ_{*2}, is negative in the central regions, thus, as discussed in Section 2.3, we verify that $\overline{{\rm v}_{\varphi 2}^2}$ is nowhere negative, and then we adopt the generalised decomposition, with a quite small $k_2 = 0.2$. The field Δ_1 instead is everywhere positive, as expected, and so we adopt the standard Satoh formula of eq. (2.25) with $k_1 = 0.5$. In the velocity profiles, the effect of the central BH is clearly visible (thanks to the logarithmic radial scale); for

---

[1] From Evolutionary Population Synthesis models (e.g. Maraston, 2005), the mass-to-light ratio of a simple stellar population is a function of its age, chemical composition and initial mass function. Since younger stars are more brighter with respect to their mass, while older stars are massive but less luminous, a younger stellar population produces in general a smaller mass-to-light ratio.

[2] We recall that $R_{\rm e} \simeq 0.75\, r_*$ for a spherical Jaffe model with constant mass-to-light ratio, from Section 4.1.1. In fact, here the total stellar distribution has a spatially-dependent mass-to-light ratio, since the two stellar components have different values of Υ_{*1} and Υ_{*2}, so the approximation is not valid, but still gives an order of comparison.

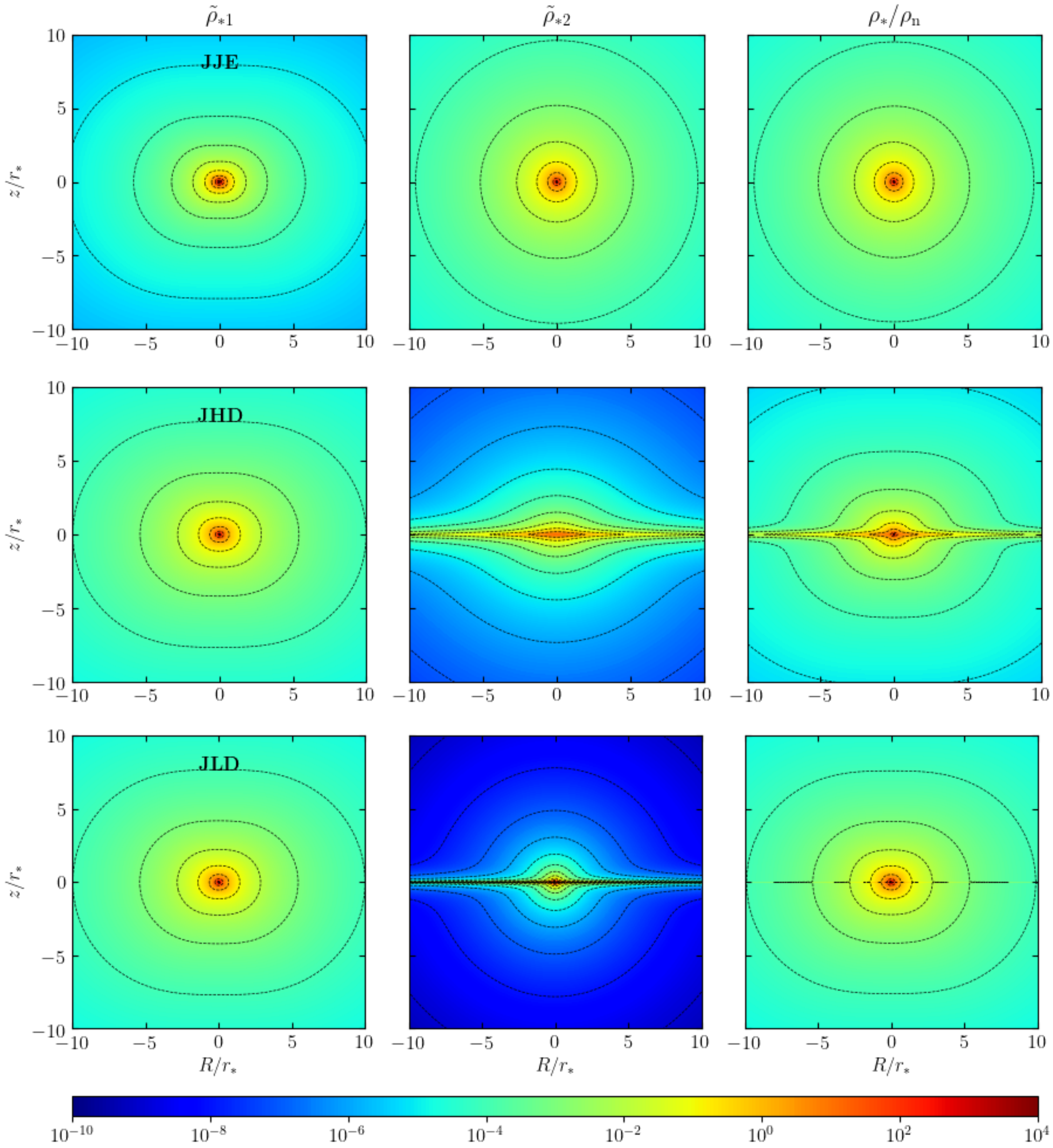

Figure 5.1: The scaled stellar distributions $\tilde{\rho}_{*1}$, $\tilde{\rho}_{*2}$, and the dimensionless total stellar distribution $\tilde{\rho}_* = \rho_*/\rho_\mathrm{n}$, of the three models of Table 5.1. The dotted contours show the isodensities, with values spaced by 1 dex.

example, the velocity dispersion profile of a Jaffe model with $\mathcal{R}_\mathrm{BH} = 0$ would be nearly constant in the central regions. Notice also how the velocity profiles, outside $\approx r_*$, are almost coincident with the profiles of the more massive component ρ_{*2}, in both the mass-weighted and luminosity-weighted cases: this is not surprising, because in these regions

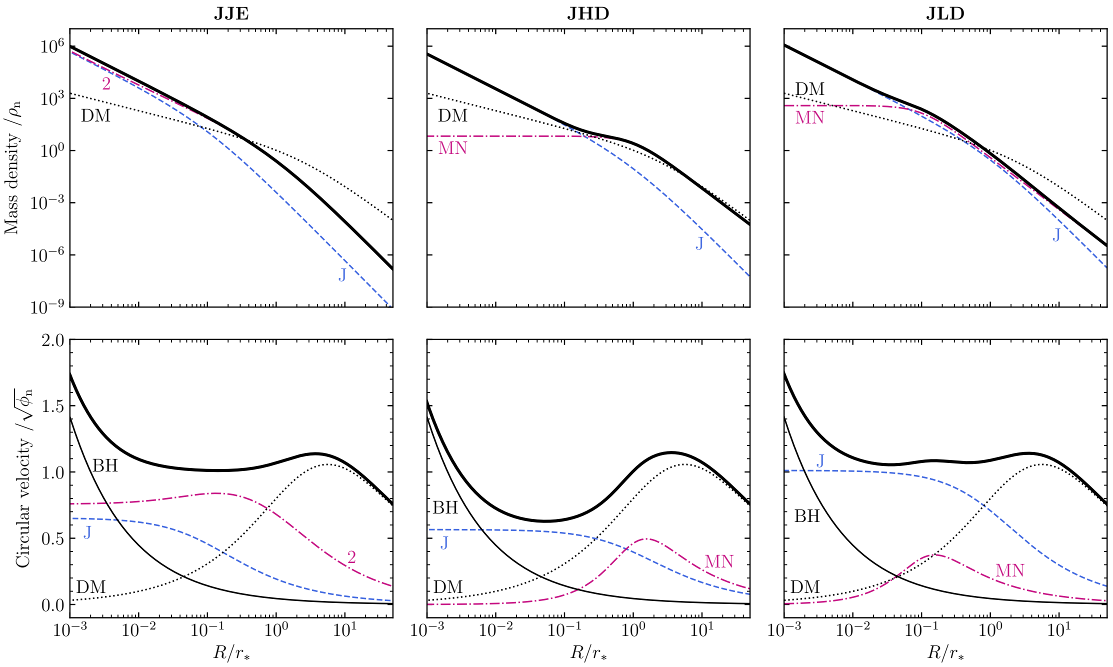

Figure 5.2: Radial profiles in the equatorial plane ($\tilde{z} = 0$) of the mass densities $\mathcal{R}_1\tilde{\rho}_{*1}$ (dashed blue), $\mathcal{R}_2\tilde{\rho}_{*2}$ (dotted-dashed magenta), $\tilde{\rho}_*$ (heavy solid), and $\mathcal{R}_h\tilde{\rho}_h$ (dotted), normalised to ρ_n (top row), for the three models of Table 5.1. In the bottom row, we show the corresponding contributions to the total circular velocity (heavy solid) in the equatorial plane of the mass components, with the additional contribution of the central BH (solid), all normalised to $\sqrt{\phi_n}$.

ρ_* nearly coincides with ρ_{*2} (see Figs. 5.1 and 5.2). The situation is different in the inner regions, where ρ_{*1} and ρ_{*2} are comparable: here the total velocities have intermediate values, with the luminosity-weighted profiles closer to the profiles of ρ_{*1} because of the smaller mass-to-light ratio.

As an illustration of the projection procedure, in the first row of Fig. 5.4, we show the EO projected luminosity-weighted fields $v_{\mathrm{los}\mathscr{L}}$ and $\sigma_{\mathrm{los}\mathscr{L}}$, with the superimposed dotted contours representing the galaxy isophotes of the surface brightness I_* (see Section 2.4). The model shows a clear morphology of regular rotation (see the classification of ETGs mentioned in Chapter 1; Krajnović et al. 2011; Cappellari 2016), with low rotation, as apparent from the colorbar values, where $v_{\mathrm{los}\mathscr{L}}$ is everywhere lower than $\sigma_{\mathrm{los}\mathscr{L}}$. A curious feature is the slightly vertically elongated shape of $\sigma_{\mathrm{los}\mathscr{L}}$: this is *not* due to the prolate shape of ρ_{*2} in the central regions, but it is an effect of the generalised k-decomposition, coupled with the fact that Δ_2 is almost null in the external regions, and so here $v_{\varphi 2} \sim k_2\sigma_2$, as introduced in Section 2.3.2. For example, an increase in k_2 would lead to an increase of the rotation in the external regions, with correspondent decrease of $\sigma_{\mathrm{los}\mathscr{L}}$, and with the net result of a more elongation of $\sigma_{\mathrm{los}\mathscr{L}}$ in the central regions.

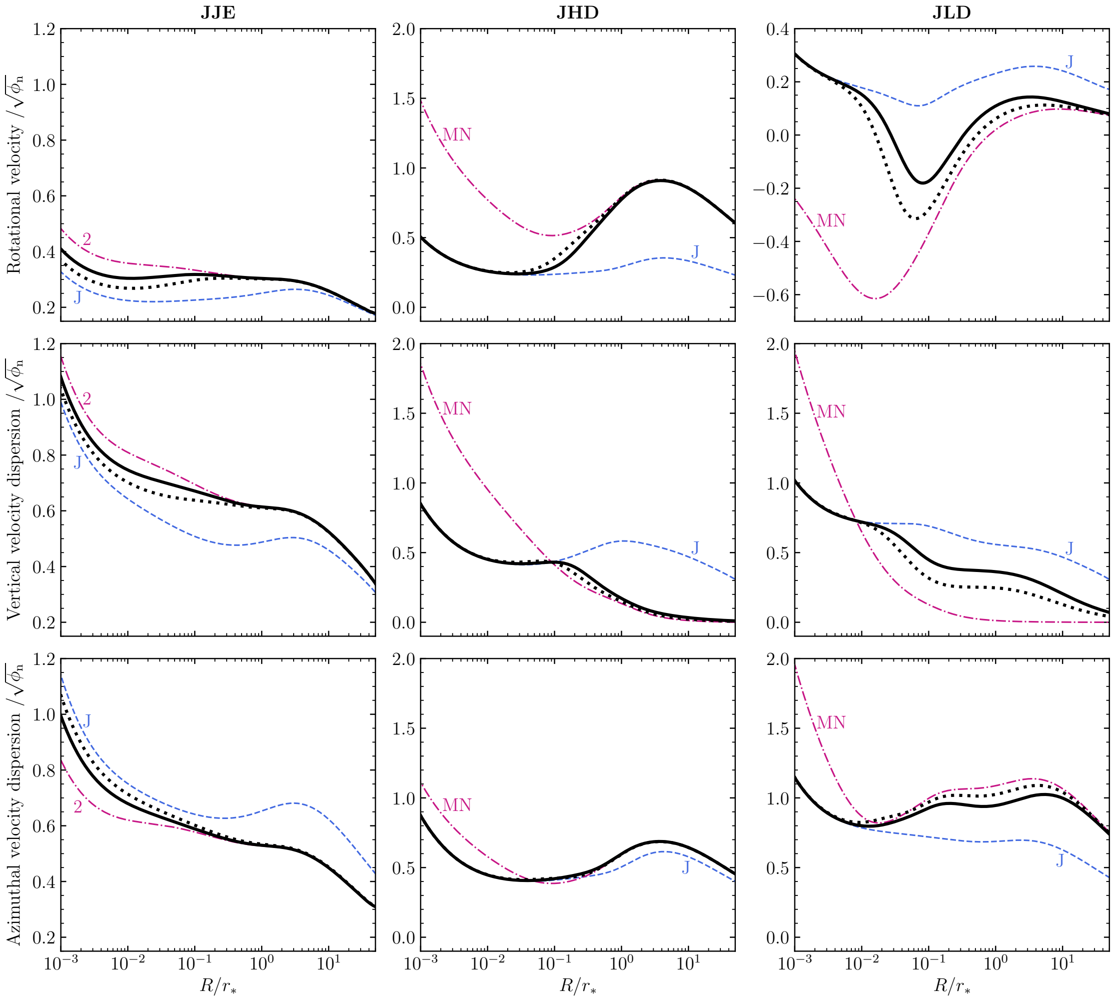

Figure 5.3: Radial profiles in the equatorial plane ($\tilde{z} = 0$) of the rotational velocities (top row), vertical velocity dispersions (middle row), and azimuthal velocity dispersions (bottom row), normalised to $\sqrt{\phi_n}$, for the three models of Table 5.1. Each panel shows the total mass-weighted (heavy solid) and luminosity-weighted (heavy dotted) fields, together with the corresponding fields of ρ_{*1} (dashed blue) and ρ_{*2} (dotted-dashed magenta). Notice the different values on the vertical scales of the first column (JJE model) and of the top right panel showing the counter-rotation (JLD model).

5.2 Ellipsoidal models with an embedded stellar disc

We consider two other galaxy models, made of two stellar components, a DM halo, and a central BH. In particular, we build the case (JHD) of a dominant stellar disc, embedded in an ellipsoidal stellar component, that can be interpreted as the stellar halo of a disc galaxy, and the case (JLD) of a small stellar disc, counter-rotating in the inner regions, at the center of a dominant stellar spheroid, as sometimes observed in real ETGs (e.g. Morelli et al. 2004; Krajnović et al. 2015; Mitzkus et al. 2017).

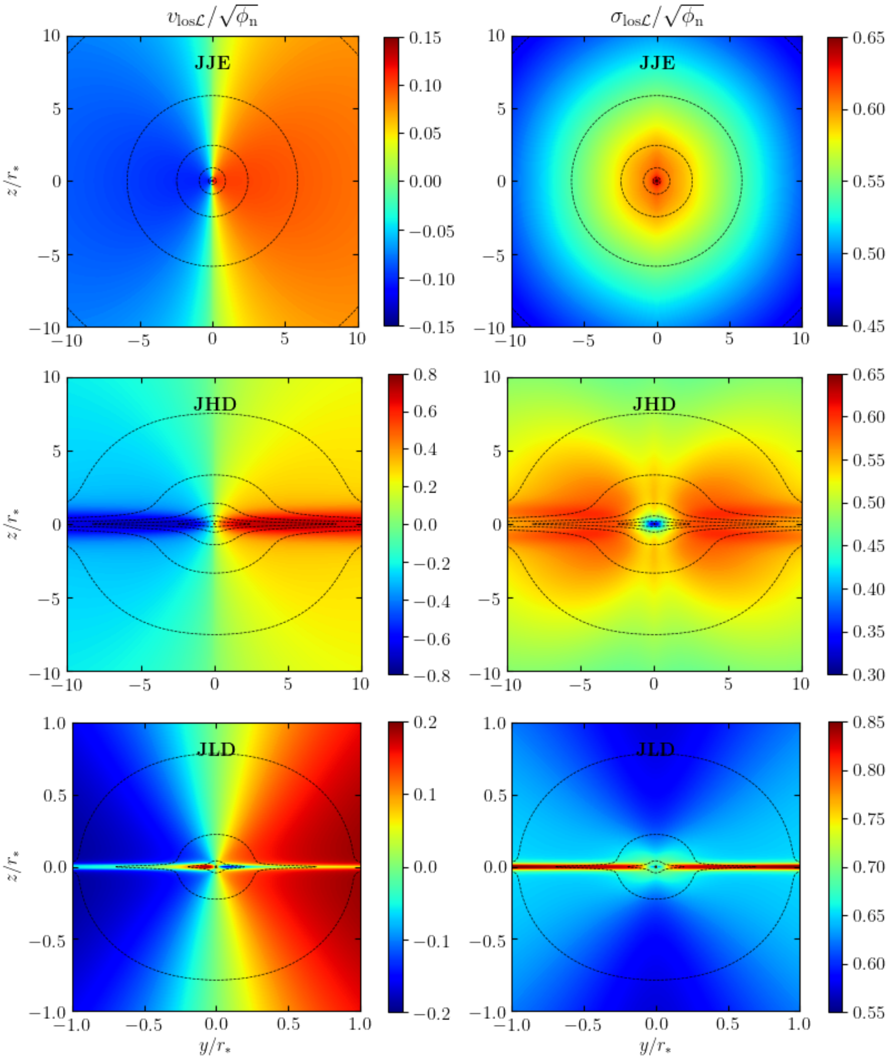

Figure 5.4: Edge-on projected luminosity-weighted rotational velocity $v_{\mathrm{los}\mathscr{L}}$ (left), and velocity dispersion $\sigma_{\mathrm{los}\mathscr{L}}$ (right), normalised to $\sqrt{\phi_{\mathrm{n}}}$, for the three models of Table 5.1. Notice the different ranges of values on the colorbars. For the JLD model, the region shown is limited to r_* to appreciate the central features, in particular the inner counter-rotating disc. The dotted contours show the galaxy isophotes with values spaced by 1 dex.

JHD and JLD models consist of a stellar profile ρ_{*1} given again by the ellipsoidal Jaffe model of eq. (5.2), coupled with a stellar MN disc ρ_{*2}, of total mass $M_{*2} = \mathcal{R}_2 M_*$, and scale-lengths $a = \tilde{a} r_*$, $b = \tilde{b} r_*$:

$$\rho_{*2}(R,z) = \rho_{\mathrm{n}} \mathcal{R}_2 \tilde{b}^2 \frac{\tilde{a}\tilde{R}^2 + (\zeta + 2\sqrt{\tilde{z}^2+\tilde{b}^2})\zeta^2}{(\tilde{R}^2+\zeta^2)^{5/2}(\tilde{z}^2+\tilde{b}^2)^{3/2}}, \tag{5.5}$$

$$\phi_{*2}(R,z) = -\frac{\phi_{\rm n}\mathcal{R}_2}{\sqrt{\tilde{R}^2+\zeta^2}}, \quad \zeta = \tilde{a} + \sqrt{\tilde{z}^2+\tilde{b}^2}, \tag{5.6}$$

where, in analogy with the previous Section, we recast here eqs. (4.15) and (4.16), with the inclusion of the weights and normalisation scales, and in particular $\mathcal{R}_2 = 1 - \mathcal{R}_1$ from eq. (3.10). We recall that for $\tilde{a} = 0$ the MN disc reduces to the Plummer (1911) sphere, and for $\tilde{b} = 0$ to the razor-thin Kuzmin (1956) disc; in the following, we indicate the disc flattening parameter with $q_2 = \tilde{a}/\tilde{b}$. As in JJE models, we add the spherical NFW halo in eq. (5.4), and a central BH. Overall, JHD and JLD models differ from the JJE model only for the second stellar component ρ_{*2}, and consequently for the total ρ_*; moreover, ρ_* is now obtained by the sum of the stellar components, so that

$$\rho_*(R,z) = \rho_{*1}(R,z) + \rho_{*2}(R,z), \tag{5.7}$$

while in JJE models ρ_{*2} is obtained by difference of assigned ρ_* and ρ_{*1} from eq. (5.3). The resulting multicomponent models are completely determined once the values of ξ_1, q_1, $\mathcal{R}_1$, Υ_{*1}, k_1 for ρ_{*1}, $\tilde{b}$, q_2, Υ_{*2}, k_2 for ρ_{*2}, $\xi_{\rm h}$, c, $\mathcal{R}_{\rm h}$ for $\rho_{\rm h}$, and $\mathcal{R}_{\rm BH}$ for the BH, are assigned, in addition to the total stellar mass M_* and the scale length r_* (see Table 5.1). The parameters of the DM halo and of the central BH are the same as in the JJE model.

5.2.1 Results for the JHD model

In the 'Jaffe - Heavy Disc' JHD model (see Table 5.1), the ellipsoidal Jaffe stellar halo ρ_{*1} is characterised by a scale-length $\xi_1 = 1$, a flattening $q_1 = 0.8$, a stellar mass fraction of 30% of the total stellar mass (i.e. $\mathcal{R}_1 = 0.3$), and a mass-to-light ratio $\Upsilon_{*1} = 6$. The dominant and younger MN disc ρ_{*2} ($\mathcal{R}_2 = 0.7$) is quite flat ($q_2 = 10$), with $\tilde{b} = 0.1$, and a lower $\Upsilon_{*2} = 2$.

In the central row of Fig. 5.1, the dimensionless density distributions $\tilde{\rho}_{*1}$, $\tilde{\rho}_{*2}$, and $\tilde{\rho}_*$, are shown. The resulting isodensity contours of ρ_* could be classified as *discy* near the equatorial plane, and as *boxy* at large distance from the plane. The radial profiles of the density distributions (including the DM), in the equatorial plane, are shown in Fig. 5.2. It is apparent how, inside $\approx 0.1\,r_*$ the Jaffe halo dominates, around r_* the MN disc dominates, and $\rho_{\rm h}$ overcomes the total ρ_* outside $\approx 10\,r_*$. Note that, even if $\mathcal{R}_1 < \mathcal{R}_2$, ρ_{*1} dominates the total density in the central regions, due to the cuspy profile of the Jaffe density compared with the flat core of the MN density. The density decomposition reflects on the circular velocity profiles in the bottom panel of the same Figure: the total $v_{\rm c}$ at small radii is totally dominated by the BH, and at large radii by the DM halo; while the *bump* around $3\,r_*$ is due to the MN and the DM potentials.

The radial profiles in the equatorial plane of the velocity fields, obtained from the Jeans equations, coupled with suitable kinematical decompositions, are shown in the middle column of Fig. 5.3, where from top to bottom the total mass- and luminosity-weighted rotational velocity, vertical velocity dispersion, and azimuthal velocity dispersion, are plotted together with the corresponding quantities for each stellar component separately. For the adopted values of the parameters in Table 5.1, Δ_1 turns out to be negative in a quite central region, while $\Delta_1 + \sigma_1^2$ is everywhere positive; we decide to apply the generalised k-decomposition of eq. (2.27) to both stellar components, with $k_1 = 0.5$ and $k_2 = 0.8$. The total velocity profiles, in the central regions, are completely determined by the Jaffe profile, because here $\rho_{*1} > \rho_{*2}$, compensating also for the higher Υ_{*1}; in the external regions, instead, the total profiles are dominated by the MN disc. Furthermore, v_φ stays well below v_c both in the inner and outer regions, as for the JJE model as well (see v_c in Fig. 5.2), as expected and as a clear manifestation of *asymmetric drift* in the equatorial plane (e.g. B&T08). Note that σ_2, associated with a flat density profile at the centre, is much higher than σ_1, associated with $\rho_{*1} \sim R^{-2}$ in the inner regions, as can be expected from the integration of the vertical Jeans equation for a power law density distribution in the gravitational field of a point-mass (i.e. the BH). In addition, Δ_2 of the MN model with the central BH vanishes at the centre (as known analytically, see e.g. Ciotti, 2021), thus in the generalised k-decomposition $v_{\varphi 2} \sim k_2 \sigma_2$ (at variance with what would happen in the standard Satoh decomposition, i.e. $v_{\varphi 2} = k_2 \sqrt{\Delta_2}$).

In the second row of Fig. 5.4, the luminosity-weighted projected fields $v_{\mathrm{los}\mathscr{L}}$ and $\sigma_{\mathrm{los}\mathscr{L}}$ are shown, and the high rotation of the disc is clearly visible, with an overall regular rotation pattern. The drop of $v_{\mathrm{los}\mathscr{L}}$ inside r_* is due to a drop of the internal rotational velocity (Fig. 5.3). Also $\sigma_{\mathrm{los}\mathscr{L}}$ shows the highest values near the equatorial plane, with a nearly toroidal distribution around the centre, and a drop inside r_*.

5.2.2 Results for the JLD model

At variance with the JHD model, in the 'Jaffe - Light Disc' JLD model (see Table 5.1), the ellipsoidal Jaffe distribution ρ_{*1} accounts for almost the whole stellar mass of the galaxy ($\mathcal{R}_1 = 0.96$), while its scale-length ($\xi_1 = 1$), flattening ($q_1 = 0.8$), and mass-to-light ratio ($\Upsilon_{*1} = 6$) are unchanged. The component ρ_{*2} is a small and young MN disc, with $\tilde{b} = 0.01$ and $\mathcal{R}_2 = 0.04$, while $q_2 = 10$ and $\Upsilon_{*2} = 2$ are the same of the JHD model.

The scaled density distributions, and the resulting total stellar density, are shown in the three bottom panels of Fig. 5.1: $\tilde{\rho}_{*1}$ is (structurally) identical to that of the JHD model, while $\tilde{\rho}_{*2}$ is much more concentrated, so that the total stellar density is distributed in an extended halo with a very small disc. Indeed, the disc is almost invisible in the last panel, and it would be apparent only with a zoom in, as in Fig. 5.4. The last column of Fig. 5.2 shows the radial profiles in the equatorial plane of the density components, with their mass weights, and the resulting decomposition of the galaxy circular velocity profile. Notice that the central values of ρ_{*2} are higher than those in the JHD model, due to its smaller size, compensating for the reduced mass. In the circular velocity plot, this reflects into a larger contribution from the Jaffe component, and a smaller and inner *bump* of the MN component. As a result, v_c is almost flat between $10^{-2}\, r_*$ and $10\, r_*$.

In the last column of Fig. 5.3, the radial profiles of the velocity fields in the equatorial plane are shown. As in the previous models, of course, the total luminosity-weighted profiles, when distinguished from the mass-weighted ones, are always closer to the profiles of the component with the lower mass-to-light ratio. For the JLD model, both Δ_1 and Δ_2 are everywhere positive, so we apply the standard Satoh decomposition. The stellar halo is modeled with a low rotation, given by $k_1 = 0.5$, while the circumnuclear stellar disc as a faster and counter-rotating light disc. In order to have counter-rotation limited to a central region, we adopt a position-dependent Satoh parameter, defined as follows:

$$k_2(R, z) = k_0 + (k_\infty - k_0)\frac{s}{s + 0.1}\,, \qquad s = \sqrt{\tilde{R}^2 + \tilde{z}^2} \tag{5.8}$$

(also used in Chapter 6; see also Negri, Ciotti and Pellegrini 2014 for an alternative parameterisation), with $k_0 = -0.8$, $k_\infty = 0.1$, where the negative sign of k_0 assures the counter-rotation of the disc, as can be seen in the top right panel of Fig. 5.3, and we will discuss below for Fig. 5.4. At very small radii (inside $10^{-2}\,r_*$), the total rotational velocity is again positive, because the density is dominated by the Jaffe component. We stress that the module of $v_{\varphi 2}$ decreases towards the centre, at variance with the JHD model, because now $v_{\varphi 2} = k_2\Delta_2$, and $\Delta_2 \to 0$, as explained in the previous Section. The central total vertical velocity dispersion is higher than that of the JHD model, even if the Jaffe component is structurally identical, because of the higher $\mathcal{R}_1$ and of the more concentrated MN disc.

In the last row of Fig. 5.4, the los luminosity-weighted velocities show clearly the effect of the inner thin disc, where the region shown is limited to r_* to appreciate the central features: in the $v_{\mathrm{los}\mathscr{L}}$ distribution we have counter-rotation at small radii (but not in the very centre). In particular, the inner regions of the disc (excluded the very central radii, as already seen for Fig. 5.3) have opposite rotation with respect to the surrounding stellar halo, and also to the outer regions of the disc itself: from an observational point of view, they would appear as two counter-rotating disc components, as sometimes observed in slow rotator ETGs (e.g. Morelli et al. 2004; Krajnović et al. 2015; Mitzkus et al. 2017; see also Chapter 1, and Krajnović et al. 2011; Cappellari 2016). The disc is also responsible for the highest values of the $\sigma_{\mathrm{los}\mathscr{L}}$ in the equatorial plane, and the extended surrounding toroidal distribution is also present, in analogy with the JHD model.

5.3 Exponential discs and multi-MN decompositions

Exponential discs are the common choice for modelling the stellar disc of disc galaxies. Their gravitational potential can be constructed numerically by using the general formula based on complete elliptic integrals or by using Bessel functions, as deeply discussed in Section 4.2. The latter approach is particularly useful in case of factorised densities, such as

$$\rho_*(R, z) = \frac{\rho_{\mathrm{n}}\mathrm{e}^{-\tilde{R}/\alpha}}{\alpha^2} V(\tilde{z}/\beta), \tag{5.9}$$

where $\alpha = R_{\mathrm{d}}/r_*$ and $\beta = h_{\mathrm{d}}/r_*$ are respectively the scale-length and scale-height of the disc, and the function V describes its vertical distribution. Different expressions of V recover the three exponential discs of Section 4.1.3: the the razor-thin exponential disc of eq. (4.20), the double-exponential disc of eq. (4.21), and the pseudo-isothermal exponential disc of eq. (4.22). Unfortunately, the gravitational potential of these discs cannot be obtained in a pure analytical expression; however, due to their relevance in the construction of galaxy models, alternative models with analytical potential have been proposed in the literature. In particular, the possibility to use multicomponent MN models to reproduce exponential discs, over some finite radial range, has been explored for example by Smith et al. (2015) and Rojas-Niño et al. (2016) (see also Flynn et al., 1996; Ciotti and Pellegrini, 1996). Such alternatives optimise the fit of the density profile, and produce a good agreement with the rotation curve of the exponential disc. Obviously, the superposition of MN discs with their power-law radial decline at large radii (see eq. 4.15) cannot reproduce the exponential decline of eq. (5.9). This forces to include at least one MN density component with negative mass (or negative scale-length), that can lead to a disc density distribution somewhere negative. The use of a multicomponent MN representation of an exponential disc is motivated by the advantage of avoiding a time-consuming numerical computation of its gravitational potential. However, as shown in Section 4.2, it is possible to obtain the potential of factorised exponential discs in eq. (5.9) also with a very fast 1D integration in terms of Bessel functions (a method we implemented in JASMINE2).

As a natural application of our procedure, we extend the work carried out by Smith et al. (2015), by constructing the solutions of the Jeans equations for the double-exponential disc and for its everywhere positive density representation in terms of three MN discs (hereafter 3MN). This 3MN decomposition is an ideal application of our multicomponent modelling procedure, also because one MN component has negative mass, which gives the opportunity to illustrate how the scaling scheme presented in Chapter 3 works also with negative values of the mass ratios $\mathcal{R}_i$.

5.3.1 A double-exponential disc and its 3MN fit

We consider the single-component double-exponential model, recast from eq. (4.21), so that

$$\rho_*(R,z) = \rho_\mathrm{n}\mathcal{R}_\mathrm{d}\frac{\mathrm{e}^{-\tilde{R}/\alpha-|\tilde{z}|/\beta}}{\alpha^2\beta}, \tag{5.10}$$

in analogy with eq. (5.9), with mass $\mathcal{R}_\mathrm{d} = M_\mathrm{d}/M_* = 1$, scale-length $\alpha = R_\mathrm{d}/r_* = 1$, and scale-height $\beta = h_\mathrm{d}/r_* = 0.1$. For this density distribution, we build the everywhere positive 3MN fit, following Section 2.2 in Smith et al. (2015). Accordingly, the three MN components are given as in eqs. (5.5) and (5.6), with a same scale-height $\tilde{b}$, and different $\mathcal{R}_i$ and scale-length $\tilde{a}_i$ $(i = 1, 2, 3)$: in particular, from their Figure 5, we obtain $\tilde{b} = 0.12$, and from their equation (7) the values of $\mathcal{R}_i$ and $\tilde{a}_i$. The parameters for the double-exponential disc and for its 3MN fit are summarised in Table 5.2, where $q_i = \tilde{a}_i/\tilde{b}_i$.

As a safety check of the reconstructed 3MN model, we compare the circular velocity in the equatorial plane of the double-exponential disc and of its 3MN fit (Fig. 5.5, top panel), that can be compared with Figure 3 of Smith et al. (2015), and the FO surface density profiles of the two models (Fig. 5.5, bottom panel) that in turn can be compared with their Figure 7. The circular velocity of the exponential disc is almost perfectly reproduced over the explored radial range, while the reproduction of the FO surface density is less satisfactory, an unavoidable consequence of the everywhere positive

Model	Parameters
Double-Exponential disc	$\alpha = R_\mathrm{d}/r_* = 1$ $\beta = h_\mathrm{d}/r_* = 0.1$ $\mathcal{R}_\mathrm{d} = 1$ $k = 1$
3MN fit (Smith et al., 2015)	$\tilde{b} = 0.12$ $q_1 = 4.64, \quad q_2 = 21.42, \quad q_3 = 18.67$ $\mathcal{R}_1 = 0.16, \quad \mathcal{R}_2 = -5.77, \quad \mathcal{R}_3 = 6.72$ $k = 1$

Table 5.2: The parameters of the double-exponential disc and its 3MN fit from Smith et al. (2015). For the meaning of the parameters of the double-exponential disc, see eq. (5.10). For the 3MN model, instead, we adopt the same notation of eq. (5.5), where $\tilde{b}$ is the same for all the three components, $q_i = \tilde{a}_i/\tilde{b}$, and $\mathcal{R}_i = M_{*i}/M_*$. The Jeans equations are solved in the isotropic case, with constant Satoh parameter $k = 1$.

decomposition adopted. For completeness, in Fig. 5.6, we present the EO surface density distributions of the two models. As expected, the two distributions are quite different in the outer regions, especially for increasing vertical distance from the equatorial plane, where the 3MN model produces higher surface density values. Consequently, also the kinematical fields obtained from the solution of the Jeans equations are expected to show significant differences, especially at high $|z|$.

5.3.2 Results for the dynamics of the double-exponential disc and its 3MN fit

We use our numerical procedure to evaluate the differences in the dynamical properties, a problem left open by the studies of Smith et al. (2015) and Rojas-Niño et al. (2016); we adopt for simplicity the case of the isotropic rotator, without DM halo and central BH. In Figure 5.7, the EO projected rotational velocity and velocity dispersion are shown. In this case, since we model a single-component system with constant mass-to-light ratio, it has no sense to look at luminosity-weighted quantities. The fields v_los of the two models look remarkably similar, also outside the equatorial plane. In particular, the percent error of the 3MN model with respect to the double-exponential model, in the equatorial plane, is $< 9\%$ out to $4\,R_\mathrm{d}$, and $< 14\%$ out to $10\,R_\mathrm{d}$ (we use the reference distances of $4\,R_\mathrm{d}$ and $10\,R_\mathrm{d}$ in analogy with Smith et al., 2015). This quite satisfactory result is not obvious a priori, since v_φ, at variance with v_c, is not a function of the potential only, but it also depends on the velocity dispersion via the asymmetric drift. Therefore, the excellent agreement of v_c in Fig. 5.5 is not a guarantee that also v_φ, and its projection v_los, are well reproduced by the 3MN density fit. The reproduction of v_los outside the equatorial plane is still quite good, with a slightly higher discrepancy at increasing $|z|$, as expected, but improving for larger galactocentric distances; for example, at $z = R_\mathrm{d}$,

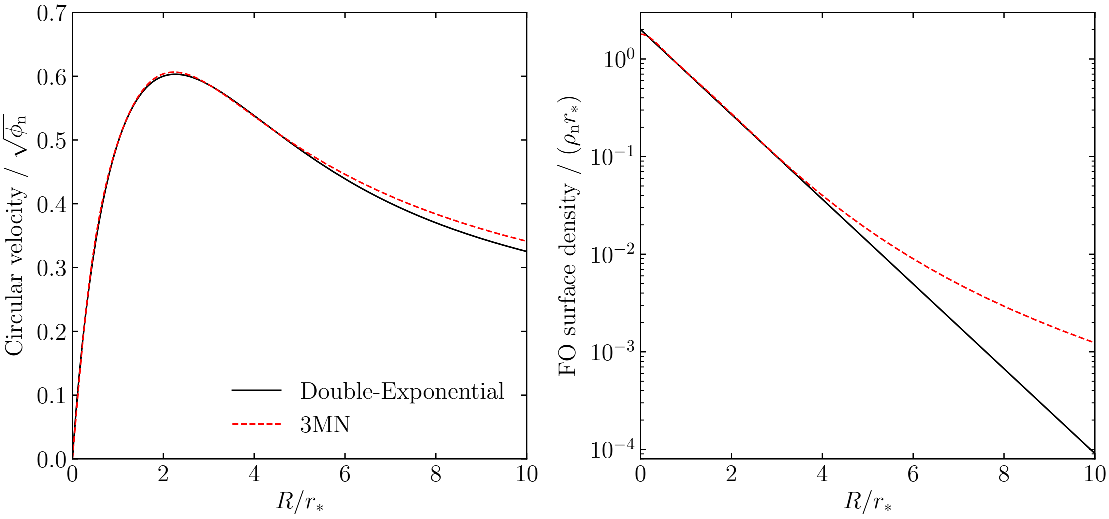

Figure 5.5: Circular velocity (left) and face-on surface density (right) profiles of the two models of Table 5.2; these plots can be compared with Figures 3 and 7 in Smith et al. (2015).

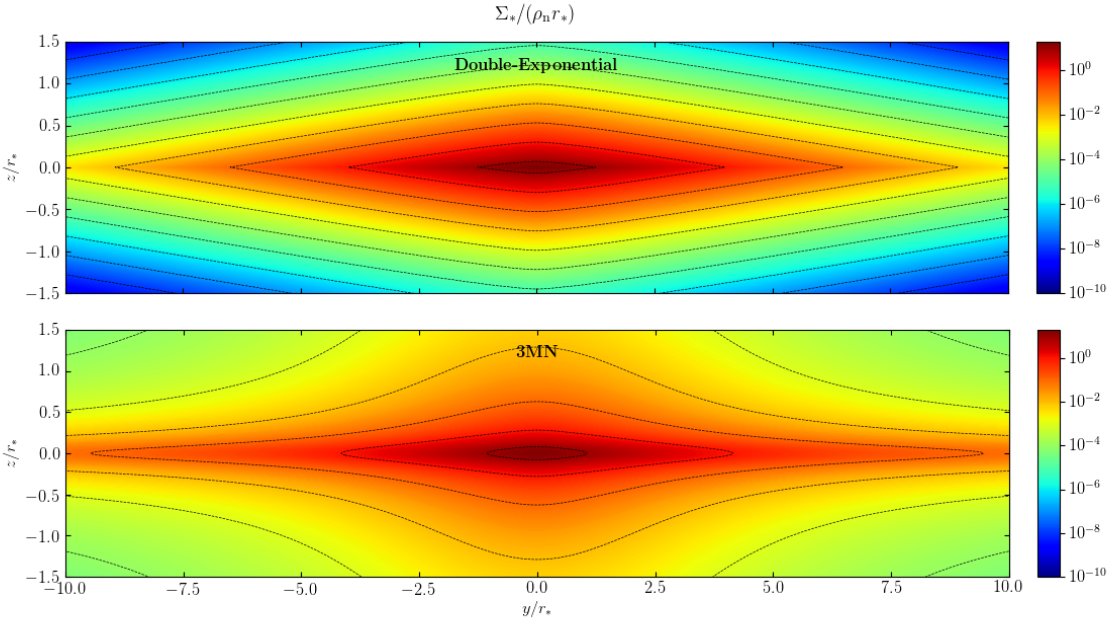

Figure 5.6: Edge-on surface density distributions Σ_* of the two models of Table 5.2. The dotted contours are spaced by 1 dex.

the percent error is $< 23\%$ out to $4\,R_\mathrm{d}$, reducing to $< 18\%$ out to $10\,R_\mathrm{d}$. The situation is different for σ_los: the two fields are significantly different, even in the equatorial plane, with the 3MN model showing values up to a factor of 2 larger than those of the double-exponential model. Moreover, the velocity dispersion of the 3MN model near the rotation

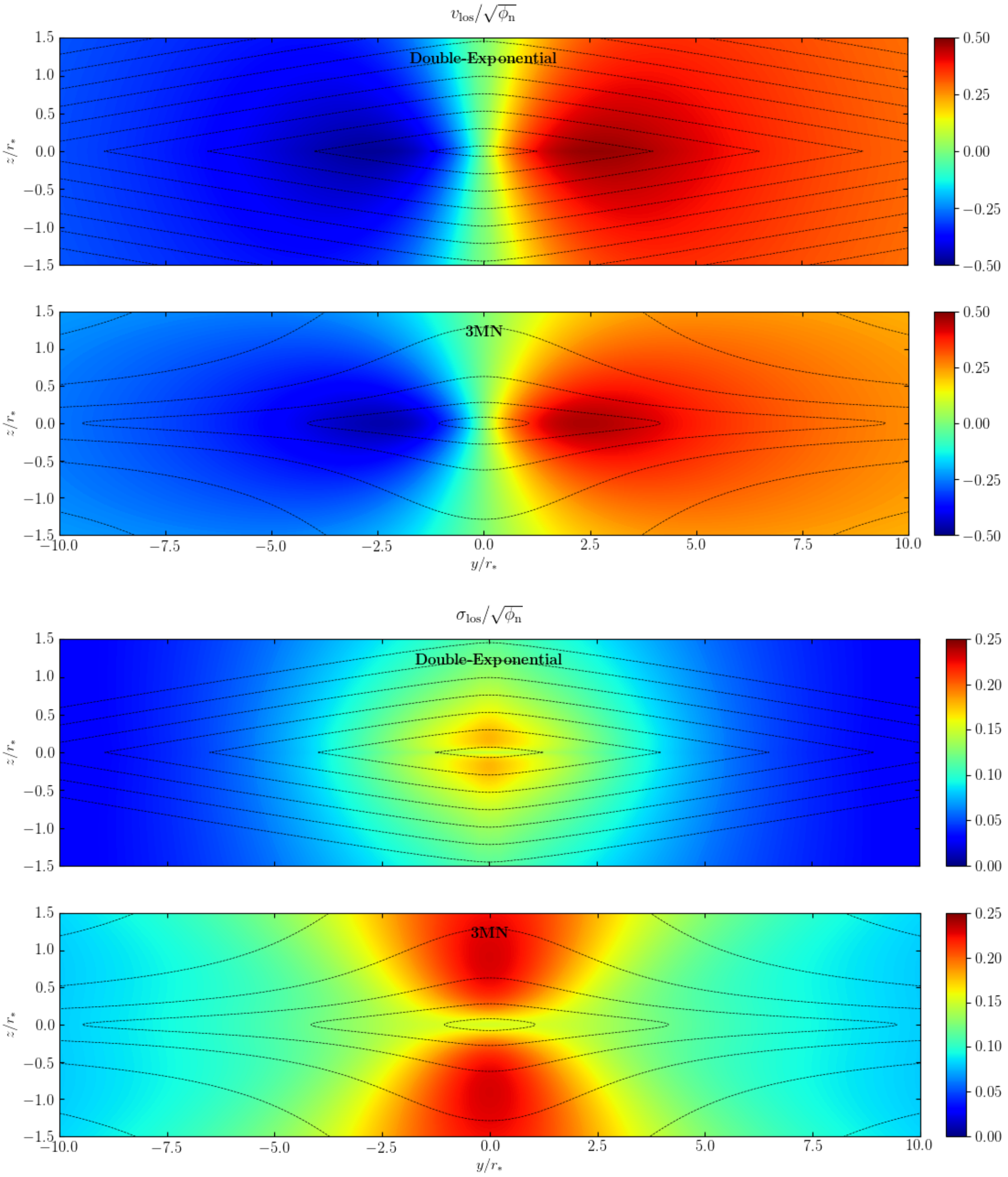

Figure 5.7: Edge-on projected rotational velocity $v_{\rm los}$, and velocity dispersion $\sigma_{\rm los}$, normalised to $\sqrt{\phi_{\rm n}}$, for the two models of Table 5.2. The dotted contours are the same as in Fig. 5.6.

axis presents a characteristic hourglass-shaped distribution (also observed e.g. by Negri, Ciotti and Pellegrini, 2014), only barely detectable at the very centre for the double-exponential model. Notice that this feature is not observed in the maps of Figure 5.4

for the JHD and JLD models, even if they also contain a MN component, due to the addition of a stellar halo and a DM halo, and to the different kinematical decompositions adopted (see also the discussion in Smet et al., 2015). These experiments suggest caution when adopting the 3MN representation to interpret the observed velocity dispersion of disc galaxies.

5.4 Summary

The galaxy models illustrated are meant to show the properties of some density models from our library, whose potential has been obtained with the methods presented in Chapter 4, and to show the results of the overall multicomponent modelling procedure presented in the previous Chapters. In particular, they offered the possibility to discuss in some details the role of the scaled density distributions chosen at the beginning of the Potential and Jeans Solver, and of the weights fixed in Post-Processing, and how they affect the resulting total galaxy properties, both internal and projected, and both mass- and luminosity-weighted. Summarising the methods here employed for the evaluation of the potentials, for the MN and the spherical NFW density distributions (and of course for the BH), the exact analytical potentials have been exploited, and for the ellipsoidal Jaffe distribution the analytical homoeoidally-expanded density-potential pair has been used; finally for the double-exponential disc, the potential has been calculated with the integral formula based on Bessel functions, in a very fast and very accurate manner. We stress that, indeed, for all the density models mentioned in the previous Chapter (including those factorised discs not yet inserted in JASMINE2), we have now the possibility to obtain the gravitational potential avoiding the most time-expensive 2D integration in terms of elliptic integrals. Thus, on the same line as this Chapter, we can build a variety of galaxy models, composed of different matter components, in a very fast and reliable way, and to flexibly vary the Post-Processing parameters. In the next Chapter, the exploration of the parameter space for some families of galaxy models is performed.

Chapter 6

Effects of galaxy structure and dynamics on gas flows in ETGs

We present a study carried out for the work in Ciotti et al. (2022; in this Chapter shortened to Paper), where axisymmetric and rotating models of ETGs, lying on the empirical Scaling Laws, are used to set the initial conditions for hydrodynamical simulations of gas flows. The goal is to study the evolution of some galaxy properties based on an exploration of the model parameter space. In this Chapter, we mainly focus on the structural and dynamical properties of the initial models, following the nomenclature and the modelling procedure presented in the previous Chapters. The solution of the Jeans equations are implemented in the numerical simulations in analytical form in homoeoidal expansion; we stress the role of JASMINE2 in testing the reliability of this approximation. The setup of the simulations, and the features of the hydrodynamical code MACER used for this study, are briefly reported, together with the main results from the evolution of the gas flows over a time spanning a few Gyr. The main global properties analysed concern the central BH accretion, the formation of (cold) gaseous and stellar discs, the star formation, the X-ray properties of the hot gas, including the effects of supernovae explosions and AGN feedback. In particular, we mainly focus on the effect of the galaxy shape and rotation on the evolution of gas flows driven by angular momentum conservation: we analyse a series of galaxy models for which also the numerical evolution has been studied, and we extend the analysis in Paper with some preliminary considerations about more flattened systems, modelled with JASMINE2, reaching degrees of flattening not allowed by the homoeoidal expansion.

Ciotti L., Ostriker J. P., Gan Z., Jiang B. X., Pellegrini S., Caravita C., Mancino A., 2022, Accepted for publication, ApJ

6.1 Introduction

As anticipated in the Introduction of Chapter 1, theoretical, numerical and observational studies of ETGs show a strong interplay between the ISM (produced by stellar mass losses and cosmological accretion from group/cluster environment) and the internal structure and stellar dynamics of the host galaxies. From an evolutionary point of view, this affects for example the cooling flows, the star formation, the BH accretion, and then the properties of the hot X-ray emitting corona surrounding the galaxies, and the amount of gas retained by and ejected from the galaxies, where indeed the feedback effects from supernovae explosions and central AGN play an important role (see e.g. Mathews and Brighenti, 2003; Kim and Pellegrini, 2012; Werner et al., 2019, for reviews).

In order to address these aspects, over the years, numerical simulations have been supplied by increasingly detailed treatment of galaxy structure and internal dynamics (e.g. shape and density profiles of stellar and DM distributions, velocity dispersion and rotational fields of the stellar component); physics of the ISM (cooling and heating mechanisms, evolution of the dust and metals content of the ISM, star formation processes, instabilities); accretion of the central supermassive BH and associated AGN feedback (radiative and mechanical feedback and its dependence on the local ISM properties, radiative transfer, cosmic-rays acceleration); group/cluster confining and accretion effects. In particular, we briefly review here the importance of the effects of the galaxy shape and rotation, based on observations and numerical works. From one side, flat and rotating ETGs are observed to host fainter and cooler X-ray emitting halos than ETGs of same optical luminosity but with rounder shape and less ordered rotation of the stellar component (e.g. Eskridge et al., 1995; Pellegrini et al., 1997; Sarzi et al., 2013; Kim and Fabbiano, 2015; Juráňová et al., 2020). On the other side, numerical simulations based on hydrodynamical codes (also carried out with the aid of a previous version of the code JASMINE2 for the study of the galaxy models, e.g. Posacki et al., 2013; Negri, Ciotti and Pellegrini, 2014; Negri, Posacki, Pellegrini and Ciotti, 2014; Negri et al., 2015) showed that indeed the galactic rotation can be very effective in enhancing ISM instabilities and leading to the formation of cold gaseous rotating discs, with substantial reduction of the X-ray luminosity, and lower emission temperatures of the ISM, in agreement with observations (see also e.g. Brighenti and Mathews, 1996, 1997; D'Ercole and Ciotti, 1998). These results have been successively confirmed also by simulations which take into account the effect of AGN feedback and using increasingly more realistic galaxy models (e.g. Ciotti et al., 2017; Pellegrini et al., 2018; Yoon et al., 2018).

Regardless of the specific topic of interest, the study of stellar systems may be faced with two different approaches, in some sense opposite and complementary, as also mentioned in Chapter 1: modelling specific real objects, reproducing their observed features, or modelling more general and arbitrary objects, reproducing global observed trends of galactic properties. In the specific case of the study of the evolution of gas flows in ETGs, this results in the following respective merits and limitations. In the first approach, it is possible to build well tailored galaxy models, but it is naturally not possible to know the specific evolutionary time at which the galaxy is observed, so that the results have to be interpreted in some time-averaged way. In the second approach, large samples of galaxy models are built, and global trends are derived, which are of course independent of specific differences from system to system, allowing for a global picture of real galaxies, and so in particular of the evolution of the ISM properties. Clearly, a thorough exploration of the model parameter space can be very time-expensive, depending on the complexity of the galaxy models, and on the spatial and temporal resolution adopted for the numerical simulations. In this scenario, the possibility of a flexible exploration of the parameter space of multicomponent galaxy models makes our modelling procedure, and in particular the scaling approach implemented in JASMINE2, a useful complementary tool for numerical simulations of galaxy evolution.

In Paper, the second approach is favoured: the evolution of ETGs is studied by means of hydrodynamical simulations performed with the latest version of the high-resolution 2D code MACER (Massive AGN Controlled Ellipticals Resolved), by using realistic dynamical models for the host galaxies. MACER, which is based on the Athena++ code (version 1.0.0; Stone et al., 2008, 2020), sees major improvements, with respect to the first versions (Ciotti and Ostriker, 2001, 2007; Novak et al., 2011), regarding the physical treatment of AGN and SNII feedback, the effects of rotation of the stellar component on the BH accretion, and the star formation and disc instabilities; moreover, in Gan, Ciotti, Ostriker and Yuan (2019, hereafter G19a), Gan, Choi, Ostriker, Ciotti and Pellegrini (2019, hereafter G19b), and Gan et al. (2020), additional improvements are thoroughly described, allowing for the inclusion of a suite of chemical elements, and the study of dust production and destruction. The aim of Paper is an exploration of the parameter space of the galaxy models, in particular concerning the shape and the rotational support of the stellar component, to study their effects on evolutionary properties. Over a time range of the order of few Gyr, we have analysed the formation of equatorial discs of cold gas and of newly formed stars, the time-dependent BH accretion rate and star formation rate, the evolution of the X-ray luminosity and of the emission-weighted temperature of the hot corona. Finally, the total BH accreted mass, the total amount of new stars, the final X-ray luminosity and temperature, the total mass ejected from the galaxy are obtained. A group/cluster DM halo is also included in the galaxy models, providing an important confining effect, and the cosmological accretion is also taken into account, in agreement with results from cosmological simulations. We also consider the time change of the stellar velocity dispersion and rotational velocity fields, due to mass loss of the stellar populations, and to the mass growth of the central BH.

As highlighted above, a major ingredient for the hydrodynamical simulations of galactic gas flows is represented by the galaxy models hosting the flows. The models are needed indeed in order to assign the gravitational field of the host galaxies, and the spatial and temporal distribution of the gas source terms (mass, momentum, and energy); besides, the momentum and energy terms require the specification of the galaxy internal dynamics. Structural and dynamical properties of the galaxy models have then an essential role in affecting the evolution of gas flows. Over the years, more and more realistic (and numerically tractable) models have been developed and employed in simulations. The galaxy models adopted in Paper are an extension of the models used in G19a, G19b, and

Gan et al. (2020), and are based on JJe models (CMPZ21), already presented in Section 5.1 (see also Sections 4.2.2 and 4.3). They include an ellipsoidal stellar distribution, and a galactic DM halo, as obtained from the JJe formalism, with a central supermassive BH, and an additional DM halo which accounts for the gravitational confining effect of the group/cluster hosting the galaxy. The evolutionary properties listed above have been analysed for a set of galaxy models, varying their total mass and size, accordingly to the Scaling Laws for ETGs (Faber and Jackson, 1976; Kormendy, 1977), and their rotational support, and finding results in good agreement with observations. In practice, accordingly with the modelling procedure presented in this Thesis, especially in Chapter 3 (see also the summary scheme of Fig. 3.1), we firstly build a *family* of galaxy models, characterised by the choice of the structural parameters; then we distinguish the models with different parameterisations for the kinematical decomposition; finally, the physical scales are assigned, satisfying the Scaling Laws, and building models of different physical dimensions. We obtain *specific* galaxy models characterised by different rotational supports, and by different total stellar mass and size.

In this Chapter, we present the work in Paper in the following way: we focus on the construction of the galaxy models used as input for the hydrodynamical simulations, and in particular on the contribution provided by the code JASMINE2, while we only briefly report the setup of numerical simulations and the main results achieved. We mention here that the Jeans equations for the stellar component, whose solution is needed for the hydrodynamical equations, are solved analytically in homoeoidal approximation, in the gravitational potential produced by the stars themselves, the galactic DM halo, and the central supermassive BH. In fact, the homoeoidal expansion, while very useful because it allows for fully analytical dynamical models, does not allow to take into account the effect on the stellar dynamics of the group/cluster DM halo. We exploit our code JASMINE2 to study its effect, and to assure that it can be safely neglected in the evaluation of the stellar dynamical fields, while of course it is fundamental for retaining gas. A second limit of the homoeoidal approximation faced in this investigation is that it is valid only for small flattening of the ellipsoidal density distributions, preventing the study of gas flows in quite flat galaxies. Although without running the simulations, we exploit JASMINE2 to build arbitrarily flat galaxy models, for which we give some predictions on cooling flows driven by angular momentum conservation.

In Sections 6.2 and 6.3, we recall the main structural and dynamical properties relevant for the construction of the galaxy models used for this set of simulations, and we give the specific parameters adopted. In Section 6.4, some considerations about the gas flows driven by the angular momentum conservation are discussed; important predictions can be done, indeed, even before the run of the simulations. In Section 6.5, from completeness, also the main results obtained from the hydrodynamical simulations are presented, while we refer to Paper for deeper discussions. Finally, in Section 6.6, we extend some considerations to models with different flattenings of the stellar components, as mentioned above.

6.2 Structure of the galaxy models

The stellar density distribution is described by an oblate ellipsoidal Jaffe model of total mass M_*, scale-length r_*, and flattening (axial ratio) $0 < q_* \leq 1$. We adopt the usual normalisations presented and employed in this Thesis, as defined in Section 3.2, so that all the lengths and masses are in units of r_* and M_*, respectively. By consequence, $\rho_{\rm n} = M_*/(4\pi r_*^3)$ and $\phi_{\rm n} = GM_*/r_*$, from eq. (3.9), are the normalisation coefficients for the densities and the potentials, respectively. Then, from eq. (4.1), the stellar density profile is given by

$$\rho_*(R,z) = \frac{\rho_{\rm n}}{q_*\, m_*^2(1+m_*)^2}, \qquad m_*^2 = \tilde{R}^2 + \frac{\tilde{z}^2}{q_*^2}. \tag{6.1}$$

It is useful to introduce the flattening parameter also as $\eta_* = 1 - q_*$, so that $\eta_* = 0$ corresponds to a spherical stellar distribution. In particular, the flattening of the stellar density model used for these simulations is set to $q_* = 0.7$ (i.e. $\eta_* = 0.3$), and in Fig. 6.1 the density profile in the equatorial plane is shown. We recall that the circularised effective radius $\langle R_{\rm e}\rangle$ of an ellipsoidal stellar system observed EO (edge-on) is related to the effective radius $R_{\rm e}$ of the same model in the spherical limit, or when observed FO (face-on), by $\langle R_{\rm e}\rangle = \sqrt{q_*} R_{\rm e}$; moreover, in the EO projection of an ellipsoidal system, the isophotal flattening coincide with the intrinsic flattening (see eq. 2.41 and the related footnote). As well known, the projected density profile of the Jaffe model is remarkably similar to the de Vaucouleurs law (eq. 4.13) over a quite large radial range, and $R_{\rm e} \simeq 0.75\, r_*$, in case of spherical symmetry and in the assumption of constant mass-to-light ratio (as reported just below eq. 4.1). Therefore, we can determine the scale radius r_* for our ellipsoidal Jaffe models once q_* and $\langle R_{\rm e}\rangle$ are fixed by observations. To complete the modelling of the stellar distribution, we disclose now that three values for the initial stellar mass M_* are explored in simulations, characterising three groups of galaxy models (whose parameters are summarised in Table 6.1): $M_* = 1.5 \times 10^{11}{\rm M}_\odot$, $3.4 \times 10^{11}{\rm M}_\odot$, and $7.8 \times 10^{11}{\rm M}_\odot$, respectively for the LM (low mass), MM (medium mass), and HM (high mass) model group.[1] The models lie on the Fundamental Plane of ETGs, so that the EO circularised effective radius $\langle R_{\rm e}\rangle$ (and consequently r_*) and the total luminosity ($L_{\rm B}$, in the B-band) are derived for the chosen values of M_*.

In JJe models the stellar distribution is embedded in a *galactic* DM halo, so that the *total* (stellar plus DM) galaxy density distribution is again described by a Jaffe ellipsoidal distribution of total mass $M_{\rm g} = \mathcal{R} M_*$, flattening $q_{\rm g}$, and scale length $r_{\rm g} = \xi r_*$:

$$\rho_{\rm g}(R,z) = \frac{\rho_{\rm n}\mathcal{R}\xi}{q_{\rm g} m_{\rm g}^2(\xi + m_{\rm g})^2}, \qquad m_{\rm g}^2 = \tilde{R}^2 + \frac{\tilde{z}^2}{q_{\rm g}^2}; \tag{6.2}$$

in the present models we always assume the natural choice of $\xi \geq 1$, and for simplicity we restrict to the case of spherically symmetric $\rho_{\rm g}$, i.e. $q_{\rm g} = 1$. The latter approximation

---

[1] The explored models correspond to galaxies that are massive enough that the evolution of the gaseous halo is not entirely dominated by SNIa heating, being smaller systems able to sustain galactic winds just due to the SN energy input.

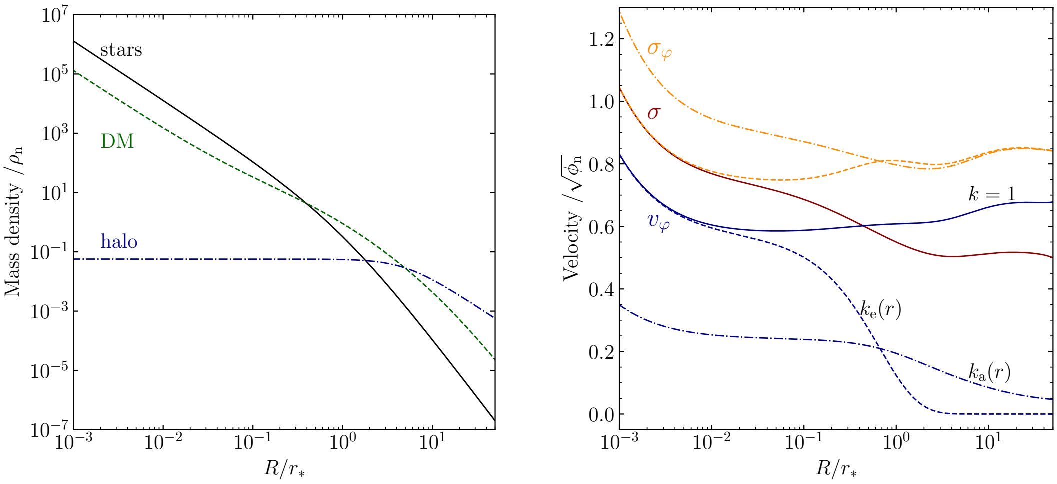

Figure 6.1: On the left, radial profiles in the equatorial plane ($z = 0$) of the mass densities of the stellar component (solid black), the galactic DM halo ('DM', dashed green), and the group/cluster DM halo ('halo', dot-dashed blue), described in Section 6.2, and normalised to $\rho_n = M_*/(4\pi r_*^3)$. The galactic DM profile dominates around few $\langle R_e \rangle$, while the external DM dominates in the outermost regions. On the right, radial profiles in the equatorial plane of the vertical (and radial) velocity dispersion σ (solid red), and of the azimuthal velocity dispersion σ_φ (orange) and rotational velocity v_φ (blue), with different line-styles depending on the kinematical decomposition, all normalised to $\sqrt{\phi_n} = \sqrt{GM_*/r_*}$. For all the models, the Satoh k-decomposition is adopted: the solid blue line is v_φ of the isotropic rotator ($k = 1$), while of course in this case $\sigma_\varphi = \sigma$; the dot-dashed lines represent the asymptotically flat case ($k = k_a(r)$), and the dashed lines the exponentially declining case ($k = k_e(r)$), in eq. (6.10). The effect of the central supermassive BH is clearly visible in the innermost regions; notice also that in the exponential decomposition the stars rotate faster in the inner regions (like the isotropic rotator) than in the asymptotically flat decomposition, while rotation is the lowest in the outer regions. For the galaxy models of the simulations, the values of ρ_n and ϕ_n can be obtained from Table 6.1.

is quite acceptable for moderately flattened galaxies (as the isopotential surfaces are in general rounder than the associated mass density), with the additional advantage of a simple expression for the galaxy gravitational field, and of analytical expressions for the solution of the Jeans equations in homoeoidal expansion, of easy implementation in the hydrodynamical code. In the spherical limit, the total galaxy mass contained in a sphere of radius r, and the galaxy potential, are given by

$$M_g(r) = \frac{M_* \mathcal{R} s}{\xi + s}, \qquad \phi_g(r) = -\frac{\phi_n \mathcal{R}}{\xi} \ln\left(\frac{\xi + s}{s}\right), \qquad s = \frac{r}{r_*}, \tag{6.3}$$

in agreement with eq. (4.2). Since in JJe models ρ_g and ρ_* are assigned, a condition for the positivity of the density distribution of the galactic DM halo $\rho_{DM} = \rho_g - \rho_*$ (shown in Fig. 6.1) is needed. From eq. (13) in CMPZ21[2], imposing $\xi \geq 1$ and $q_g = 1$, the

---

[2] The positivity condition of eq. (6.4) is obtained in Appendix A in CMPZ21; the proof is analogous to Appendix E at the end of this Thesis, but in a different formalism: we recall that, in fact, our Appendix is recast for JJE models of Section 5.1, where the normalisation scales, r_* and M_*, represent the scale-

positivity condition reduces to

$$\mathcal{R} \geq \mathcal{R}_{\mathrm{m}} = \frac{\xi}{1-\eta_*}. \tag{6.4}$$

A model with $\mathcal{R} = \mathcal{R}_{\mathrm{m}}$ is called *minimum halo* model; it can be shown that, in this case, ρ_{DM} is well described by the NFW profile (eq. 4.3) over a large radial range (Ciotti and Ziaee Lorzad 2018, Ciotti et al. 2019, CMPZ21): for this reason, in the simulations, the initial galaxy parameters are fixed to the minimum halo case, in particular with $\xi = 12.6$, and so $\mathcal{R} = 18$. Notice that the total galaxy (stars plus DM) density profile ρ_{g} in eq. (6.2) is proportional to r^{-2} inside r_{g}: this property is one of the motivations behind the construction of JJe models, since different theoretical and observational findings support this assumption over a large radial range (see e.g. Gavazzi et al., 2007; Koopmans et al., 2009; Auger et al., 2010; Barnabè et al., 2011; Cappellari et al., 2015; Serra et al., 2016; Poci et al., 2017; Lyskova et al., 2018; Li et al., 2018; Bellstedt et al., 2018; Wang et al., 2019, 2020).

In order to take into account the effects of a group/cluster DM halo on the gas flows, we also consider the gravitational field produced by a spherically symmetric quasi-isothermal DM halo of asymptotic circular velocity v_{h}, and scale-length $r_{\mathrm{h}} = \xi_{\mathrm{h}} r_*$, so that

$$\rho_{\mathrm{h}}(r) = \frac{v_{\mathrm{h}}^2}{4\pi G r_*^2 (\xi_{\mathrm{h}}^2 + s^2)}, \qquad M_{\mathrm{h}}(r) = \frac{v_{\mathrm{h}}^2 r_*}{G}\left[s - \xi_{\mathrm{h}} \arctan\left(\frac{s}{\xi_{\mathrm{h}}}\right)\right], \tag{6.5}$$

and

$$\phi_{\mathrm{h}}(r) = v_{\mathrm{h}}^2 \left[\ln\left(\sqrt{1 + s^2/\xi_{\mathrm{h}}^2}\right) + \frac{\arctan(s/\xi_{\mathrm{h}})}{s/\xi_{\mathrm{h}}} - 1\right], \tag{6.6}$$

from eqs. (4.5) and (4.6), recast here as functions of v_{h}. Notice that in eqs. (6.3) and (6.6) we fixed $\phi_{\mathrm{g}}(\infty) = \phi_{\mathrm{h}}(0) = 0$. In the simulations we consider models with $\xi_{\mathrm{h}} \gg 1$, so that the group/cluster DM component does not alter significantly the internal dynamics of the models, as we show in details in Section 6.3.1. In particular, for these models, we set $\xi_{\mathrm{h}} = 5$, in order to have a quite flat total rotation curve in the equatorial plane, as shown in Fig. 6.2 (and apparent especially with a linear radial scale, on the right plot). Moreover, v_{h} is fixed equal to the central value of the circular velocity due to the galaxy (stars plus DM), as can be seen in the same figure, and we discuss below in eq. (6.14).

The stellar mass $\langle M_* \rangle(r)$ contained in a sphere of radius r, centred in the origin is easily computed in the homoeoidal expansion approximation, and we have

$$\langle M_* \rangle(r) = \frac{M_* s}{1+s}\left[1 + \frac{\eta_*}{3(1+s)}\right], \tag{6.7}$$

from eqs. (15) and (16) in CMPZ21, so that the total DM mass (galactic plus group/-cluster) inside the same sphere is

$$M_{\mathrm{DMtot}}(r) = M_{\mathrm{DM}}(r) + M_{\mathrm{h}}(r) = M_{\mathrm{g}}(r) - \langle M_* \rangle(r) + M_{\mathrm{h}}(r). \tag{6.8}$$

---

length and the total mass, respectively, of the *total* density distribution. Here, instead, they represent the scale-length and the total mass of a *component* of the total galactic system (stars plus DM).

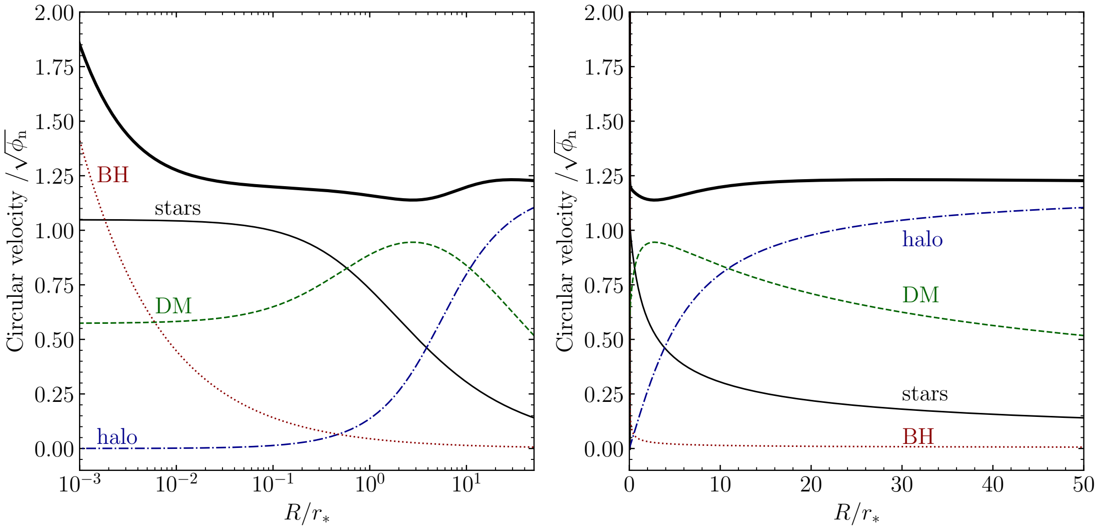

Figure 6.2: With a thick black line, the total circular velocity of the galaxy models, in the equatorial plane ($z = 0$), is shown (eq. 6.15), in units of $\sqrt{\phi_n} = \sqrt{GM_*/r_*}$ (whose value is given in Table 6.1 for the specific galaxy models of the simulations). The curves below show the contributions of the different mass components: the central supermassive BH (dotted red), the stellar component (solid black), the galactic DM halo ('DM', dashed green), and the group/cluster DM halo ('halo', dot-dashed blue). The radial profiles are shown with a logarithmic radial scale on the left, and with a linear radial scale on the right, to better appreciate the effects of the different potential components in the inner and outer regions, respectively, as discussed in Sections 6.3.1 and 6.3.2.

For the three groups of models in Table 6.1, it follows that $M_{\rm DMtot}(r)/M_{\rm g}(r) \simeq 52\%$ at $r = \langle R_{\rm e}\rangle$, and $\simeq 64\%$ at $r = 2\langle R_{\rm e}\rangle$ for $\eta_* = 0.3$, and for reference $\simeq 39\%$ at $r = R_{\rm e}$, and $\simeq 55\%$ at $r = 2R_{\rm e}$, for $\eta_* = 0$.

Finally, a supermassive BH of initial mass $M_{\rm BH} = \mathcal{R}_{\rm BH} M_*$, with an initial value of $\mathcal{R}_{\rm BH} = 10^{-3}$ (half of the currently observationally estimated value, see e.g. Kormendy and Ho 2013, as instead used in applications in Chapter 5), is added at the centre of the galaxy, with

$$\phi_{\rm BH}(r) = -\frac{\phi_{\rm n}\mathcal{R}_{\rm BH}}{s}, \tag{6.9}$$

in agreement with eq. (2.7).

6.3 Internal dynamics

The internal dynamics of the galaxy models, i.e. their velocity dispersion and ordered rotation fields, is a crucial ingredient of the problem, as it determines the momentum and kinetic energy sources associated with stellar mass losses that enter the hydrodynamical equations. The kinematical fields are obtained by solving the Jeans equations for the density ρ_*, under the usual assumption of a two-integral phase-space DF (eq. 2.10), and after the choice of a decomposition of the azimuthal motions (see Section 2.3). In

Model	$L_{\rm B}$ $(10^{11}\,L_{\rm B,\odot})$ (1)	M_* $(10^{11}\,{\rm M_\odot})$ (2)	r_* (kpc) (3)	$\langle R_{\rm e}\rangle$ (kpc) (4)	$v_{\rm g}(0)$ $({\rm km\,s^{-1}})$ (5)	$\sigma(0)$ $({\rm km\,s^{-1}})$ (6)	$\sqrt{\phi_{\rm n}}$ $({\rm km\,s^{-1}})$ (7)	$v_{\rm h}$ $({\rm km\,s^{-1}})$ (8)
LM	0.32	1.54	7.33	4.57	360	223	301	360
MM	0.65	3.35	11.29	7.04	427	265	357	427
HM	1.38	7.80	18.94	11.80	504	312	421	504

Table 6.1: Structural and dynamical properties of the three groups of galaxy models. For the group name on the left, each column gives: (1) the galaxy luminosity in the B-band, (2) the initial stellar mass, (3) the scale-length of the stellar distribution (eq. 6.1), (4) the edge-on circularised effective radius (below eq. 6.1), (5) the galaxy central circular velocity (in absence of the BH and in the minimum halo case, eq. 6.14), (6) the stellar central velocity dispersion (in absence of the BH, eq. 6.12), (7) the normalisation coefficient for the velocities of the models, and (8) the asymptotic circular velocity of the quasi-isothermal DM halo (eq. 6.5), equal to $v_{\rm g}(0)$ (eq. 6.14). For all models, the flattening of the stellar distribution in eq. (6.1) is fixed to $q_* = 0.7$ (i.e. $\eta_* = 0.3$), the initial BH-to-stellar mass ratio in eq. (6.9) is $\mathcal{R}_{\rm BH} = 10^{-3}$, the parameters characterising the total galaxy density in eq. (6.2) are $\xi = 12.6$ and $\mathcal{R} = 18$, corresponding to a minimum-halo model from eq. (6.4), and the scale-length of the quasi-isothermal halo in eq. (6.5) is $\xi_{\rm h} = 5$.

particular, the Jeans equations for the stellar component are solved both numerically with JASMINE2, and analytically in homoeoidal approximation with the formulae of CMPZ21. The fully analytical form (given in Appendix A in Paper), not only allows for a simple numerical implementation in simulations (see also G19a), but it also allows to follow the secular changes of the gravitational and kinematical fields due to the stellar mass losses and the mass growth of the central BH, just by imposing the required time-dependence on the structural parameters (see Appendix B in Paper). We also consider the effects on the gas flows of the (time-dependent) gravitational field associated with the formation of the stellar disc in the equatorial plane (see Section 3 in Paper for details), and with the gravitational field of a group/cluster DM halo; for simplicity, instead, we do not consider their effects on the stellar dynamical fields, so the formulae in the Appendices in Paper give the dynamical fields produced by the total galaxy mass distribution (disc excluded) and the central BH.

In the following Section 6.3.1, we prove that we can safely adopt this approximation, thanks to the comparison with the numerical solution of the Jeans equations in the total initial gravitational potential performed with our code JASMINE2. In the successive Section 6.3.2, the most relevant properties about the internal dynamics of the galaxy models presented in Section 6.2, and used for the simulations, are given.

6.3.1 Applicability of the homoeoidal approximation

The assumption of homoeoidal expansion, and the neglect of the effect of the group/-cluster DM halo on the stellar dynamics inside a few effective radii of the galaxy (corresponding to more than 99% of the total stellar mass), are checked with respect to numerical results obtained with JASMINE2. We build a model as described in the Section 6.2, where the density distributions of the stellar and galactic DM halo are given in homoeoidal expansion, and so their potentials (following CMPZ21; see also Section 4.2.2), and the group/cluster DM halo and the central BH are added to the total gravitational potential. Then the Jeans equations are solved numerically with JASMINE2, without truncation in the flattening order, for the stellar distribution in the total initial gravitational potential; see Section 4.3 for a detailed description of the difference between numerical and analytical results (and some tests on the homoeoidal approximation). We stress that, in Section 4.3, we show the level of approximation of the expanded solution of the Jeans equations for a single stellar Jaffe component (also in the specific case of flattening $q_* = 0.7$, as used for the current models); since here the stellar component is embedded in a total spherical Jaffe distribution (with exact analytical potential), the discrepancy from the *true* solution is even smaller than the discrepancy shown in Section 4.3. Now we show in particular that the effect of the group/cluster DM halo on the stellar dynamics within $\approx 2R_{\rm e}$ is in fact negligible, as clearly visible by the rotation curves in the equatorial plane in Fig. 6.2, especially with a logarithmic radial scale, in the left plot. Also in the velocity profiles in Fig. 6.1, its effect can be seen as dominant only at large radii. We can safely conclude that, for the purposes of the present hydrodynamical simulations, the formulae in Appendix A in Paper can be adopted: the stellar dynamics is recovered in homoeoidal approximation and determined by the effect of the gravitational potential produced by the stellar ellipsoidal component ρ_* itself, the galactic DM halo $\rho_{\rm DM}$, and the central BH, as in JJe models of CMPZ21.

6.3.2 Dynamical properties

We present here the main dynamical properties relevant for the setup of the simulations. The azimuthal velocity field is split in its ordered and dispersion contributions, v_φ and σ_φ, respectively, by adopting the standard Satoh k-decomposition of eq. (2.25), with the expressions for the solution of the Jeans equations, σ and Δ, given in Appendix A in Paper. We recall that $k = 1$ corresponds to the isotropic rotator, while $k = 0$ describes a galaxy with a flattening totally supported by tangential velocity dispersion. In addition to the standard case with constant k, we also explore two more models of rotating galaxies, with a spatially-dependent Satoh parameter:

$$k_{\rm a}(r) = k_0 + (k_\infty - k_0)\frac{s}{\xi_0 + s}, \qquad k_{\rm e}(r) = {\rm e}^{-r/\langle R_{\rm e}\rangle}, \tag{6.10}$$

where in the first case we adopt the same parametrisation of eq. (5.8), and we set $k_0 = 0.42$, $k_\infty = 0.05$, $\xi_0 = 2.67$. In the right plot of Fig. 6.1, the effect of the three different kinematical decompositions on v_φ and σ_φ can be seen (recalling that $\sigma_\varphi = \sigma$ when $k = 1$). In particular, at large radii, in the first case v_φ becomes asymptotically flat, while in the second exponential case v_φ decreases significantly; in the central region, instead, stars of a model with $k = k_{\rm e}(r)$ rotate almost as fast as an isotropic rotator, faster than those in the asymptotically flat case with $k = k_{\rm a}(r)$, as at the centre $k_{\rm a}(0) = k_0$ is lower than unity.

To set up realistic galaxy models, we recall that their stellar central velocity dispersion, in absence of the central BH, can be obtained combining eqs. (26) and (42) in CMPZ21 (the former with $\mathcal{R} = \xi = 1$ and $\eta_{\rm g} = \eta_*$, and the latter with $\mathcal{R}_{\rm BH} = 0$ and $\eta_{\rm g} = 0$):

$$\sigma^2(0) = \frac{\phi_{\rm n}\mathcal{R}}{2\xi}\frac{1-\eta_*\cos^2\theta}{1+\eta_*-2\eta_*\cos^2\theta}. \tag{6.11}$$

For minimum halo models (i.e. $\mathcal{R} = \mathcal{R}_{\rm m}$ from eq. 6.4), when evaluating the limit[3] along the equatorial plane, it becomes

$$\sigma^2(0) = \frac{\phi_{\rm n}}{2(1-\eta_*^2)}, \tag{6.12}$$

so that $\sigma(0)/\sqrt{\phi_{\rm n}} \simeq 0.74$ for $\eta_* = 0.3$, and this would be the central value of the radial profile in the equatorial plane of $\sigma/\sqrt{\phi_{\rm n}}$, in absence of the BH, in the right plot of Fig. 6.1. We adopt $\sigma(0)$ as a proxy for the observed velocity dispersion of the galaxy in the central regions (outside the sphere of influence of the central BH). Moreover, at the centre of the galaxy, in absence of the BH, the circular velocity of JJe models in the equatorial plane is given by

$$v_{\rm g}^2(0) = \frac{\phi_{\rm n}\mathcal{R}}{\xi}, \tag{6.13}$$

and again, for minimum halo models,

$$v_{\rm g}^2(0) = 2(1+\eta_*)\sigma^2(0), \tag{6.14}$$

which gives $v_{\rm g}(0)/\sqrt{\phi_{\rm n}} \simeq 1.20$ (see Fig. 6.2), with the central value of $\sigma(0)$ estimated above, $\eta_* = 0.3$, and recalling that $v_{\rm g}^2(r) = v_*^2(r) + v_{\rm DM}^2(r)$, which includes the contributions of the stars and the galactic DM halo. The value of $v_{\rm g}(0)$ is also equal to the asymptotic value at large radii of the circular velocity due to the external DM halo, $v_{\rm h}$, by construction.

Finally, the model circular velocity in the equatorial plane $v_{\rm c}^2(r) = v_{\rm BH}^2(r) + v_{\rm g}^2(r) + v_{\rm h}^2(r)$, in case of minimum halo, can be written as

$$v_{\rm c}^2(r) = 2(1-\eta_*^2)\left(\frac{\mathcal{R}_{\rm BH}}{s} + \frac{\mathcal{R}_{\rm m}}{\xi+s}\right)\sigma^2(0) + \left[1 - \frac{\xi_{\rm h}}{s}\arctan\left(\frac{s}{\xi_{\rm h}}\right)\right]v_{\rm h}^2, \tag{6.15}$$

where we neglect for simplicity the contribution of the equatorial stellar disc formed by cooling and rotating ISM (see Section 3 in Paper). It is immediate to see that at the centre $v_{\rm h}(0)$ is zero, so $v_{\rm c}^2(0) = v_{\rm g}^2(0) = v_{\rm h}$, in absence of central BH (see Fig. 6.2).

6.4 Gas flows driven by angular momentum conservation

We spend some words about another quantity determined by the structure and dynamics of a rotating system, and which is essential to understand gas flows: the angular

---

[3] The central velocity dispersion of ellipsoidal JJe models is discontinuous, with values dependent on the direction approaching the centre (for a full discussion, we refer to CMPZ21).

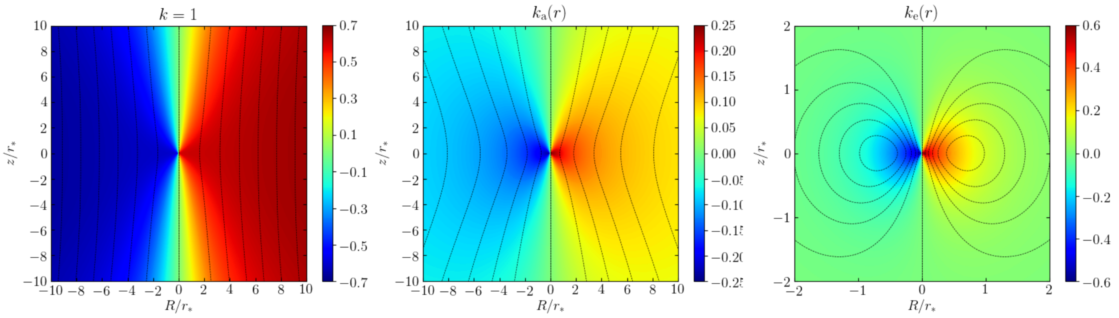

Figure 6.3: Maps of stellar rotational velocity v_φ, for the isotropic rotator (left), and for the two spatially dependent Satoh decompositions in eq. (6.10), i.e. the asymptotically flat case (middle) and the exponentially declining case (right). The velocity values are in units of $\sqrt{\phi_{\rm n}} = \sqrt{GM_*/r_*}$, whose value is given in Table 6.1 for the specific galaxy models of the simulations. The dotted lines represent surfaces of constant angular momentum per unit mass, J_z, of the stellar component. As discussed in Section 6.4, in absence of mass sources and viscous dissipation, for a gaseous halo rotating with the same velocity v_φ of the stars, the cooling gas falls along these lines, reaching the radius $R_{\rm in}$ on the equatorial plane (i.e. where the surfaces of constant J_z cross the plane), and then contract to $R_{\rm fin}$, as shown in Fig. 6.4. Notice the zoom-in of the last panel, to appreciate the rotation, limited to a very central region.

momentum. The z-component of the stellar angular momentum (per unit mass) is defined as $J_z = Rv_\varphi$, where the rotational velocity v_φ depends on the adopted kinematical decomposition. For these simulations, the Satoh k-decomposition is applied to all the galaxy models, and so J_z depends on the choice of the parameter k: in Fig. 6.3, we show the distribution of v_φ in the meridional plane (i.e. $R - z$ plane), with the superimposed curves representing surfaces of constant J_z, for the different choices of $k = 1$, $k_{\rm a}(r)$, $k_{\rm e}(r)$, from eq. (6.10); of course in case of $k = 0$, there is no net rotation, and the angular momentum is everywhere null. We also define the quantity $J_{\rm c} = Rv_{\rm c}$, related to the circular velocity (eq. 6.15), and so defined only in the equatorial plane, and independent of the decomposition of the azimuthal motions.

In this Section, we limit to considerations based on the structural and dynamical properties of the galaxy models, while in Section 6.5 the results of the evolution are reported. However, let us see for a while the equation for the time evolution of J_z of the gas, subjected to the angular momentum injection due to stellar evolution.[4] Due to the axisymmetry of the simulations (and ignoring for simplicity viscosity effects of the inflows, at variance with the evolution of the equatorial cold gas discs, where α-viscosity is taken into account), it is easy to show that along the paths of fluid elements,

$$\frac{DJ_z}{Dt} = \frac{\dot{\rho}}{\rho} R\,(v_\varphi - u_\varphi), \tag{6.16}$$

---

[4] In the simulations, the mass sources terms for the galactic gas flows are represented by mass losses from stars (red giants, AGB stars, and SNIa/SNII explosions, computed following the prescriptions of stellar evolution), and by a time-dependent cosmologically motivated mass accretion rate from the group/cluster environment, imposed at the outer boundary of the numerical grid.

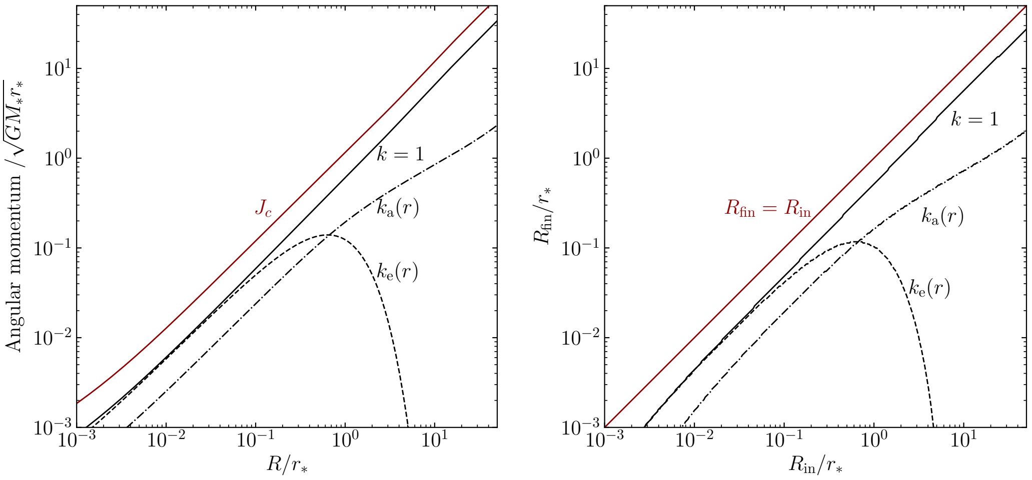

Figure 6.4: On the left, with black lines, the radial profiles in the equatorial plane ($z = 0$) of the angular momentum per unit mass, J_z, of the stellar component, for the three kinematical decompositions adopted: isotropic rotator (solid), asymptotically flat case (dot-dashed), and exponentially declining case (dashed). With the red line, the radial profile of J_c is shown for reference. Following the explanation of Section 6.4, cooling gas reaching the equatorial plane at a radius R_{in} (see also Fig. 6.3) moves inwards to R_{fin}, so that $J_z(R_{in}, 0) = J_c(R_{fin})$. In the right plot, the movement of the gas in the equatorial plane from R_{in} to R_{fin} is explicit.

where D/Dt is the lagrangian derivative, and $v_\varphi - u_\varphi$ is the difference between the stellar and the gas azimuthal velocity. The numerical simulations show that this difference is quite small, so that as a zeroth-order approximation we can assume J_z is conserved. In this simplified assumption, in rotating models, the stellar mass losses are injected in the ISM following v_φ, and the cooling gas falls along the curves of constant J_z, as in Fig. 6.3, preserving its initial angular momentum, and reaching the equatorial disc at R_{in}, i.e. where the surfaces of constant J_z cross the plane. However, due to the asymmetric drift, the rotational velocity of the gas is lower than the galaxy local circular velocity, so $J_z(R_{in}, 0) < J_c(R_{in})$; then the gas moves inwards in the plane, ending on a circular orbit of radius R_{fin}, where $J_z(R_{in}, 0) = J_c(R_{fin})$, meaning $R_{in} v_\varphi(R_{in}, 0) = R_{fin} v_c(R_{fin})$. On the left plot of Fig. 6.4, the two measures of the angular momentum in the equatorial plane are shown, where the black lines represent $J_z(R_{in}, 0)$ regarding to the different rotational supports of the models, and the reference red line represents $J_c(R_{in})$, clearly larger than $J_z(R_{in}, 0)$ at each radius. Moreover, on the right plot, the movement from R_{in} to R_{fin} is explicit.

From Fig. 6.3, we see that the gas falls onto the disc at significantly larger radii in the isotropic rotator than in the mildly rotating models, and from Fig. 6.4 we also see that it moves less inwards in more rotating systems. This suggests that more rotating models will develop larger discs of cold and dense gas in the equatorial plane. The runs of the simulations confirm this prediction, as reported in Section 6.5, showing also the effect of the gas disc properties on the accretion onto the BH, and on the formation of newly formed stars on the equatorial discs. Notice that curious curves of constant J_z are obtained for the model with exponentially declining rotation (last panel in Fig. 6.3): the curves are very inclined towards the centre and *closed*, so that the same value of J_z can be found at a very small radius and at a larger radius. This implies that gas particles which fall at such a large radius, in this prescription for the gas flows, are destined to move on the plane down to the same inner radius than particles arrived on the plane at the smaller radius, as visible in Fig. 6.4. Simulations confirm, in particular, that models with this parametrisation of the streaming velocity field produce gaseous discs confined in the inner regions.

Furthermore, in Section 6.6, we extend the analysis of gas inflows due to angular momentum conservation to similar galaxy models with different degrees of flattening, exploiting also the knowledge achieved from the results of the simulations.

6.5 Summary of the main results from hydrodynamical simulations

A detailed presentation of the setup of the hydrodynamical simulations is given in Paper and references therein, while in this Section, like in previous Sections, we only recall some features when needed. The simulations are performed with the high-resolution 2D hydrodynamical code MACER, introduced in Section 6.1.

The run of numerical simulations for a systematic and complete exploration of the model parameter space would be impossible, due to the computational time required by each run (see details in Paper), and to the number of model parameters. Therefore, we fix the properties of the galactic and the group/cluster DM halos, and the initial BH-to-stellar mass ratio, together with the galaxy flattening. We restrict the investigation to the combination of three values for the total initial stellar mass, M_*, already introduced as LM, (low mass), MM (medium mass), HM (high mass), with three kinematical decompositions: no rotation ($k = 0$, all the galaxy flattening is due to tangential velocity dispersion), moderate rotation ($k = k_{\rm e}(r)$, rotation exponentially declining in the outer regions), and the isotropic rotator case ($k = 1$, all the galaxy flattening is supported by ordered rotation). The parameters of the galaxy models, discussed in the previous Sections for each mass component, are reported in Table 6.1. The age of the galaxy at the beginning of the simulation is fixed to be 2 Gyr, so that the initial phases of galaxy formation are terminated, and a central supermassive BH with a mass near to the observed values of $\mathcal{R}_{\rm BH} \sim 2 \times 10^{-3}$ (e.g. Kormendy and Ho, 2013) is assumed to be already in place.

In the following, the main results obtained from the evolution of these galaxy models, over a time range spanning from 2 Gyr to 13.7 Gyr, are summarised, with a focus on the topics manly discussed in this Chapter. The study of Paper mainly concern the following aspects of galaxy evolution: the BH accretion, the formation of gaseous and stellar discs in the equatorial plane, the star formation, and the luminosity and temperature of the X-ray emitting gas of the hot corona. The discussion is driven by the study of the effects

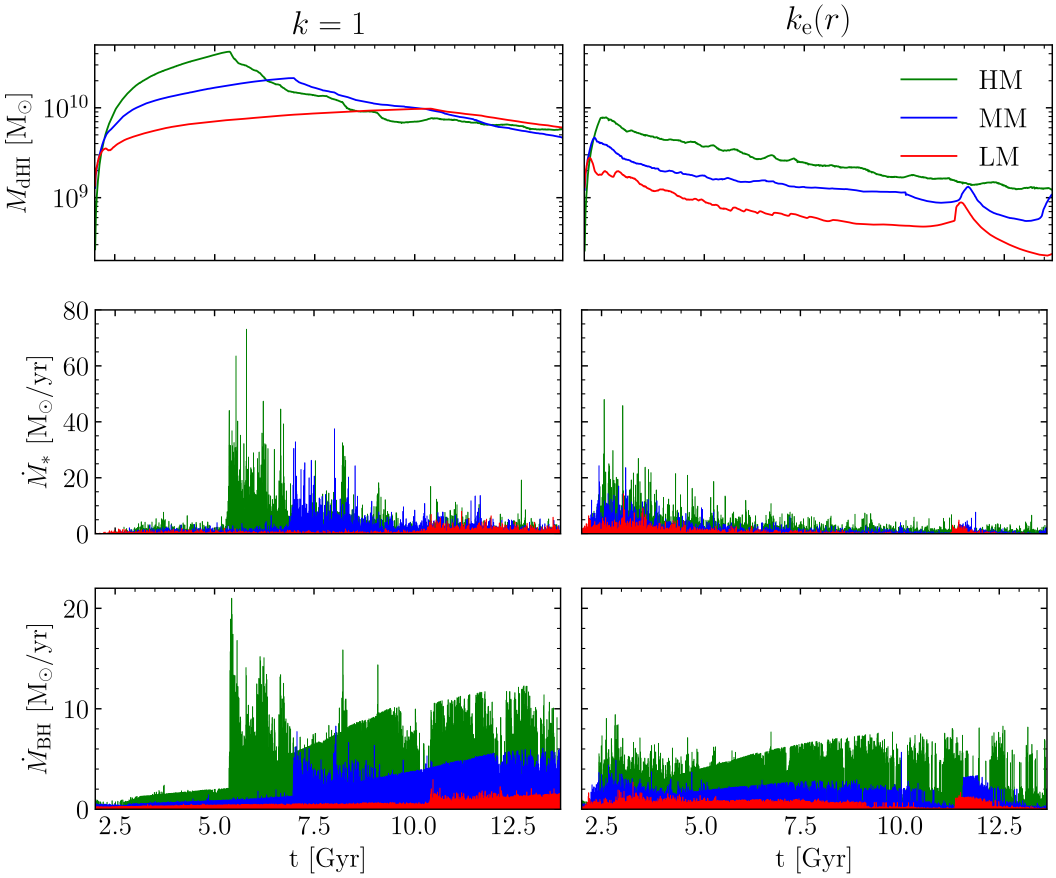

Figure 6.5: From top to bottom, the time evolution of the total mass of cold gas $M_{\rm dHI}$ ($T \leq T_{\rm c} = 5\times10^5$ K) in the equatorial disc, the star formation rate $\dot{M}_*$, and the BH accretion rate $\dot{M}_{\rm BH}$, from 2 Gyr to 13.7 Gyr. All the quantities are shown for the three groups of models, meaning high-mass ('HM', green), medium-mass ('MM', blue), and low-mass ('LM', red) galaxy models, and for two degrees of rotational support: $k = 1$ on the left, and $k = k_{\rm e}(r)$ on the right. The correlation between the evolution of these quantities is apparent, as discussed in particular in Section 6.5. Further figures about the time evolution of the galaxy properties are shown and discussed in Paper, together with the final values (at the end of the simulation) of the total cold gas mass, mass of new stars formed, and accreted BH mass.

of the galaxy mass and of the degree of internal rotation, comparing the behaviour of the galaxy models on the basis of their different initial M_*, and decomposition parameter k, as mentioned above. Some evolutionary trends for the six rotating galaxy models analysed are shown in Figure 6.5 to support the results, while full discussions, more quantitative results, and more figures, can be found in Paper.

As a first global consideration, we confirm the picture that the evolution of the ISM undergoes recurrent cycles, during which the gas cools, falls towards the central galactic regions, and - if it possesses angular momentum - accumulates in a central disc. Indeed, with the exception of non rotating models, in all the six rotating models, cold gaseous discs of HI form in the equatorial plane, as consequence of gas cooling in the assumption of angular momentum conservation. Then, the cold gaseous disc becomes over-dense and self-gravitating, and develop Toomre instabilities, allowing for local bursts of star formation[5], and mass inflow from the disc towards the central supermassive BH, with consequent SNII and AGN feedback in the galaxy.

In Fig. 6.5, from top to bottom, the evolution of the gaseous disc mass $M_{\rm dHI}$, the stellar disc mass $\dot{M}_*$, and the BH accretion rate $\dot{M}_{\rm BH}$, are shown, and their interplay is apparent from the correlation between their trends. We found that the mass and size of HI disc increase for increasing galaxy mass and amount of rotational support. The BH accretion rate and the total BH accreted mass, as well, increase with galaxy mass, meaning that the central supermassive BHs accrete more material, and more efficiently, in more massive galaxies. Moreover, the efficiency of accretion increase with increasing galaxy rotation. This is not so obvious, since in more rotating galaxies the gas falls onto the equatorial plane at larger distances from the centre (as shown in Figs. 6.3 and 6.4, and discussed in Section 6.4). However, more rotating discs in galaxies of same structure (i.e. same initial M_*) turn out to have lower gas surface density, due to the larger size. This implies more Toomre instabilities in faster rotators, leading to more BH accretion and more star formation, despite the stronger centrifugal barrier. Overall, the larger BH mass accreted in fast rotators is due to fewer instability events in the disc, characterised though by significantly larger mass accretion. Analogously, faster rotators produce larger and more massive discs of newly formed stars in the equatorial plane[6], as visible in Fig. 6.5.

For completeness, albeit less discussed in this Chapter, we briefly summarise also the evolutionary X-ray properties of the hot gas, as functions of the galaxy properties. More massive galaxies are more X-ray luminous and hotter, in agreement with expectations from the Faber-Jackson relation (Faber and Jackson, 1976), and with values in the observed ranges. Moreover, more rotating galaxies of same structure are found at a lower luminosity, confirming that rotation tends to reduce the X-ray luminosity of galaxies, due to the strong tendency of rotating flows to induce gas cooling. Indeed, more rotating models present a larger amount of cold gas, and coherently a smaller amount of hot gas, and so they are less X-ray luminous and with lower hot gas temperature.

6.6 Effect of galaxy flattening on the gas flows

In Section 6.4, we described the expected behaviour of gas flows driven by angular momentum conservation, and neglecting viscosity effects, in relation to the rotational sup-

---

[5] Two different channels are considered for star formation: the classical one based on the cooling and the Jeans collapse times of the ISM, and a second one based on the assumption that the rotating gaseous disc self-regulates due to Toomre instabilities around a value of the Toomre parameter of $Q \simeq 1$ (Toomre, 1964).

[6] We stress that, from the stellar formation prescription in G19a, the star formation is not limited to the equatorial disc; however in the simulations almost all the star formation takes place in the gaseous disc. A top heavy IMF is adopted, and the massive stars inject energy in the ISM via SNII explosions, i.e. SNII feedback.

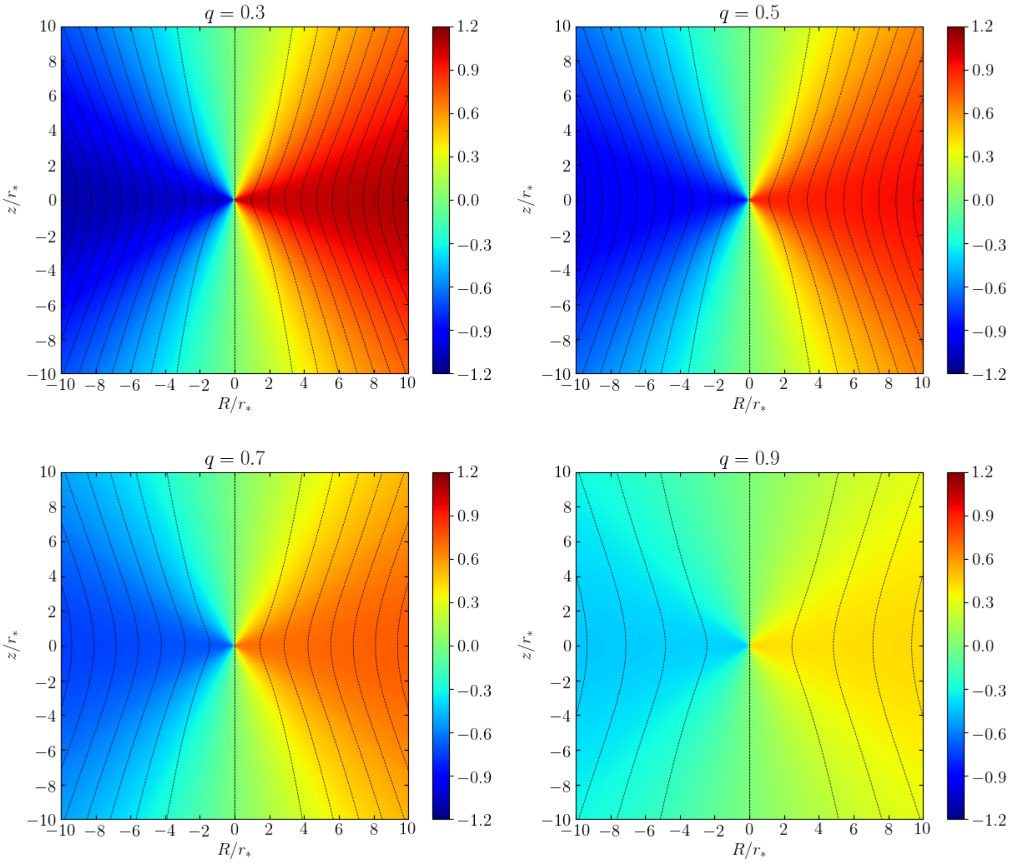

Figure 6.6: Maps of stellar rotational velocity v_φ, for the isotropic rotator, for $q_* = 0.3$, 0.5, 0.7, 0.9, in units of $\sqrt{\phi_\mathrm{n}} = \sqrt{GM_*/r_*}$. The galaxy models are discussed in Section 6.6. The dotted lines represent surfaces of constant angular momentum per unit mass, J_z, of the stellar component. See Fig. 6.3 for the explanation of the fall of the cooling gas onto the equatorial plane, with reference also to the next Fig. 6.7.

port of a flattened galaxy model. In particular, we analysed the model with $q_* = 0.7$ described in Section 6.2, for the three cases of Satoh kinematical decomposition $k = 1, k_\mathrm{a}(r), k_\mathrm{e}(r)$ of eq. (6.10). For the isotropic and the exponential cases, the evolution has been studied through numerical simulations, and some results are discussed in the previous Section. We extend here the investigation to different degrees of flattening of the galaxy models: along the same lines of Section 6.4, now we analyse the effect of the flattening on gas inflows for isotropic rotators, both more and less flattened with respect to the already studied case of $q_* = 0.7$.

We recall that the formulae for the stellar component of the models used for the simulations are given in homoeoidal expansion, which imposes a limit in the flattening of the ellipsoidal density distribution of $q_* \geq 2/3$ (see Section 4.3, and e.g. CMPZ21 for details). Thus the models studied in this Section are built with JASMINE2, as *true* ellip-

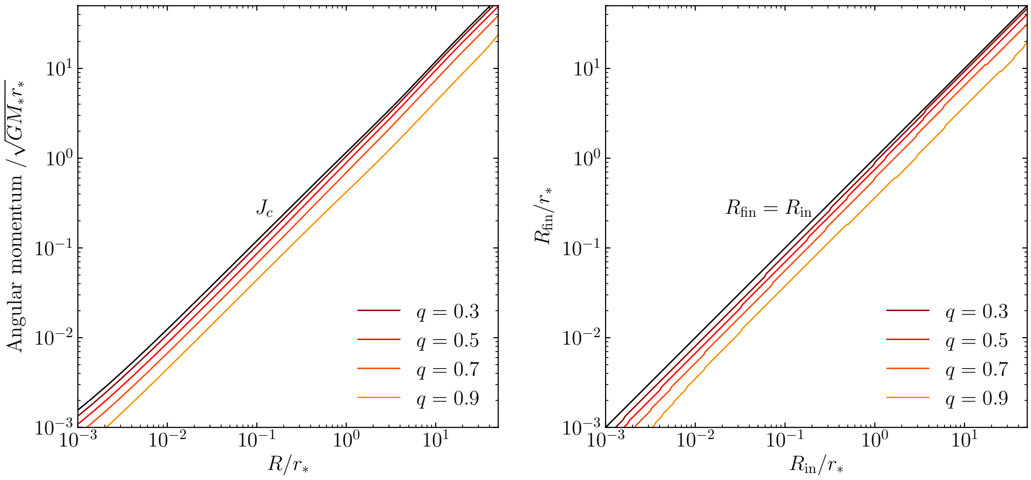

Figure 6.7: Analogous to Fig. 6.4, for the isotropic rotator, with different degrees of flattening (as reported in the plot), as discussed in Section 6.6. See Fig. 6.4 for the explanation of the movement of gas in the equatorial plane, from $R_{\rm in}$ to $R_{\rm fin}$. Clearly, in less flattened models (and less rotating, see the previous Fig. 6.6), gas reaching the equatorial plane at the same $R_{\rm in}$ moves towards more central $R_{\rm fin}$.

soids (not homoeoidally expanded), with numerical evaluation of the potentials (through the Chandrasekhar integral formula, from eqs. 4.27 and 4.30), and numerical solutions of the Jeans equations (see Section 4.3 for a detailed discussion of the difference between homoeoidally expanded and numerical results). In this way, we have no limits in the choice of the flattening degree of the ellipsoidal stellar density distribution, and we can study also very flattened systems. We build galaxy models following the prescription of Sections 6.2 and 6.3.2 (except for the homoeoidal approximation) with $q_* = 0.3$, 0.5, 0.7, 0.9, and Satoh parameter $k = 1$. The two extreme values of q_* represent a quite flat E7 galaxy and an almost spherical E1 galaxy; the case $q_* = 0.7$ is the not-expanded counterpart of the isotropic rotator studied in the previous Sections, so that we use it as reference for the more and less flattened cases.

In Fig. 6.6, the maps of stellar rotational velocity v_φ and the surfaces of constant angular momentum J_z are shown, in analogy with Fig. 6.3. The same colorbar has been used for the four models to highlight that more flattened models rotate faster, with the same pattern of rotation, typical of a *regular rotator* such as the isotropic one. The curves of constant J_z, from a position (R, z) and reaching the equatorial plane $(z = 0)$, are slightly more inclined towards the centre for increasing flattening, i.e. for increasing rotation in the plane. They are almost vertical for the almost spherical case ($q_* = 0.9$, lower right plot); indeed, as the spatial gradient of v_φ decreases, J_z depends more and more only on the radius R, by definition, and so the surfaces of constant J_z tend to become stratified on cylinders. However, the radius $R_{\rm in}$ in the equatorial plane reached by gas coming from a position (R, z) does not vary strongly with the flattening of the system, as visible in Fig. 6.6. From Fig. 6.7, analogous to Fig. 6.3 discussed in Section 6.4, we see that in less flattened (and less rotating) models, the gas moves in the equatorial plane more inwards, reaching more central $R_{\rm fin}$, while in more flattened models the movement is less significant, and $R_{\rm fin}$ turns out to be nearer to $R_{\rm in}$.

Without fixing the total initial stellar mass and size of the galaxy models, and without running the simulations, it is not possible of course to predict the evolution of the gas flows in the whole galaxy, neither the amount of gas involved, and neither by consequence the effect on the BH accretion and the star formation. Nevertheless, from what learnt from the present study of the gas flows onto the equatorial plane, and the inflows towards the centre of the galaxy, we can say that more flattened models tend to form more extended gaseous discs. This is in agreement with what found in Sections 6.4 and 6.5, since more flattened models are also faster rotators, and we found that the size of gaseous equatorial discs correlates with the rotational support of the models.

6.7 Summary

We applied the code JASMINE2 to the study of galaxy models suitable for hydrodynamical simulations of galaxy evolution. In particular, the effect on the stellar dynamics of an extended group/cluster DM distribution has been analysed, and different parametrisations of the Satoh parameter k have been considered. Then, we discussed the expected behaviour of gas inflows towards the centre of the galaxies, as predicted through the assumption that the gas falls into the equatorial plane following the rotation field of stars, and preserving its angular momentum. The run of hydrodynamical simulations for a set of galaxy models, with different total stellar mass and different rotational support, confirmed the predictions and naturally extended the analysis.

Chapter 7

Conclusions

The work presented in this Thesis is addressed at building dynamical models of multicomponent stellar systems as flexible and rigorous as possible, in order to study the properties of galaxies in relation to the complexity of their internal structure and dynamics. For instance, the observable stellar morphological and kinematical features depend of course on the amount and distribution of the stellar and DM components, and on the properties of the stellar populations. On the basis of the history of formation and evolution of the whole system, galaxies are composed by stellar populations characterised by different age, metallicity, IMF, with higher or lower streaming velocities, and more or less anisotropic orbits; these populations are also structurally distinct, belonging for example to an extended halo, a main disc, a central bulge or bar, a nuclear stellar disc or star cluster. A sophisticated modelling of the internal structure and of the stellar dynamics of galaxies is crucial not only to understand observed features of real galaxies, but also to produce realistic galaxy models to study the initial conditions for hydrodynamical and N-body simulations of galaxy evolution.

7.1 Summary and conclusions

We summarise the main results achieved in this Thesis, and we mention some ongoing and future applications.

Modelling procedure and JASMINE2

Theoretical framework We developed a theoretical framework to model (and project along a given line-of-sight) the internal structure and stellar dynamics of multicomponent axisymmetric galaxies in equilibrium, with an arbitrary number of stellar and DM components, and a central BH; the models are based on the solution of the Jeans equations for the stellar dynamics. The numerical applicability is illustrated as an efficient and easily reproducible modelling procedure, which in particular we implemented in, and tested with, the ad hoc numerical code JASMINE2, developed as part of the PhD project. In our approach, we reproduce realistic galaxy properties, and we can build large samples of galaxy models, thanks to a dynamical modelling procedure allowing to control the internal structure and dynamics of each stellar component. For this purpose, we consider a number of stellar components, representing a stellar population, and described by a specific distribution function (DF). In fact, the underlying DF is unknown, and we only verify some consistency arguments based on the positivity of the mass density and on the positivity of second-order velocity moments; instead, we define each stellar distribution through its density profile. The total stellar distribution is implicitly described by a DF which is given by the sum of the DFs of the stellar components; from this fundamental identity, we derived the sum rules of the structural properties and of the velocity moments, and consequently of the projected fields, allowing to calculate the total internal and projected fields once they are obtained for the single stellar components. This procedure can be easily applied to the construction of stellar systems by difference of stellar components, which can be very for instance when interested in setting the total stellar distribution. Moreover, for each stellar component we assume a possibly different constant mass-to-light ratio, so that the total mass-to-light ratio is in general position-dependent, and the total internal and projected dynamical quantities can be calculated as mass-weighted or luminosity-weighted sums of the components.

Anisotropy and kinematical decomposition In the assumption of axisymmetry, each DF is assumed to depend on two integrals of motions, producing stellar systems with only tangential anisotropy of the velocity dispersion tensor, and rotating only around the symmetry axis. This assumption is also generalised to stellar systems fully anisotropic, which do not depend on two integrals, following Cappellari (2008). Once the solution of the Jeans equations is obtained for a stellar component in the total gravitational potential, a further assumption is necessary to split the total azimuthal velocity in ordered velocity and velocity dispersion: besides well-known kinematical decompositions, we presented a generalisation of the Satoh k-decomposition, which can be applied when the Satoh decomposition cannot be used, a not uncommon case in multicomponent systems, as we have shown in some applications.

Numerical aspects

Two main bottlenecks in the numerical implementation In a numerical implementation of the multicomponent modelling technique presented, two main slowdown factors are encountered, meaning the time-expensive numerical evaluation of the gravitational potentials, and the large number of model parameters. Indeed, for each stellar and DM density component, the gravitational potential is determined by the solution of the Poisson equation; only for few simpler density models, an analytical expression for the associated potential is known, so that in most cases a numerical computation is required. For any axisymmetric density distribution, the numerical computation of the potential can be performed in terms of complete elliptic integrals, implying a very accurate but quite time-expensive 2D integration for each position of the 2D numerical grid. The computational time increases naturally for increasing number of density components, and for increasing numerical resolution, so that an extensive exploration of the model parameter space, which can be very large for multicomponent models, would be impossible. To reduce the computational time, and allow for a fast and flexible models construction, on one side, we proposed faster methods for the evaluation of the potentials, and on the other side, we fully exploited the scalings allowed by the Poisson and the Jeans equations, and by the projection formulae.

Scaling approach The scaling approach, which we implemented in the numerical code JASMINE2, is proposed as a general numerical scheme that can be implemented as well in similar codes. The scheme leads to an organisation of the code in two logically distinct parts, which we called Potential and Jeans Solver and Post-Processing (PP). In practice, once the structural properties of the scaled (dimensionless) stellar and DM distributions are assigned, the code computes, with a single run of the Potential and Jeans Solver, the scaled solutions of the Jeans equations, for each stellar component in each potential component, defining a family of models. The scaled Jeans solutions are then combined in PP, with the desired mass and luminosity weights, and the choice of appropriate kinematical decompositions, and then projected along a given line-of-sight. The PP procedure can be rapidly performed several times, obtaining different specific models in the same family. Finally, for each model, the two physical scales M_* and r_*, to which all the masses and lengths are respectively normalised, can be assigned, obtaining the final scaling of the whole system. A further benefit of this approach is the possibility to gain a full understanding of the role of each density component in determining the resulting total galaxy properties, including for instance the kinetic and gravitational energies of the systems, and the observable quantities entering the Fundamental Plane.

Fast methods for the evaluation of the potentials Besides the scaling operations, a second expedient reduces the computational time with respect to what required by the computation of the potentials in terms of elliptic integrals. We suggested the use of the Chandrasekhar integral formula for ellipsoidal distributions, and of an integral formula based on Bessel functions for factorised disc distributions. Both methods only require a very fast 1D integration, and we showed that the accuracy reached is the same provided by the elliptic integrals. The so-called Chandrasekhar formula is a classic method, involving two integrations: one can be solved analytically for many axisymmetric distributions, and in particular for all the spheroidal density models of the library included in JASMINE2. Also integral formulae based on Bessel functions are well known; however, we presented a general formula using the Bessel function J_0, allowing for a fast 1D integration when applied to factorised discs in cylindrical coordinates for which the two integrals over R and z have analytical solutions. This is obtained for several radial and vertical distributions, which can be combined to produce a variety of thin and thick discs, beyond the simplest approximation of zero-thickness. In particular, the radial term is represented by the Hankel transform of the radial density distribution, which is known for many commonly used models. For the vertical stratification, the solution for the exponential distribution is obtained, recasting a well-known result, and the infinitely-thin case is simply given as a limit case; more importantly, we offered the solution also for the so-called pseudo-isothermal sheet, with vertical density profile proportional to sech^n, which is often used as well to model stellar and gaseous galactic discs. Summarising, for many ellipsoidal systems and factorised discs, and especially for all the density models of the library implemented in JASMINE2 (which do not have analytical potential), we are able to calculate the potential with a fast numerical integration, reducing the computational time from many hours to few minutes, or even few seconds, with respect to the standard integration using elliptic integrals.

Reliability of the homoeoidal approximation We exploited the numerical solutions of the Jeans equations for σ and $\sqrt{\Delta}$, obtained with JASMINE2, to test the reliability of homoeoidally-expanded formulae for increasing degree of flattening of the ellipsoidal density distributions. For Jaffe models, as examples, we proved that the numerical solution for σ obtained for an homoeoidally-expanded density-potential pair, with respect to the true ellipsoidal density distribution with numerical potential, diverges only up to few percent for $q = 0.7$, i.e. approaching the limit flattening allowed in homoeoidal approximation; $\sqrt{\Delta}$ instead diverges up to about 20%. Thus more care is needed in this latter case, recalling also that from $\sqrt{\Delta}$ we calculate the stellar rotational field with the Satoh k-decomposition. In addition, we showed that the use of pure analytical homoeoidally-expanded σ and $\sqrt{\Delta}$, i.e. neglecting second-order terms in the flattening, does not increase significantly the discrepancies discussed above.

Applications

Three illustrative galaxy models In order to illustrate the features of the modelling procedure presented, and to show the effect of the different matter components on the total galaxy properties, we built and discussed three illustrative galaxy models - named JJE, JHD, and JLD -, composed of two stellar components, a DM halo, and a central BH. The JJE model represents a spherical galaxy, and it has been used to force the models construction to obtain a stellar density component by difference of assigned density distributions. Then it offered the opportunity to apply the generalised Satoh decomposition to the difference component, after assuring the consistency of the underlying DF, at least up to second-order velocity moments. The JHD and JLD are built as quite realistic models of ETGs including a stellar disc embedded in a stellar halo: the JHD model may represent a disc galaxy, with a large, massive and rotating disc, and a surrounding stellar halo, less massive and populated by older stars, with more anisotropic orbits; the JLD model, instead, may represent a so-called slow rotator with evidence of a small inner counter-rotating disc. We studied the effect on the internal and projected dynamics of the mass and luminosity weights of the components. For instance, the younger stellar component (with lower mass-to-light ratio) may dominate the total dynamical fields, at least in some regions of the galaxy, even if less massive, as expected. Moreover, different values of mass-to-light ratio for the components produce gradients of total mass-to-light ratio, in agreement with what observed in ETGs.

3MN fit of a double-exponential disc We explored the accuracy of one of the 3MN decompositions proposed by Smith et al. (2015) to reproduce the morphological and kinematical fields of double-exponential discs. Firstly, we confirmed the excellent agreement of the rotation curves of the two models in the equatorial plane, at least out to $\sim 10R_{\rm d}$, and the good agreement of the FO and EO surface brightness near the centre, while they start to significantly diverge at few R_d; especially the EO projections are different off-plane, due to the rounder shape of the MN distributions. Then, we extended the analysis to the solution of the Jeans equations, and to the projected kinematical fields. We found that the EO v_los tends to be larger for the double-exponential disc than for its 3MN representation, but overall the agreement is rather good, even outside the equatorial plane. A different situation is found for the EO σ_los: the values are significantly larger in the 3MN model, which also presents a characteristic hourglass-shaped vertical distribution. Some care is thus recommended when using a 3MN decomposition to infer the properties of observed disc galaxies. Furthermore, we recall that with a fast and precise evaluation of the potential produced by the double-exponential disc, as possible with the method presented based on Bessel functions, it is not necessary (at least in many applications) to resort to less realistic disc models (although with analytical potentials), and to the use of tailored combinations of such models.

Internal dynamics and gas flows in ETGs Finally, we carried out an exploration of the parameter space for a family of galaxy models, representing oblate and rotating massive ETGs, with the aim of investigating the evolution of gas flows, by means of hydrodynamical simulations, as functions of structural and dynamical galaxy properties. The galaxy models are composed of an oblate stellar component, a DM halo, and a central supermassive BH, with the addition of a DM distribution taking into account the effect of an hosting galaxy group/cluster. The stellar dynamical fields are included in the simulations, in a convenient way via analytical formulae in homoeoidal approximation, which however limited the analysis with respect to two main points: it is not possible to include the effect of group/cluster DM halo on the stellar dynamics, and to consider very flattened stellar systems, making helpful the application of the code JASMINE2 in two main directions. On one side, we studied the total dynamical fields, to assure the construction of a group/cluster DM halo which did not affect the stellar dynamics in the inner regions, and which produced a flat rotation curve in the outer regions. On the other side, we made predictions on the behaviour of the gas falling on the equatorial plane, and then infalling towards the centre of the galaxy, for a set of galaxy models with different degree of flattening and different rotational support, Overall, more flattened and rotating systems tend to form more extended discs of cold gas on the equatorial plane. For some of these models, with different total stellar mass and size, and different rotational support, but same flattening, hydrodynamical simulations have been run, also confirming the predictions. Furthermore, the time evolution of some galaxy properties are discussed in details in Ciotti et al. (2022), leading to the construction of galaxies with global properties in agreement with observations.

7.2 Ongoing work: the global stability of disc galaxies

This study arises from a recent collaboration with Elena D'Onghia, and it is presented here in its starting idea, as an ongoing application of the modelling approach and numerical code presented in this Thesis, with the support of N-body simulations.

Caravita C., D'Onghia E., Ciotti L., Pellegrini S., In preparation

We extend our study, mainly focused so far on ETGs, to the analysis of disc galaxies which can develop global instabilities on the stellar disc, leading to the formation of non-axisymmetric features, such as a bar in the inner regions. Often spiral galaxies host a bar, and are classified as *barred* galaxies.

The formation and evolution of the bar is an open research field, addressed by means of N-body simulations since the early 1970s (e.g. Hohl, 1971; Ostriker and Peebles, 1973). Some criteria have been studied to understand the conditions for the development of global instabilities in the stellar disc leading to bar formation, but a universal agreement is not found. Our intent is to find a global stability parameter which is a good diagnostic for the development of future instabilities.

The most common global stability parameter, due to Ostriker and Peebles (1973), is

$$t = \frac{T}{|U|}, \tag{7.1}$$

where T is the ordered kinetic energy of the system (see eq. A.13 and eq. A.34), and U is the total gravitational energy, calculated from the potential of the whole system (eq. A.17). In particular, it is stated that discs become certainly unstable to bar formation for an initial value of $t < 0.14$. It is well recognised, indeed, that the stellar rotation of the disc itself enhances the growth of instabilities, while the presence of an additional matter distribution, such as a DM halo, a central bulge, or a central BH, tends to stabilise the disc. However, while the parameter t may predict in a quite satisfactory way the development of disc instabilities in certain cases, it may fail in some other situations.

We briefly discuss the main limits, which are partially discussed also, for example, in Sellwood (1983). First, the parameter t cannot be used to take into account the effect of a central point-mass, such as the central BH, which would produce a divergent denominator for an arbitrarily small central mass: the resulting zero t regardless to any other model parameter, indeed, could not give any useful prediction. Second, in the opposite case, t can be misleading even in case of an extended mass distribution, such as a spherical DM halo extended far beyond the stellar disc: the amount of mass outside the disc cannot affect the stellar dynamics, since it produces a null gravitational force inside (from the *Newton's Theorem*); however, since U depends on the potential, an arbitrarily large mass distributed outside the disc produces an arbitrarily small t, without actually affecting the stability of the disc.

Addressing the points above, an alternative global stability parameter has been proposed by Efstathiou et al. (1982), as

$$t^* = \frac{T_*}{|W_*|}, \tag{7.2}$$

where now T_* is by definition the stellar order kinetic energy (see eq. 2.20), and W_* is the trace of the gravitational interaction energy tensor (eq. A.16), of the stars in the total potential (eq. 2.22). Thus t^* involves the forces instead of the potentials, and it does not take into account the self-interaction energy of an external matter distribution, in contrast with the parameter t.

We are analysing the behaviour of the two global stability parameters t and t^*, as functions of structural and dynamical galaxy properties, and investigating in depth their limits and merits, through an exploration of the model parameter space with JASMINE2, and through N-body simulations performed with the numerical code GADGET (Springel et al., 2005). For a sample of interesting galaxy models, selected also on the basis of the more critical situations discussed above, we are running the simulations. We aim at understanding the relation between the initial model parameters and the successive development of instabilities, with respect to bar formation, and at establishing which parameter provides a stronger stability criterion, able to distinguish between models which remain stable during many Gyr of evolution, and models which develop clear features of a central bar within few Gyr.

The first galaxy models we are studying are built following Springel et al. (2005), and they are composed of a stellar disc and an external halo. The disc is modelled by a pseudo-isothermal exponential density distribution (eq. 4.22), whose associated potential is computed in terms of Bessel functions from eq. (4.50) (with eqs. D.2 and 4.62); the halo is modelled by an Hernquist density profile (eq. 4.1), with analytical potential in the spherical case (eq. 4.2), or otherwise numerical potential calculated with the Chandrasekhar formula in eq. (4.27) (with eq. 4.30). The stellar azimuthal motions are determined in epicyclic approximation (Section 2.3.3). As a check between the different numerical codes, we found a remarkable agreement between the circular velocity, the rotational velocity and the velocity dispersion profiles produced by JASMINE2, and independently produced as initial conditions of the simulations of GADGET. With suitable choices of the parameters, the halo may be intended as an extended DM distribution, or an inner stellar bulge. We are studying the values of the global stability parameters, t and t^*, for a large sample of galaxy models, varying the halo-to-stellar mass ratio, the halo-to-stellar scale-radius ratio, the amount of rotational support of the stellar disc.

7.3 Future applications

Dynamical models of galaxies are a powerful tool to study galaxy properties and to understand galaxy formation and evolution.

- An application field is naturally represented by the reproduction and interpretation of observed features, especially accounting for the quantity and quality of data provided by Integral Field Spectroscopy, and exploiting the ability of a numerical code like JASMINE2 in modelling multiple stellar components, and complex kinematical structures.

- A future perspective of application of JASMINE2, and of its scaling approach, is a systematic exploration of galaxy models constrained to lie on the empirical Scaling Laws, and the Fundamental Plane in particular for ETGs, extending the statistical approach pioneered in Bertin et al. (2002) and Lanzoni and Ciotti (2003). The possibility to flexibly vary in Post-Processing the mass-weights of all the matter components, and the luminosity weights and rotational supports of the stellar components, and moreover to vary further the total stellar mass and size, can be very convenient to identify the models satisfying some Scaling Relations.

- From the point of view of numerical simulations of galaxy evolution, we have seen that dynamical models can provide the stellar dynamical fields necessary to implement the hydrodynamical equations. Further investigations can be performed, based on the construction of different galaxy models, on the exploration of different model parameters, or after the implementation of new features in simulations.

- The evolution of stellar systems is studied also by means of N-body simulations, and also in this case a numerical code like JASMINE2 allows to study the properties of galaxy models for which one is interested in running the simulations, and to calculate the initial conditions. At this regard, in the previous Section, we have briefly introduced an ongoing study on the stability of galactic discs, with the aid of N-body simulations.

Appendix A

Jeans equations and Virial theorem

We show some considerations about astrophysical gravitational systems and their stellar dynamics. First, we briefly recall the validity of the assumption of non-collisionality of galaxies, and we define the *distribution function* (DF) of stars over the phase-space. Then we derive some fundamental dynamical properties, as velocity moments of the DF over the velocity space, and the energies of the systems. In the assumption of non-collisionality, the DF of stars satisfies the *Collisionless Boltzmann Equation* (CBE). We apply the *method of moments* to derive simpler differential equations: the *Jeans Equations* are obtained through the velocity moments of the CBE over the velocity space. In turn, through the configuration moments of the Jeans equations over the configuration space, we verify the *Tensor Virial Theorem*, and consequently its scalar formulation. Finally, we derive the Jeans equations and the scalar Virial Theorem in case of stationary and axisymmetric stellar systems, which are the objects of interest of this Thesis work.

This Appendix does not claim to be exhaustive on the topic, but to create the necessary background for the issues faced in this dissertation. For a much more extended view on the topic, and on stellar dynamics in general, see e.g. Binney and Tremaine (2008), Ciotti (2021).

We stress that here we refer to a generic single stellar component, but what we discuss is valid also for each stellar component of a multicomponent system, adapting to galaxy models presented in this Thesis. In this regard, the subscript used here, e.g. ij, refer to the tensorial nature of a quantity, and not to i-th stellar components and j-th potential components.

A.1 Non-collisionality and distribution function

In stellar systems, the orbits of stars are determined by the gravitational interactions with the stars themselves, generic DM particles, and a central massive BH if present; while the gravitational effect of the gaseous component on stellar orbits can be neglected. For an exact investigation of the stellar dynamics, these systems should be treated as *N-body problems*, in which each encounter with a nearby star, DM particle and black hole, changes the position and the velocity of each star, i.e. its coordinates in the phase-space $\gamma = (\mathbf{x}, \mathbf{v})$. Nevertheless, the time scale employed by a system to experience significant variations in its dynamics through the sum of individual encounters, the 2-body relaxation time, t_{relax}, can be even longer than the age of the system itself. In this case, 2-body collisions are negligible, and the stellar system can be considered *collisionless*; otherwise, 2-body collisions are important in determining the stellar dynamics, and the system has to be treated as *collisional.* For illustrative purposes, we set for a moment on the simple and idealised case of a self-gravitating finite stellar system of N particles, with generic size R and stellar speed σ. The characteristic time needed by a star to cross the system is the crossing time $t_{\text{cross}} \sim R/\sigma$, and it is proved that approximately

$$t_{\text{relax}} \sim \frac{0.1\,N}{\ln N}\, t_{\text{cross}}. \tag{A.1}$$

Note that t_{relax} increases of course with increasing t_{cross}, but also with increasing N, although less intuitively. For example, for a typical galaxy with $N \sim 10^{11}$ and $t_{\text{cross}} \sim 10^8$, it results $t_{\text{relax}} \sim 10^7$Gyr, a time scale even greater than the age of the Universe; therefore, it is effectively significant the study of the galactic dynamics in the approximation of non-collisionality. In contrast, stellar systems such as globular clusters, with characteristic $N \sim 10^{5-6}$ and $t_{\text{cross}} \sim 10^6$, have $t_{\text{relax}} \sim 1 - 10$Gyr, a time scale comparable to their age, thus they are weakly collisional. Strongly collisional systems are instead open clusters, with characteristic $N \sim 10^{2-3}$ and $t_{\text{cross}} \sim 10^6$, and so $t_{\text{relax}} \sim 10^{6-7}$yr.

In the assumption of non-collisionality, we replace the real discrete distribution of N stars with a continuous mass density distribution $\rho(\mathbf{x}; t)$; the gravitational potential associated derives from the Poisson equation $\nabla^2\phi = 4\pi G\rho$, so that

$$\phi(\mathbf{x}; t) = -G \int_{\Re^3} \frac{\rho(\boldsymbol{\xi}; t) d^3\boldsymbol{\xi}}{||\mathbf{x} - \boldsymbol{\xi}||}. \tag{A.2}$$

The distribution of stars in the phase-space, i.e. the space of configurations and velocities, at any time, is described by the so-called *distribution function* (DF) $f(\mathbf{x}, \mathbf{v}; t)$: a nowhere negative function, which represents the stellar mass density in a volume element of the phase-space $\mathrm{d}^3\mathbf{x} d^3\mathbf{v}$, at a given time t. Just to clarify between different definitions in literature, we are adopting the same definition as in Ciotti (2021), while in Binney and Tremaine (1987) it is defined as a numerical density and in Binney and Tremaine (2008) as a probability density. So the stellar mass density distribution of the system, at position $\mathbf{x}$ and at time t, is given by

$$\rho(\mathbf{x}; t) = \int_{\Re^3} f(\mathbf{x}, \mathbf{v}; t) d^3\mathbf{v} \tag{A.3}$$

and the total stellar mass is

$$M = \int_{\Re^6} f(\mathbf{x}, \mathbf{v}; t)\, \mathrm{d}^3\mathbf{x} d^3\mathbf{v}. \tag{A.4}$$

Before introducing some relevant properties of stellar systems, we consider a generic physical property of stars, defined over the phase-space, $F(\mathbf{x}, \mathbf{v}; t)$, and we define its average over the velocity space weighted for the DF as

$$\bar{F}(\mathbf{x}; t) = \frac{1}{\rho(\mathbf{x}; t)} \int_{\Re^3} F(\mathbf{x}, \mathbf{v}; t) f(\mathbf{x}, \mathbf{v}; t) d^3\mathbf{v}. \tag{A.5}$$

We then define, as *velocity moments* of the DF over the velocity space, this operation when F is given by the velocity coordinates. Immediately, the zero-order velocity moment gives eq. (A.3). The first-order moment is

$$\overline{\mathrm{v}_i}(\mathbf{x}; t) = \frac{1}{\rho} \int_{\Re^3} \mathrm{v}_i f d^3\mathbf{v} \tag{A.6}$$

and the second-order moments are

$$\overline{\mathrm{v}_i \mathrm{v}_j}(\mathbf{x}; t) = \frac{1}{\rho} \int_{\Re^3} \mathrm{v}_i \mathrm{v}_j f d^3\mathbf{v}, \tag{A.7}$$

$$\begin{aligned} \sigma^2_{ij}(\mathbf{x}; t) &= \overline{\mathrm{v}_i \mathrm{v}_j} - \overline{\mathrm{v}_i}\,\overline{\mathrm{v}_j} = \overline{(\mathrm{v}_i - \overline{\mathrm{v}_i})(\mathrm{v}_j - \overline{\mathrm{v}_j})} = \\ &= \frac{1}{\rho} \int_{\Re^3} (\mathrm{v}_i - \overline{\mathrm{v}_i})(\mathrm{v}_j - \overline{\mathrm{v}_j}) f d^3\mathbf{v}, \end{aligned} \tag{A.8}$$

for $i, j = 1, 2, 3$, where $\overline{\mathrm{v}_i}$ is the i-th component of the streaming velocity, and σ^2_{ij} is the velocity dispersion tensor, representing the mean dispersion from the mean (streaming) velocity of stars. It is a symmetric tensor, so in a reference system in which it can be written in the diagonal form (e.g. the cylindrical coordinates system, as we will see later), the only non-zero components are $\sigma^2_{ii} = \overline{\mathrm{v}^2_i} - \overline{\mathrm{v}_i}^2$. Its geometrical interpretation as *velocity dispersion ellipsoid* is useful when the anisotropy of the velocity dispersion tensor plays an important role in determining the galaxy morphology, as in slow-rotating elliptical galaxies. In each position and at any time, it is possible to define an ellipsoid, whose three semi-axis coincide with the three components of the diagonal tensor: if $\sigma^2_{ij}(\mathbf{x}; t) = \sigma^2(\mathbf{x}; t)\delta_{ij}\, \forall\, \mathbf{x}$, the velocity dispersion tensor is *isotropic*, and the velocity dispersion ellipsoid is everywhere a sphere; otherwise σ^2_{ij} is *anisotropic*.

We see now other essential second-order tensors, obtained as moments over the configuration space, by integrating the quantities above. First, we define the mass tensor

$$I_{ij}(t) = \int_{\Re^3} \rho x_i x_j\, \mathrm{d}^3\mathbf{x}, \tag{A.9}$$

whose trace is $\mathrm{Tr}(I_{ij}) = I(t)$. The kinetic energy of the system is described by the total, streaming, and velocity dispersion kinetic energy tensors, respectively,

$$K_{ij}(t) = \frac{1}{2} \int_{\Re^3} \rho \overline{\mathrm{v}_i \mathrm{v}_j}\, \mathrm{d}^3\mathbf{x}, \tag{A.10}$$

$$T_{ij}(t) = \frac{1}{2}\int_{\Re^3} \rho \overline{\mathrm{v}_i}\,\overline{\mathrm{v}_j}\,\mathrm{d}^3\mathbf{x}, \tag{A.11}$$

$$\Pi_{ij}(t) = \int_{\Re^3} \rho \sigma^2_{ij}\,\mathrm{d}^3\mathbf{x}, \tag{A.12}$$

with traces

$$K(t) = \frac{1}{2}\int_{\Re^3} \rho \overline{\mathrm{v}^2}\,\mathrm{d}^3\mathbf{x}, \qquad T(t) = \frac{1}{2}\int_{\Re^3} \rho \bar{\mathrm{v}}^2\,\mathrm{d}^3\mathbf{x}, \qquad \Pi(t) = \int_{\Re^3} \rho \sigma^2\,\mathrm{d}^3\mathbf{x}, \tag{A.13}$$

where $\overline{\mathrm{v}^2}$, $\bar{\mathrm{v}}^2$, σ^2 are the total velocities, sums of the diagonal terms of the related tensors. Of course it holds

$$K_{ij} = T_{ij} + \frac{\Pi_{ij}}{2}, \qquad K = T + \frac{\Pi}{2}. \tag{A.14}$$

The gravitational interaction energy tensor between a density distribution ρ and a generic gravitational potential Φ is defined as

$$W_{ij}(t) = -\int_{\Re^3} \rho x_i \frac{\partial\Phi}{\partial x_j}\,\mathrm{d}^3\mathbf{x}. \tag{A.15}$$

Its trace is

$$W(t) = -\int_{\Re^3} \rho < \mathbf{x}, \nabla\Phi > \,\mathrm{d}^3\mathbf{x}, \tag{A.16}$$

where $<,>$ indicates the scalar product. If the potential Φ is produced by the density ρ only (eq. A.2), then W represents the self-gravity of the system; otherwise, Φ may indicate an *external* potential with respect to ρ, i.e. produced by a different density distribution (such as dark matter or gaseous components, other stellar components, a central black hole) or a *total* potential in which ρ is embedded, given by the superposition of the potential produced by ρ and those produced by other density distributions. At variance with the tensors of eqs. (A.9)–(A.12), which are always positive, W_{ij} is always negative. We recall also that the total energy of the system is given by $E = K + W$. It is useful to define the gravitational energy of the density ρ in the total potential Φ as the scalar quantity

$$U(t) = \frac{1}{2}\int_{\Re^3} \rho\Phi\,\mathrm{d}^3\mathbf{x}. \tag{A.17}$$

If otherwise Φ is an external potential with respect to ρ, then the gravitational energy becomes

$$U(t) = \int_{\Re^3} \rho\Phi\,\mathrm{d}^3\mathbf{x}. \tag{A.18}$$

This difference appears more clear, and its importance stands out, in the application to multicomponent systems (as we see in particular in Chapter 3 and we briefly introduce in Section 7.2). Obviously also U is always negative, and in particular in case of self-gravity it holds $U = W$ (from eqs. A.16 and A.17).

A.2 The Collisionless Boltzmann Equation

Although stellar systems are never exactly collisionless, we have seen that galaxies essentially are. Therefore, we describe the time evolution of the DF in the assumption of *perfectly collisionless regime*: the DF f satisfies the Collisionless Boltzmann Equation (CBE), so that

$$\frac{Df}{Dt} = \frac{\partial f}{\partial t} + \sum_{i=1}^{6} \frac{\partial (f\dot{w}_i)}{\partial w_i} = 0, \tag{A.19}$$

where w_i is the i-th coordinate of the phase space, i.e. $\mathbf{w} = (x_1, x_2, x_3, \mathrm{v}_1, \mathrm{v}_2, \mathrm{v}_3)$, and $\dot{w}_i = \partial w_i/\partial t$, reading

$$\begin{cases} \dot{x}_i = \mathrm{v}_i \\ \dot{\mathrm{v}}_i = -\dfrac{\partial \Phi}{\partial x_i}, \end{cases} \tag{A.20}$$

where Φ is the total gravitational potential. Then the CBE can also be written as

$$\frac{\partial f}{\partial t} + \mathrm{v}_i \frac{\partial f}{\partial x_i} - \frac{\partial \Phi}{\partial x_i}\frac{\partial f}{\partial \mathrm{v}_i} = 0, \tag{A.21}$$

where the Einstein summation convention (sum over repeated indices) is adopted.

Now we calculate the zero-order and first-order velocity moments of the CBE over the velocity space:

$$\int_{\Re^3} \left[\frac{\partial f}{\partial t} + \mathrm{v}_i \frac{\partial f}{\partial x_i} - \frac{\partial \Phi}{\partial x_i}\frac{\partial f}{\partial \mathrm{v}_i}\right] d^3\mathbf{v} = 0, \tag{A.22}$$

$$\int_{\Re^3} \mathrm{v}_j \left[\frac{\partial f}{\partial t} + \mathrm{v}_i \frac{\partial f}{\partial x_i} - \frac{\partial \Phi}{\partial x_i}\frac{\partial f}{\partial \mathrm{v}_i}\right] d^3\mathbf{v} = 0. \tag{A.23}$$

Through the definitions (A.3), and (A.6)–(A.8), a set of the so-called Jeans equations is derived,

$$\frac{\partial \rho}{\partial t} + \frac{\partial (\rho \overline{\mathrm{v}_i})}{\partial x_i} = 0, \tag{A.24}$$

$$\frac{\partial (\rho \overline{\mathrm{v}_j})}{\partial t} + \frac{\partial (\rho \overline{\mathrm{v}_i \mathrm{v}_j})}{\partial x_i} + \rho \frac{\partial \Phi}{\partial x_j} = 0, \tag{A.25}$$

where the latter can also be written in terms of σ_{ij} as

$$\rho \frac{\partial \overline{\mathrm{v}_j}}{\partial t} + \frac{\partial (\rho \sigma_{ij}^2)}{\partial x_i} + \rho \overline{\mathrm{v}_i} \frac{\partial \overline{\mathrm{v}_j}}{\partial x_i} + \rho \frac{\partial \Phi}{\partial x_j} = 0. \tag{A.26}$$

We stress the similarity between the two expressions of the Jeans equations for the stellar dynamics and the hydrodynamical equations of the mass conservation and the momentum conservation, respectively.

Then we calculate the first order configuration moment of the Jeans equations (A.25) over the configuration space, meaning

$$\int_{\Re^3} x_k \left[\frac{\partial (\rho \overline{\mathrm{v}_j})}{\partial t} + \frac{\partial (\rho \overline{\mathrm{v}_i \mathrm{v}_j})}{\partial x_i} + \rho \frac{\partial \Phi}{\partial x_j}\right] \mathrm{d}^3\mathbf{x} = 0. \tag{A.27}$$

The integration of the three terms leads, respectively, to the tensors of eqs. (A.9), (A.10), and (A.15), so that

$$\frac{1}{2}\frac{d^2 I_{jk}}{dt^2} = 2K_{jk} + W_{jk}, \tag{A.28}$$

which is the tensorial expression of the Virial theorem. While the second and third terms are straightforward, the first one is derived as follows:

$$\begin{aligned} \frac{dI_{jk}}{dt} &= \int_{\Re^3} \frac{\partial \rho}{\partial t} x_j x_k \,\mathrm{d}^3\mathbf{x} = \\ &= -\int_{\Re^3} \frac{\partial(\rho \overline{\mathrm{v}_i})}{\partial x_i} x_j x_k \,\mathrm{d}^3\mathbf{x} = \\ &= \int_{\Re^3} \rho \overline{\mathrm{v}_i}(x_k \delta_{ij} + x_j \delta_{ki}) \,\mathrm{d}^3\mathbf{x} = \\ &= \int_{\Re^3} \rho(\overline{\mathrm{v}_j} x_k + \overline{\mathrm{v}_k} x_j) \,\mathrm{d}^3\mathbf{x}, \end{aligned} \tag{A.29}$$

and, since x_k is independent of t, it holds

$$\frac{1}{2}\frac{d^2 I_{jk}}{dt^2} = \int_{\Re^3} x_k \frac{\partial(\rho \overline{\mathrm{v}_j})}{\partial t} \,\mathrm{d}^3\mathbf{x}. \tag{A.30}$$

From the traces of each tensor, the scalar Virial theorem is also immediately verified:

$$\frac{1}{2}\frac{d^2 I}{dt^2} = 2K + W. \tag{A.31}$$

A.3 Stationary and axisymmetric stellar systems

We consider now stationary and axisymmetric stellar systems, in cylindrical coordinates (R, φ, z), and we write the associated Jeans equations and scalar Virial theorem.

The velocity dispersion tensor σ_{ij} is diagonal and aligned with the coordinate system. Moreover, in a stationary and axisymmetric potential Φ, all derivatives with respect to t and φ vanish. There is no rotation in radial and vertical directions, $\overline{\mathrm{v}_R} = \overline{\mathrm{v}_z} = 0$, so the only non-zero streaming motion can occur in the azimuthal direction, $\overline{\mathrm{v}_\varphi}$, and the only non-zero component of the angular momentum is $J_z = R v_\varphi$. Axisymmetry also impose $\sigma_R^2 = \sigma_z^2$. A stationary and axisymmetric system is therefore described by a *two-integral* DF $f(E, J_z)$, which depends on the phase-space coordinates only through two integrals of motion, according with the Jeans theorem: the energy $E = \frac{1}{2}(\mathrm{v}_R^2 + \mathrm{v}_\varphi^2 + \mathrm{v}_z^2) + \Phi$ and the vertical component of the angular momentum J_z, both per unit mass. The Jeans equations become

$$\begin{cases} \dfrac{\partial(\rho\sigma^2)}{\partial z} = -\rho_* \dfrac{\partial \Phi}{\partial z} \\ \\ \dfrac{\partial(\rho\sigma^2)}{\partial R} = \rho \dfrac{\overline{\mathrm{v}_\varphi^2} - \sigma^2}{R} - \rho \dfrac{\partial \Phi}{\partial R}, \end{cases} \tag{A.32}$$

and the scalar Virial theorem reads

$$2K + W = 0. \tag{A.33}$$

In this case, $K = T + \Pi/2 = T_\varphi + \Pi_z + \Pi_\varphi/2$, where from eq. (A.13)

$$T_\varphi = 2\pi \int_0^\infty \int_0^\infty \rho \overline{\mathrm{v}_\varphi}^2 \, R \, \mathrm{d}R \, \mathrm{d}z, \tag{A.34}$$

$$\Pi_z = 4\pi \int_0^\infty \int_0^\infty \rho \sigma_z^2 \, R \, \mathrm{d}R \, \mathrm{d}z, \qquad \Pi_\varphi = 4\pi \int_0^\infty \int_0^\infty \rho \sigma_\varphi^2 \, R \, \mathrm{d}R \, \mathrm{d}z, \tag{A.35}$$

and $\Pi_R = \Pi_z$. Finally,

$$W = -4\pi \int_0^\infty \int_0^\infty \rho \left(R \frac{\partial \Phi}{\partial R} + z \frac{\partial \Phi}{\partial z} \right) R \, \mathrm{d}R \, \mathrm{d}z. \tag{A.36}$$

Appendix B

The numerical code JASMINE2

We report the main technical features of the code JASMINE2, on which this Thesis work is substantially based.

The code JASMINE2 arises from a first version JASMINE (Jeans AxiSymmetric Models of galaxies IN Equilibrium, Posacki et al., 2013; Posacki, 2014), which I partially upgraded for my Master Thesis (Caravita, 2018), and substantially modified during my PhD project. The code produces models of stationary axisymmetric galaxies, based on the solution of the Jeans equations for the dynamics of multiple stellar components in a multicomponent gravitational potential. The idea behind the development of the code is fully illustrated in this Thesis, and so the modelling procedure. Here we report the main technical features.

The code is organised in two main parts, accordingly to the modelling procedure illustrated, in particular in Section 3.2: the Potential & Jeans Solver and the Post-Processing (PP). The Potential & Jeans Solver, due to the computational task of evaluating the gravitational potentials (when analytical potentials are not given) is developed in `Fortran 90`, and it can run in serial or parallel. The PP, instead, is developed in `Python 3`, better suited to the flexibility requested by the exploration of the model parameter space for the combination of the single matter components. The output data produced by the Potential & Jeans Solver are stored in HDF5 files (in binary format), and then read as input in PP. Since all the projection formulae, integrated in PP, are linearly proportional to all the weights, except the (FO/EO) los rotational velocity $v_{\rm los}$ (as discussed in Section 3.2.3), there is actually an intermediate output of the PP: all the *scaled* projected fields are calculated and then stored in HDF5 libraries, while $v_{\rm los}$ is calculated separately after the choice of the mass weights, so that a change in the weights does not require to compute again all the projections.

At this stage, the Potential & Jeans Solver runs in parallel using three processors. Indeed, it works on three axisymmetric grids in $\left(\tilde{R},\tilde{z}\right)$: a principal grid, on which all quantities are computed, and two secondary grids, staggered in $\tilde{R}$ and $\tilde{z}$ respectively, that serve to compute the derivatives of the potentials (forces) with the centred finite-differences method of approximation; the potential of a density component is then calculated simultaneously on the three grids by the three processors. Numerical integrations are performed through the standard trapezoidal rule.

The first version of the code, JASMINE, was supplied by two possible spatial grids, a linear one and a slightly logarithmic one, to better resolve the central regions of the galaxy. This latter was set by choosing the number of grid points, the maximum extension of the grid, and the step between the points, keeping free the minimum value after 0. In this way, however, an increase of the total number of points would increase much more the number of points at small radii, than at large radii. We upgraded JASMINE2 with another slightly logarithmic grid, where we choose the total number of points, the maximum value and the minimum value (after 0), keeping free the step between the points: in this way an increase of the number of grid points would increase the spatial resolution everywhere. The principal spatial grid and the two staggered grids have equal parameters. Moreover, also the grid in λ for the 1D integrations of the Chandrasekhar formula and of the formula based on Bessel functions (Sections 4.2.1 and 4.4, respectively) are built in the same slightly logarithmic way, with suitable parameters.

We report now the parameters usually used for the numerical grids, depending on the need. The grid in $\left(\tilde{R}, \tilde{z}\right)$ usually ranges from 10^{-6} to 70 with 500 points. The seemingly very small minimum value is necessary to assure a good precision in the potential evaluation in terms of elliptic integrals down to $\approx 10^{-3} - 10^{-4}$. Of course, we have performed many checks on the resolution of the spatial grid, in order to find the better possible resolution with the minimum possible computational time: just to give an idea, the Potential & Jeans Solver with three processors spends a couple of days to compute a potential component with elliptic integrals; decreasing down to 350 points, it would spend some hours, giving a quite satisfactory precision for some needs; on the other side, increasing up to 700 points, for example, would require many days of computation, with no significant improvements. The grid in λ (for integrations from 0 to ∞) usually spans a range of $10^{-3} - 10^{6}$ with 500 points, suitable both for the Chandrasekhar formula and for the formula based on Bessel functions (after many checks also in these cases). The two 1D integrations are remarkably fast, spending only few seconds or few minutes, depending on the model. The gain in running time is apparent with respect to the 2D integration based on elliptic integrals, and in Sections 4.3 and 4.4.3 we also show the precision of these alternative methods.

We note that a further parallelization of the Potential & Jeans Solver would be possible, allocating the computation of each of the three potentials of each density component to a different processor, reaching a number of $3 \times N$ processors for N density components. Nevertheless, thanks to the very fast alternative methods implemented in JASMINE2 to evaluate the potentials (collected in Section 4.2), only rarely we need the full numerical integration based on elliptic integrals, and so a further parallelization is avoided for now.

Appendix C

Few notes about Beta functions and Hypergeometric functions

We briefly present the complete and incomplete Beta functions, recalling in particular the properties exploited in the discussions of this Thesis. Then we stress a limit that can be faced in a numerical implementation, and we give useful relations which allow to write the Beta functions in terms of Hypergeometric functions.

We recall, first of all, the complete Beta function, which reads

$$\mathrm{B}(a,b)=\int_0^1 t^{a-1}(1-t)^{b-1}\,\mathrm{d}t, \qquad a>0, \qquad b>0, \tag{C.1}$$

and it is related to the complete Gamma function by $\mathrm{B}(a,b)=\Gamma(a)\Gamma(b)/\Gamma(a+b)$. If $a=b$, it becomes $\mathrm{B}(a,a)=\Gamma(a)^2=\Gamma(2a)$, and, for example, it evaluates to π for $a=1/2$, and to 1 for $a=1$. The incomplete Beta function is given by

$$\mathrm{B}(a,b;x)=\int_0^x t^{a-1}(1-t)^{b-1}\,\mathrm{d}t, \qquad a>0, \qquad b>0 \text{ if } x=1. \tag{C.2}$$

A consideration is in order, especially for a numerical implementation. For example, in Fortran 90, the incomplete Beta function can be implemented following Press et al. (1992) in a *regularised* form, as $\mathrm{I}(a,b;x)=\mathrm{B}(a,b;x)/\mathrm{B}(a,b)$, i.e. normalised for the related complete Beta function. Thus, the incomplete Beta inherits the more limiting conditions of the complete Beta, and it cannot be called for arguments $b\leq 0$, even if it is assured that $x\neq 1$. This occurs, for example, in the expression of the potential of γ-models in homoeoidal expansion (eq. 4.41), and in the evaluation of the potential of the pseudo-isothermal sheet in terms of Bessel functions (eq. 4.61). To avoid this numerical obstacle, we suggest a solution in terms of Hypergeometric functions, by exploiting the relation

$$\mathrm{B}(a,b;x)=\frac{x^a}{a}\,{}_2\mathrm{F}_1(\mathrm{a},1-\mathrm{b};1+\mathrm{a};\mathrm{x}) \tag{C.3}$$

(see e.g. Gradshteyn et al., 2007), where we recall that the Hypergeometric function ${}_2\mathrm{F}_1$ is symmetric with respect to the first two arguments, so that ${}_2\mathrm{F}_1(\mathrm{a},\mathrm{b};\mathrm{c};\mathrm{x})={}_2\mathrm{F}_1(\mathrm{b},\mathrm{a};\mathrm{c};\mathrm{x})$. Moreover, many relations exist between Hypergeometric functions ${}_2\mathrm{F}_1$, allowing for the use of different arguments, which can be useful in some cases. For instance, it holds

$${}_2\mathrm{F}_1(\mathrm{a},\mathrm{b};\mathrm{c};\mathrm{x})=\frac{1}{(1-\mathrm{x})^{\mathrm{a}}}\,{}_2\mathrm{F}_1\left(\mathrm{a},\mathrm{c}-\mathrm{b};\mathrm{c};\frac{\mathrm{x}}{\mathrm{x}-1}\right). \tag{C.4}$$

Appendix D

Hankel transforms for some radial density profiles

We report the analytical Hankel transform of some radial density distributions, used for the evaluation of the gravitational potential of factorised discs in terms of Bessel functions, as discussed in Section 4.4.

We report here some well-known radial distributions in the form $A(R)$ (eq. 4.49), for which we show the related analytical solutions for the Hankel transform $\hat{A}(k)$ (eqs. 4.50 and 4.51). We avoid to derive them, since they are exhaustively treated for example in Ciotti (2021). The radial decreasing of the mass density on a disc can be naturally finite, truncated, so that the total mass is enclosed in a certain truncation radius R_t, or can continue towards infinity. The Hankel transform of eq. (4.51) can be written in general as

$$\hat{A}(k) = R_\mathrm{d}^2 \int_0^\infty g(t)\, \mathrm{J}_0(\lambda t)\, t\, \mathrm{d}t, \qquad \lambda = kR_\mathrm{d}, \quad t = R'/R_\mathrm{d}, \tag{D.1}$$

with R_d the scale-radius of the disc, on the same line of eq. (4.54) for the vertical stratification.

We start from the exponential disc (Freeman, 1970), for which

$$A(R) = \mathrm{e}^{-R/R_\mathrm{d}}, \qquad \hat{A}(k) = \frac{R_\mathrm{d}^2}{\left(1+\lambda^2\right)^{3/2}}, \qquad \lambda = kR_\mathrm{d}, \tag{D.2}$$

in agreement with Kuijken and Gilmore (1989) and Cuddeford (1993). For the Kuzmin-Toomre disc (Kuzmin, 1956; Toomre, 1963), we have

$$A(R) = \left(1 + R^2/R_\mathrm{d}^2\right)^{-3/2}, \qquad \hat{A}(k) = R_\mathrm{d}^2 \mathrm{e}^{-kR_\mathrm{d}}. \tag{D.3}$$

We include also some truncated discs of finite mass enclosed in a truncation radius R_t, by exploiting the Heaviside step function Θ: for example, the truncated constant density disc (Mestel, 1963),

$$A(R) = \Theta(1 - R/R_\mathrm{t}), \qquad \hat{A}(k) = \frac{R_\mathrm{t}^2 J_1(\lambda)}{\lambda}, \qquad \lambda = kR_\mathrm{t}; \tag{D.4}$$

the Maclaurin disc (Mestel, 1963; Kalnajs, 1972; Schulz, 2009),

$$A(R) = \sqrt{1 - R^2/R_\mathrm{t}^2}\, \Theta(1 - R/R_\mathrm{t}), \qquad \hat{A}(k) = R_\mathrm{t}^2 \frac{\sin\lambda - \lambda\cos\lambda}{\lambda^3}, \qquad \lambda = kR_\mathrm{t}; \tag{D.5}$$

the truncated Mestel disc (Mestel, 1963),

$$A(R) = \frac{\Theta(1 - R/R_\mathrm{t})}{R/R_\mathrm{d}}, \qquad \hat{A}(k) = R_\mathrm{d} R_\mathrm{t} \left\{ \mathrm{J}_0(\lambda) + \frac{\pi}{2}\left[J_1(\lambda)\mathrm{H}_0(\lambda) - \mathrm{J}_0(\lambda)\mathrm{H}_1(\lambda) \right] \right\}, \qquad \lambda = kR_\mathrm{t}, \tag{D.6}$$

where we stress the different meaning of R_d and R_t, and H_0 and H_1 are Struve functions of the zero-th and first order, respectively. At variance, for the finite Mestel disc (Mestel, 1963; Lynden-Bell and Pineault, 1978; Brada and Milgrom, 1995; Schulz, 2012), we have

$$A(R) = \frac{\arccos(R/R_\mathrm{t})}{R/R_\mathrm{t}}\, \Theta(1 - R/R_\mathrm{t}), \qquad \hat{A}(k) = \frac{R_\mathrm{t}^2\, \mathrm{Si}(\lambda)}{\lambda}, \qquad \lambda = kR_\mathrm{t}, \tag{D.7}$$

where we refer to the sine integral function $\mathrm{Si}(\lambda) = \int_0^\lambda \sin x/x\, \mathrm{d}x$. Finally, the untruncated Mestel disc is obtained from the truncated case of eq. (D.6) in the limit $R_\mathrm{t} \to \infty$, so that

$$A(R) = \frac{R_\mathrm{d}}{R}, \qquad \hat{A}(k) = \frac{R_\mathrm{d}}{k}. \tag{D.8}$$

Appendix E

Positivity condition for JJE models

We derive the condition assuring the positivity of the density distribution obtained by difference in JJE models, presented in Section 5.1.

Caravita C., Ciotti L. and Pellegrini S., 2021, MNRAS

The stellar component ρ_{*2}, for the two-component ellipsoidal models JJE, described in Section 5.1, is given by the difference of an assigned total ρ_* and an assigned ρ_{*1}. This approach naturally leads to discuss the positivity of ρ_{*2}, with a treatment similar to that followed in the appendix of CMPZ21, and references therein. We recast eq. (5.3) in the generalisation of γ-models, in agreement with eq. (4.1), so that

$$\frac{\rho_{*2}(R,z)}{(3-\gamma)\rho_{\rm n}} = \frac{\xi}{qm^{\gamma}(\xi+m)^{4-\gamma}} - \frac{\mathcal{R}_1\xi_1}{q_1 m_1^{\gamma}(\xi_1+m_1)^{4-\gamma}}, \tag{E.1}$$

recovering the case of JJE models for $\gamma = 2$. In order to discuss the positivity condition for ρ_{*2}, we use spherical coordinates, so that $(R,z) = r(\sin\theta, \cos\theta)$ and

$$m = s\Omega, \quad m_1 = s\Omega_1, \quad s \equiv \frac{r}{r_*}, \tag{E.2}$$

where

$$\Omega^2 \equiv \sin^2\theta + \frac{\cos^2\theta}{q^2}, \quad \Omega_1^2 \equiv \sin^2\theta + \frac{\cos^2\theta}{q_1^2}. \tag{E.3}$$

The positivity of ρ_{*2} reduces to a condition on $\mathcal{R}_1$, given by

$$\mathcal{R}_1 \le \mathcal{R}_{\rm M} \equiv \inf_{\mathcal{I}} \left[\frac{\xi q_1}{\xi_1 q}\left(\frac{\Omega_1}{\Omega}\right)^{\gamma}\left(\frac{\xi_1+s\Omega_1}{\xi+s\Omega}\right)^{4-\gamma}\right], \tag{E.4}$$

over the rectangular region $\mathcal{I} \equiv \{s \ge 0, 0 \le \theta \le \pi/2\}$ in the (s,θ) plane. Following the discussion in CMPZ21, we determine

$$\mathcal{R}_{\rm M} = \min\left(\mathcal{R}_{\rm c}, \mathcal{R}_{\infty}, \mathcal{R}_0, \mathcal{R}_{\pi/2}, \mathcal{R}_{\rm int}\right), \tag{E.5}$$

where the first four quantities refer to the minimum value of the r.h.s. of eq. (E.4) over the boundaries of $\mathcal{I}$, and $\mathcal{R}_{\rm int}$ is the value of a minimum (if it exists) in the interior of $\mathcal{I}$. When $q_1 \neq q$, it is simple to show that no critical points can exist in the interior of $\mathcal{I}$, and so the discussion reduces to the boundaries of $\mathcal{I}$: geometrically, $\mathcal{R}_{\rm M}$ can be reached only at the centre ($s = 0$, $\mathcal{R}_{\rm c}$), at infinity ($s \to \infty$, $\mathcal{R}_{\infty}$), along the symmetry axis ($\theta = 0$, $\mathcal{R}_0$), or on the equatorial plane ($\theta = \pi/2$, $\mathcal{R}_{\pi/2}$).

We begin with $\mathcal{R}_{\rm c}$ and $\mathcal{R}_{\infty}$, obtaining

$$\mathcal{R}_{\rm c} = \frac{\xi_1^{3-\gamma} q_1}{\xi^{3-\gamma} q} \min_{0\le\theta\le\pi/2}\left(\frac{\Omega_1}{\Omega}\right)^{\gamma}, \tag{E.6}$$

$$\mathcal{R}_{\infty} = \frac{\xi q_1}{\xi_1 q} \min_{0\le\theta\le\pi/2}\left(\frac{\Omega_1}{\Omega}\right)^{4}. \tag{E.7}$$

Now, from eq. (E.3), it is easy to show that for a generic $\alpha \ge 0$, the function $(\Omega_1/\Omega)^{\alpha}$ reaches its minimum at $\theta = \pi/2$ if $q_1 \le q$, and at $\theta = 0$ if $q \le q_1$, so that

$$\min_{0\le\theta\le\pi/2}\left(\frac{\Omega_1}{\Omega}\right)^{\alpha} = \begin{cases} 1, & q_1 \le q, \\ \left(\dfrac{q}{q_1}\right)^{\alpha}, & q \le q_1, \end{cases} \tag{E.8}$$

and the conditions in eqs. (E.6) and (E.7) can be finally summarised as

$$\mathcal{R}_{\mathrm{c}} = \frac{\xi_1^{3-\gamma} q_1}{\xi^{3-\gamma} q} \min\left(1, \frac{q^\gamma}{q_1^\gamma}\right), \tag{E.9}$$

$$\mathcal{R}_\infty = \frac{\xi q_1}{\xi_1 q} \min\left(1, \frac{q^4}{q_1^4}\right). \tag{E.10}$$

Along the symmetry axis, and in the equatorial plane, condition (E.4) becomes

$$\mathcal{R}_0 = \frac{\xi q^3}{\xi_1 q_1^3} \inf_{0\leq s<\infty} \left(\frac{\xi_1 q_1 + s}{\xi q + s}\right)^{4-\gamma}, \tag{E.11}$$

$$\mathcal{R}_{\pi/2} = \frac{\xi q_1}{\xi_1 q} \inf_{0\leq s<\infty} \left(\frac{\xi_1 + s}{\xi + s}\right)^{4-\gamma}, \tag{E.12}$$

and simple algebra finally shows that the results can be summarised as

$$\mathcal{R}_0 = \frac{\xi q^3}{\xi_1 q_1^3} \min\left[1, \left(\frac{\xi_1 q_1}{\xi q}\right)^{4-\gamma}\right], \tag{E.13}$$

$$\mathcal{R}_{\pi/2} = \frac{\xi q_1}{\xi_1 q} \min\left(1, \frac{\xi_1^{4-\gamma}}{\xi^{4-\gamma}}\right). \tag{E.14}$$

For the JJE models in Section 5.1, with $\xi_1 < \xi$, $q_1 < q$, and $\gamma = 2$, the positivity condition (E.5) becomes

$$\mathcal{R}_1 \leq \mathcal{R}_{\mathrm{M}} = \frac{\xi_1 q_1}{\xi q}. \tag{E.15}$$

Bibliography

Auger, M. W., Treu, T., Bolton, A. S., Gavazzi, R., Koopmans, L. V. E., Marshall, P. J., Moustakas, L. A. and Burles, S. (2010), 'The Sloan Lens ACS Survey. X. Stellar, Dynamical, and Total Mass Correlations of Massive Early-type Galaxies', **724**(1), 511–525.

Barnabè, M., Czoske, O., Koopmans, L. V. E., Treu, T. and Bolton, A. S. (2011), 'Two-dimensional kinematics of SLACS lenses - III. Mass structure and dynamics of early-type lens galaxies beyond z â 0.1', **415**(3), 2215–2232.

Bellstedt, S., Forbes, D. A., Romanowsky, A. J., Remus, R.-S., Stevens, A. R. H., Brodie, J. P., Poci, A., McDermid, R., Alabi, A., Chevalier, L., Adams, C., Ferré-Mateu, A., Wasserman, A. and Pandya, V. (2018), 'The SLUGGS survey: a comparison of total-mass profiles of early-type galaxies from observations and cosmological simulations, to ∼4 effective radii', **476**(4), 4543–4564.

Bernardi, M., Sheth, R. K., Dominguez-Sanchez, H., Fischer, J. L., Chae, K. H., Huertas-Company, M. and Shankar, F. (2018), 'M_*/L gradients driven by IMF variation: large impact on dynamical stellar mass estimates', **477**(2), 2560–2571.

Bertin, G., Ciotti, L. and Del Principe, M. (2002), 'Weak homology of elliptical galaxies.', **386**, 149–168.

Binney, J. (1978), 'On the rotation of elliptical galaxies', *MNRAS* **183**, 501–514.

Binney, J. and McMillan, P. J. (2016), 'Torus mapper: a code for dynamical models of galaxies', **456**(2), 1982–1998.

Binney, J. and Tremaine, S. (1987), *Galactic dynamics*.

Binney, J. and Tremaine, S. (2008), *Galactic Dynamics: Second Edition*, Princeton University Press.

Bovy, J. (2022), *Dynamics and Astrophysics of Galaxies*, Princeton University Press, in preparation.

Brada, R. and Milgrom, M. (1995), 'Finite Disks with Power-Law Potentials', **444**, 71.

Brighenti, F. and Mathews, W. G. (1996), 'Structure and Evolution of Interstellar Gas in Flattened, Rotating Elliptical Galaxies', **470**, 747.

Brighenti, F. and Mathews, W. G. (1997), 'Evolution of Interstellar Gas in Rapidly Rotating Elliptical Galaxies: Formation of Disks', **490**(2), 592–604.

Cappellari, M. (2002), 'Efficient multi-Gaussian expansion of galaxies', **333**(2), 400–410.

Cappellari, M. (2008), 'Measuring the inclination and mass-to-light ratio of axisymmetric galaxies via anisotropic Jeans models of stellar kinematics', *MNRAS* **390**, 71–86.

Cappellari, M. (2016), 'Structure and Kinematics of Early-Type Galaxies from Integral Field Spectroscopy', *ARAA* **54**, 597–665.

Cappellari, M., McDermid, R. M., Alatalo, K., Blitz, L., Bois, M., Bournaud, F., Bureau, M., Crocker, A. F., Davies, R. L., Davis, T. A., de Zeeuw, P. T., Duc, P.-A., Emsellem, E., Khochfar, S., Krajnović, D., Kuntschner, H., Lablanche, P.-Y., Morganti, R., Naab, T., Oosterloo, T., Sarzi, M., Scott, N., Serra, P., Weijmans, A.-M. and Young, L. M. (2012), 'Systematic variation of the stellar initial mass function in early-type galaxies', *Nature* **484**, 485–488.

Cappellari, M., McDermid, R. M., Alatalo, K., Blitz, L., Bois, M., Bournaud, F., Bureau, M., Crocker, A. F., Davies, R. L., Davis, T. A., de Zeeuw, P. T., Duc, P.-A., Emsellem, E., Khochfar, S., Krajnović, D., Kuntschner, H., Morganti, R., Naab, T., Oosterloo, T., Sarzi, M., Scott, N., Serra, P., Weijmans, A.-M. and Young, L. M. (2013), 'The ATLAS^{3D} project - XX. Mass-size and mass-σ distributions of early-type galaxies: bulge fraction drives kinematics, mass-to-light ratio, molecular gas fraction and stellar initial mass function', *MNRAS* **432**, 1862–1893.

Cappellari, M., Romanowsky, A. J., Brodie, J. P., Forbes, D. A., Strader, J., Foster, C., Kartha, S. S., Pastorello, N., Pota, V., Spitler, L. R., Usher, C. and Arnold, J. A. (2015), 'Small Scatter and Nearly Isothermal Mass Profiles to Four Half-light Radii from Two-dimensional Stellar Dynamics of Early-type Galaxies', **804**(1), L21.

Caravita, C. (2018), *Master Thesis*, Bologna University.

Caravita, C., Ciotti, L. and Pellegrini, S. (2020), Dynamical models of spheroidal multi-component stellar systems, *in* A. Bragaglia, M. Davies, A. Sills and E. Vesperini, eds, 'Star Clusters: From the Milky Way to the Early Universe', Vol. 351, pp. 273–276.

Caravita, C., Ciotti, L. and Pellegrini, S. (2021), 'Jeans modelling of axisymmetric galaxies with multiple stellar populations', **506**(1), 1480–1497.

Casertano, S. (1983), 'Rotation curve of the edge-on spiral galaxy NGC 5907 : disc and halo masses.', **203**, 735–747.

Chandrasekhar, S. (1969), *Ellipsoidal figures of equilibrium.*

Ciotti, L. (2021), *Introduction to Stellar Dynamics*, Cambridge University Press.

Ciotti, L. and Bertin, G. (2005), 'A simple method to construct exact density-potential pairs from a homeoidal expansion', **437**(2), 419–427.

Ciotti, L., Mancino, A. and Pellegrini, S. (2019), 'A new class of galaxy models with a central BH - I. The spherical case', **490**(2), 2656–2667.

Ciotti, L., Mancino, A., Pellegrini, S. and Ziaee Lorzad, A. (2021), 'Two-component galaxy models with a central BH - II. The ellipsoidal case', **500**(1), 1054–1070.

Ciotti, L. and Ostriker, J. P. (2001), 'Cooling Flows and Quasars. II. Detailed Models of Feedback-modulated Accretion Flows', **551**(1), 131–152.

Ciotti, L. and Ostriker, J. P. (2007), 'Radiative Feedback from Massive Black Holes in Elliptical Galaxies: AGN Flaring and Central Starburst Fueled by Recycled Gas', **665**(2), 1038–1056.

Ciotti, L., Ostriker, J. P., Gan, Z., Jiang, B. X., Pellegrini, S., Caravita, C. and Mancino, A. (2022), 'A Parameter Space Exploration of High Resolution Numerically Evolved Early Type Galaxies Including AGN Feedback and Accurate Dynamical Treatment of Stellar Orbits', *arXiv e-prints* p. arXiv:2201.03909.

Ciotti, L. and Pellegrini, S. (1996), 'The energetics of flat and rotating early-type galaxies and their X-ray luminosity', *MNRAS* **279**, 240.

Ciotti, L., Pellegrini, S., Negri, A. and Ostriker, J. P. (2017), 'The Effect of the AGN Feedback on the Interstellar Medium of Early-Type Galaxies:2D Hydrodynamical Simulations of the Low-Rotation Case.', **835**(1), 15.

Ciotti, L. and Ziaee Lorzad, A. (2018), 'Two-component Jaffe models with a central black hole - I. The spherical case', *MNRAS* **473**, 5476–5491.

Cuddeford, P. (1993), 'On the potentials of galactic discs', **262**(4), 1076–1086.

de Vaucouleurs, G. (1948), 'Recherches sur les nébuleuses extragalactiques', *Journal des Observateurs* **31**, 113.

de Zeeuw, P. T. and Lynden-Bell, D. (1985), 'Best approximate quadratic integrals in stellar dynamics', **215**, 713–730.

de Zeeuw, T. (1985), 'Elliptical galaxies with separable potentials', **216**, 273–334.

Dehnen, W. (1993), 'A Family of Potential-Density Pairs for Spherical Galaxies and Bulges', **265**, 250.

D'Ercole, A. and Ciotti, L. (1998), 'Decoupled and Inhomogeneous Gas Flows in S0 Galaxies', **494**(2), 535–545.

Djorgovski, S. and Davis, M. (1987), 'Fundamental properties of elliptical galaxies', *ApJ* **313**, 59–68.

Dressler, A., Lynden-Bell, D., Burstein, D., Davies, R. L., Faber, S. M., Terlevich, R. and Wegner, G. (1987), 'Spectroscopy and photometry of elliptical galaxies. I - A new distance estimator', *ApJ* **313**, 42–58.

Efstathiou, G., Lake, G. and Negroponte, J. (1982), 'The stability and masses of disc galaxies.', **199**, 1069–1088.

Einasto, J. (1965), 'On the Construction of a Composite Model for the Galaxy and on the Determination of the System of Galactic Parameters', *Trudy Astrofizicheskogo Instituta Alma-Ata* **5**, 87–100.

Emsellem, E., Cappellari, M., Krajnović, D., Alatalo, K., Blitz, L., Bois, M., Bournaud, F., Bureau, M., Davies, R. L., Davis, T. A., de Zeeuw, P. T., Khochfar, S., Kuntschner, H., Lablanche, P.-Y., McDermid, R. M., Morganti, R., Naab, T., Oosterloo, T., Sarzi, M., Scott, N., Serra, P., van de Ven, G., Weijmans, A.-M. and Young, L. M. (2011), 'The ATLAS^{3D} project - III. A census of the stellar angular momentum within the effective radius of early-type galaxies: unveiling the distribution of fast and slow rotators', *MNRAS* **414**, 888–912.

Eskridge, P. B., Fabbiano, G. and Kim, D.-W. (1995), 'A Multiparametric Analysis of the Einstein Sample of Early-Type Galaxies. I. Luminosity and ISM Parameters', **97**, 141.

Evans, N. W. and de Zeeuw, P. T. (1992), 'Potential-density pairs for flat galaxies', **257**(1), 152–176.

Faber, S. M. and Jackson, R. E. (1976), 'Velocity dispersions and mass-to-light ratios for elliptical galaxies', *ApJ* **204**, 668–683.

Flynn, C., Sommer-Larsen, J. and Christensen, P. R. (1996), 'Kinematics of the outer stellar halo', **281**(3), 1027–1032.

Freeman, K. C. (1970), 'On the Disks of Spiral and S0 Galaxies', **160**, 811.

Gan, Z., Choi, E., Ostriker, J. P., Ciotti, L. and Pellegrini, S. (2019), 'Adding a Suite of Chemical Abundances to the MACER Code for the Evolution of Massive Elliptical Galaxies', **875**(2), 109.

Gan, Z., Ciotti, L., Ostriker, J. P. and Yuan, F. (2019), 'MACER Improved: AGN Feedback Computed in Rotating Early-type Galaxies at High Resolution', **872**(2), 167.

Gan, Z., Hensley, B. S., Ostriker, J. P., Ciotti, L., Schiminovich, D. and Pellegrini, S. (2020), 'Infrared Emission from Cold Gas Dusty Disks in Massive Ellipticals', **901**(1), 7.

García-Benito, R., González Delgado, R. M., Pérez, E., Cid Fernandes, R., Sánchez, S. F. and de Amorim, A. L. (2019), 'Spatially resolved mass-to-light from the CALIFA survey. Mass-to-light ratio vs. color relations', **621**, A120.

Gavazzi, R., Treu, T., Rhodes, J. D., Koopmans, L. V. E., Bolton, A. S., Burles, S., Massey, R. J. and Moustakas, L. A. (2007), 'The Sloan Lens ACS Survey. IV. The Mass Density Profile of Early-Type Galaxies out to 100 Effective Radii', **667**(1), 176–190.

Gradshteyn, I. S., Ryzhik, I. M., Jeffrey, A. and Zwillinger, D. (2007), *Table of Integrals, Series, and Products.*

Graham, A. W., Merritt, D., Moore, B., Diemand, J. and Terzić, B. (2006), 'Empirical Models for Dark Matter Halos. II. Inner Profile Slopes, Dynamical Profiles, and ρ/σ^3', **132**(6), 2701–2710.

Hernquist, L. (1990), 'An Analytical Model for Spherical Galaxies and Bulges', **356**, 359.

Hohl, F. (1971), 'Numerical Experiments with a Disk of Stars', **168**, 343.

Hubble, E. P. (1936), *Realm of the Nebulae.*

Jackson, J. D. (1998), *Classical Electrodynamics, 3rd Edition.*

Jaffe, W. (1983), 'A simple model for the distribution of light in spherical galaxies', *MNRAS* **202**, 995–999.

Jeans, J. H. (1922), 'The Motions of Stars in a Kapteyn Universe', *MNRAS* **82**, 122–132.

Juráňová, A., Werner, N., Nulsen, P. E. J., Gaspari, M., Lakhchaura, K., Canning, R. E. A., Donahue, M., Hroch, F. and Voit, G. M. (2020), 'Hot gaseous atmospheres of rotating galaxies observed with XMM-Newton', **499**(4), 5163–5174.

Jurić, M., Ivezić, Ž., Brooks, A., Lupton, R. H., Schlegel, D., Finkbeiner, D., Padmanabhan, N., Bond, N., Sesar, B., Rockosi, C. M., Knapp, G. R., Gunn, J. E., Sumi, T., Schneider, D. P., Barentine, J. C., Brewington, H. J., Brinkmann, J., Fukugita, M., Harvanek, M., Kleinman, S. J., Krzesinski, J., Long, D., Neilsen, Eric H., J., Nitta, A., Snedden, S. A. and York, D. G. (2008), 'The Milky Way Tomography with SDSS. I. Stellar Number Density Distribution', **673**(2), 864–914.

Kalnajs, A. J. (1972), 'The Equilibria and Oscillations of a Family of Uniformly Rotating Stellar Disks', **175**, 63.

Kim, D.-W. and Fabbiano, G. (2015), 'X-Ray Scaling Relations of 'Core' and 'Coreless' E and S0 Galaxies', **812**(2), 127.

Kim, D.-W. and Pellegrini, S. (2012), *Hot Interstellar Matter in Elliptical Galaxies*, Vol. 378 of *Astrophysics and Space Science Library.*

Koopmans, L. V. E., Bolton, A., Treu, T., Czoske, O., Auger, M. W., Barnabè, M., Vegetti, S., Gavazzi, R., Moustakas, L. A. and Burles, S. (2009), 'The Structure and Dynamics of Massive Early-Type Galaxies: On Homology, Isothermality, and Isotropy Inside One Effective Radius', **703**(1), L51–L54.

Kormendy, J. (1977), 'Brightness distributions in compact and normal galaxies. II - Structure parameters of the spheroidal component', *ApJ* **218**, 333–346.

Kormendy, J. and Ho, L. C. (2013), 'Coevolution (Or Not) of Supermassive Black Holes and Host Galaxies', **51**(1), 511–653.

Krajnović, D., Emsellem, E., Cappellari, M., Alatalo, K., Blitz, L., Bois, M., Bournaud, F., Bureau, M., Davies, R. L., Davis, T. A., de Zeeuw, P. T., Khochfar, S., Kuntschner, H., Lablanche, P.-Y., McDermid, R. M., Morganti, R., Naab, T., Oosterloo, T., Sarzi, M., Scott, N., Serra, P., Weijmans, A.-M. and Young, L. M. (2011), 'The ATLAS^{3D} project - II. Morphologies, kinemetric features and alignment between photometric and kinematic axes of early-type galaxies', **414**(4), 2923–2949.

Krajnović, D., Weilbacher, P. M., Urrutia, T., Emsellem, E., Carollo, C. M., Shirazi, M., Bacon, R., Contini, T., Epinat, B., Kamann, S., Martinsson, T. and Steinmetz, M. (2015), 'Unveiling the counter-rotating nature of the kinematically distinct core in NGC 5813 with MUSE', **452**(1), 2–18.

Kuijken, K. and Gilmore, G. (1989), 'The mass distribution in the galactic disc. I - A technique to determine the integral surface mass density of the disc near the sun.', **239**, 571–603.

Kuzmin, G. G. (1956), 'A stationary galaxy model admitting triaxial velocity distribution', **33**, 27.

Lanzoni, B. and Ciotti, L. (2003), 'Projection effects on the FP thickness. A Monte-Carlo exploration', **404**, 819–830.

Li, R., Shu, Y. and Wang, J. (2018), 'Strong-lensing measurement of the total-mass-density profile out to three effective radii for z $\sim$ 0.5 early-type galaxies', **480**(1), 431–438.

Lynden-Bell, D. and Pineault, S. (1978), 'Relativistic disks - 1. Counter rotating disks', **185**, 679–694.

Lyskova, N., Churazov, E. and Naab, T. (2018), 'Mass density slope of elliptical galaxies from strong lensing and resolved stellar kinematics', **475**(2), 2403–2414.

Magorrian, J., Tremaine, S., Richstone, D., Bender, R., Bower, G., Dressler, A., Faber, S. M., Gebhardt, K., Green, R., Grillmair, C., Kormendy, J. and Lauer, T. (1998), 'The Demography of Massive Dark Objects in Galaxy Centers', *AJ* **115**, 2285–2305.

Maraston, C. (2005), 'Evolutionary population synthesis: models, analysis of the ingredients and application to high-z galaxies', *MNRAS* **362**, 799–825.

Martín-Navarro, I., La Barbera, F., Vazdekis, A., Falcón-Barroso, J. and Ferreras, I. (2015), 'Radial variations in the stellar initial mass function of early-type galaxies', **447**(2), 1033–1048.

Mathews, W. G. and Brighenti, F. (2003), 'Hot Gas in and around Elliptical Galaxies', **41**, 191–239.

Mellier, Y. and Mathez, G. (1987), 'Deprojection of the de Vaucouleurs R exp 1/4 brightness profile', *AAp* **175**, 1–3.

Mestel, L. (1963), 'On the galactic law of rotation', **126**, 553.

Mitzkus, M., Cappellari, M. and Walcher, C. J. (2017), 'Dominant dark matter and a counter-rotating disc: MUSE view of the low-luminosity S0 galaxy NGC 5102', **464**(4), 4789–4806.

Miyamoto, M. and Nagai, R. (1975), 'Three-dimensional models for the distribution of mass in galaxies.', **27**, 533–543.

Mo, H., van den Bosch, F. C. and White, S. (2010), *Galaxy Formation and Evolution*.

Morelli, L., Halliday, C., Corsini, E. M., Pizzella, A., Thomas, D., Saglia, R. P., Davies, R. L., Bender, R., Birkinshaw, M. and Bertola, F. (2004), 'Nuclear stellar discs in low-luminosity elliptical galaxies: NGC 4458 and 4478', **354**, 753–762.

Navarro, J. F., Frenk, C. S. and White, S. D. M. (1996), 'The Structure of Cold Dark Matter Halos', *ApJ* **462**, 563.

Negri, A., Ciotti, L. and Pellegrini, S. (2014), 'The effects of stellar dynamics on the X-ray emission of flat early-type galaxies', **439**(1), 823–844.

Negri, A., Pellegrini, S. and Ciotti, L. (2015), 'X-ray haloes and star formation in early-type galaxies', **451**(2), 1212–1228.

Negri, A., Posacki, S., Pellegrini, S. and Ciotti, L. (2014), 'The effects of galaxy shape and rotation on the X-ray haloes of early-type galaxies - II. Numerical simulations', **445**(2), 1351–1369.

Novak, G. S., Ostriker, J. P. and Ciotti, L. (2011), 'Feedback from Central Black Holes in Elliptical Galaxies: Two-dimensional Models Compared to One-dimensional Models', **737**(1), 26.

Ostriker, J. P. and Peebles, P. J. E. (1973), 'A Numerical Study of the Stability of Flattened Galaxies: or, can Cold Galaxies Survive?', **186**, 467–480.

Parikh, T., Thomas, D., Maraston, C., Westfall, K. B., Goddard, D., Lian, J., Meneses-Goytia, S., Jones, A., Vaughan, S., Andrews, B. H., Bershady, M., Bizyaev, D., Brinkmann, J., Brownstein, J. R., Bundy, K., Drory, N., Emsellem, E., Law, D. R., Newman, J. A., Roman-Lopes, A., Wake, D., Yan, R. and Zheng, Z. (2018), 'SDSS-IV MaNGA: the spatially resolved stellar initial mass function in ∼400 early-type galaxies', **477**(3), 3954–3982.

Pellegrini, S., Ciotti, L., Negri, A. and Ostriker, J. P. (2018), 'Active Galactic Nuclei Feedback and the Origin and Fate of the Hot Gas in Early-type Galaxies', **856**(2), 115.

Pellegrini, S., Held, E. V. and Ciotti, L. (1997), 'X-ray emission and internal kinematics in early-type galaxies - I. Observations', **288**(1), 1–11.

Plummer, H. C. (1911), 'On the problem of distribution in globular star clusters', **71**, 460–470.

Poci, A., Cappellari, M. and McDermid, R. M. (2017), 'Systematic trends in total-mass profiles from dynamical models of early-type galaxies', *MNRAS* **467**, 1397–1413.

Posacki, S. (2014), *The dynamics of early-type galaxies as a tool to understand their hot coronae and their IMF.*

Posacki, S., Pellegrini, S. and Ciotti, L. (2013), 'The effects of galaxy shape and rotation on the X-ray haloes of early-type galaxies', *MNRAS* **433**, 2259–2274.

Press, W. H., Teukolsky, S. A., Vetterling, W. T. and Flannery, B. P. (1992), *Numerical recipes in FORTRAN. The art of scientific computing.*

Renzini, A. and Buzzoni, A. (1986), Global properties of stellar populations and the spectral evolution of galaxies., *in* C. Chiosi and A. Renzini, eds, 'Spectral Evolution of Galaxies', Vol. 122 of *Astrophysics and Space Science Library*, pp. 195–231.

Rojas-Niño, A., Read, J. I., Aguilar, L. and Delorme, M. (2016), 'An efficient positive potential-density pair expansion for modelling galaxies', **459**(3), 3349–3355.

Roncadelli, M. and Galanti, G. (2021), 'New strong constraint on the central behaviour of spherical galactic models – No NFW cusp', *arXiv e-prints* p. arXiv:2109.13284.

Sandage, A. (1961), *The Hubble Atlas of Galaxies.*

Sarzi, M., Alatalo, K., Blitz, L., Bois, M., Bournaud, F., Bureau, M., Cappellari, M., Crocker, A., Davies, R. L., Davis, T. A., de Zeeuw, P. T., Duc, P.-A., Emsellem, E., Khochfar, S., Krajnović, D., Kuntschner, H., Lablanche, P.-Y., McDermid, R. M., Morganti, R., Naab, T., Oosterloo, T., Scott, N., Serra, P., Young, L. M. and Weijmans, A.-M. (2013), 'The ATLAS^{3D} project - XIX. The hot gas content of early-type galaxies: fast versus slow rotators', **432**(3), 1845–1861.

Satoh, C. (1980), 'Dynamical Models of Axisymmetric Galaxies and Their Applications to the Elliptical Galaxy NGC4697', *PASJ* **32**, 41.

Schulz, E. (2009), 'Potential-Density Pairs for a Family of Finite Disks', **693**(2), 1310–1315.

Schulz, E. (2012), 'The Gravitational Force and Potential of the Finite Mestel Disk', **747**(2), 106.

Schwarzschild, M. (1979), 'A numerical model for a triaxial stellar system in dynamical equilibrium.', **232**, 236–247.

Sellwood, J. A. (1983), Disk stability, *in* E. Athanassoula, ed., 'Internal Kinematics and Dynamics of Galaxies', Vol. 100, pp. 197–202.

Serra, P., Oosterloo, T., Cappellari, M., den Heijer, M. and Józsa, G. I. G. (2016), 'Linear relation between H I circular velocity and stellar velocity dispersion in early-type galaxies, and slope of the density profiles', **460**(2), 1382–1389.

Sérsic, J. L. (1963), 'Influence of the atmospheric and instrumental dispersion on the brightness distribution in a galaxy', *Boletin de la Asociacion Argentina de Astronomia La Plata Argentina* **6**, 41.

Smet, C. O., Posacki, S. and Ciotti, L. (2015), 'Miyamoto-Nagai discs embedded in the Binney logarithmic potential: analytical solution of the two-integrals Jeans equations', **448**(3), 2921–2933.

Smith, R., Flynn, C., Candlish, G. N., Fellhauer, M. and Gibson, B. K. (2015), 'Simple and accurate modelling of the gravitational potential produced by thick and thin exponential discs', **448**(3), 2934–2940.

Spitzer, Lyman, J. (1942), 'The Dynamics of the Interstellar Medium. III. Galactic Distribution.', **95**, 329.

Springel, V., Di Matteo, T. and Hernquist, L. (2005), 'Modelling feedback from stars and black holes in galaxy mergers', **361**(3), 776–794.

Stone, J. M., Gardiner, T. A., Teuben, P., Hawley, J. F. and Simon, J. B. (2008), 'Athena: A New Code for Astrophysical MHD', **178**(1), 137–177.

Stone, J. M., Tomida, K., White, C. J. and Felker, K. G. (2020), 'The Athena++ Adaptive Mesh Refinement Framework: Design and Magnetohydrodynamic Solvers', **249**(1), 4.

Syer, D. and Tremaine, S. (1996), 'Made-to-measure N-body systems', **282**(1), 223–233.

Toomre, A. (1963), 'On the Distribution of Matter Within Highly Flattened Galaxies.', **138**, 385.

Toomre, A. (1964), ‘On the gravitational stability of a disk of stars.’, **139**, 1217–1238.

Tremaine, S., Richstone, D. O., Byun, Y.-I., Dressler, A., Faber, S. M., Grillmair, C., Kormendy, J. and Lauer, T. R. (1994), ‘A Family of Models for Spherical Stellar Systems’, **107**, 634.

van Dokkum, P., Conroy, C., Villaume, A., Brodie, J. and Romanowsky, A. J. (2017), ‘The Stellar Initial Mass Function in Early-type Galaxies from Absorption Line Spectroscopy. III. Radial Gradients’, **841**(2), 68.

van Dokkum, P. G. and Conroy, C. (2010), ‘A substantial population of low-mass stars in luminous elliptical galaxies’, **468**(7326), 940–942.

Wang, Y., Vogelsberger, M., Xu, D., Mao, S., Springel, V., Li, H., Barnes, D., Hernquist, L., Pillepich, A., Marinacci, F., Pakmor, R., Weinberger, R. and Torrey, P. (2020), ‘Early-type galaxy density profiles from IllustrisTNG - I. Galaxy correlations and the impact of baryons’, **491**(4), 5188–5215.

Wang, Y., Vogelsberger, M., Xu, D., Shen, X., Mao, S., Barnes, D., Li, H., Marinacci, F., Torrey, P., Springel, V. and Hernquist, L. (2019), ‘Early-type galaxy density profiles from IllustrisTNG - II. Evolutionary trend of the total density profile’, **490**(4), 5722–5738.

Werner, N., McNamara, B. R., Churazov, E. and Scannapieco, E. (2019), ‘Hot Atmospheres, Cold Gas, AGN Feedback and the Evolution of Early Type Galaxies: A Topical Perspective’, **215**(1), 5.

Yoon, D., Yuan, F., Gan, Z.-M., Ostriker, J. P., Li, Y.-P. and Ciotti, L. (2018), ‘Active Galactic Nucleus Feedback in an Elliptical Galaxy with the Most Updated AGN Physics. II. High Angular Momentum Case’, **864**(1), 6.

Yoon, D., Yuan, F., Ostriker, J. P., Ciotti, L. and Zhu, B. (2019), ‘On the Role of the Hot Feedback Mode in Active Galactic Nuclei Feedback in an Elliptical Galaxy’, **885**(1), 16.

Zhao, H. (1996), ‘Analytical models for galactic nuclei’, **278**(2), 488–496.